

The Study of  $(\gamma, n)$  Reactions  
in Light Nuclei At Intermediate Photon Energy

Thesis

submitted by

Iskender AKKURT

for the degree of

Doctor of Philosophy



Department of Physics and Astronomy,

University of Glasgow,

April 1998.

©Iskender AKKURT, 1998.

ProQuest Number: 13815389

All rights reserved

INFORMATION TO ALL USERS

The quality of this reproduction is dependent upon the quality of the copy submitted.

In the unlikely event that the author did not send a complete manuscript and there are missing pages, these will be noted. Also, if material had to be removed, a note will indicate the deletion.



ProQuest 13815389

Published by ProQuest LLC (2018). Copyright of the Dissertation is held by the Author.

All rights reserved.

This work is protected against unauthorized copying under Title 17, United States Code  
Microform Edition © ProQuest LLC.

ProQuest LLC.  
789 East Eisenhower Parkway  
P.O. Box 1346  
Ann Arbor, MI 48106 – 1346

GLASGOW UNIVERSITY  
LIBRARY

11155 (copy 1)

GLASGOW  
UNIVERSITY  
LIBRARY

## Abstract

The work presented in this thesis describes an experimental study of  $(\gamma, n)$  reactions on  $^{16}\text{O}$  and  $^6\text{Li}$  nuclei using 50-70 MeV tagged photons. At this photon energy range, the so-called intermediate energy region, the photon absorption mechanism is not quantitatively established, but it is thought that pion-exchange-current effects are important. At the Max-Lab tagged photon facility in Lund(Sweden) it is possible to measure both  $(\gamma, N)$  and  $(\gamma, NN)$  reactions where N is either proton or neutron. The  $(\gamma, n)$  measurements, performed by the Glasgow-Lund collaboration, are unique to this facility. The present experiment was performed using the Glasgow-Lund time-of-flight (TOF) spectrometer where emitted neutrons were detected by two liquid scintillator arrays positioned at  $45^\circ$  and  $105^\circ$  to the photon beam. The neutron kinetic energy was determined by measuring the flight time of neutrons along a 2.5 metre path, which gave  $\sim 3$  MeV energy resolution. In order to improve energy resolution, decay  $\gamma$ -rays from excited states of  $^{15}\text{O}$ , produced after the  $^{16}\text{O}(\gamma, n)$  reaction, were measured using a large NaI(Tl) photon detector. This measurement gave  $\sim 0.3$  MeV energy resolution which was factor 10 better than the single arm  $^{16}\text{O}(\gamma, n)$  measurements, allowing states of interest in  $^{15}\text{O}$  to be separated.

The cross-sections for  $^{16}\text{O}(\gamma, n)$  reactions were obtained and compared with previous measurements performed on both  $(\gamma, n)$  and equivalent  $(\gamma, p)$  reactions. Comparisons were also made with various theoretical calculations. The  $^{16}\text{O}(\gamma, n_0)$  and  $^{16}\text{O}(\gamma, n_3)$  cross-sections were compared with HF-RPA calculations and the  $^{16}\text{O}(\gamma, n_{12})$  cross-section was compared with an MEC calculation.

For  $^6\text{Li}(\gamma, n)$  measurements the only state of  $^5\text{Li}$  to be identified unambiguously is the ground state. Cross sections were obtained for this and for the

continuum which peaks at around 25 MeV missing energy. These cross sections were compared with equivalent  ${}^6\text{Li}(\gamma, p)$  measurements. The peak continuum cross section, thought to involve interactions with the " $\alpha$ -core" of  ${}^6\text{Li}$ , was also compared with the  ${}^4\text{He}(\gamma, n)$  cross-section. Contributions of the  ${}^6\text{Li}(\gamma, pn)$  reaction to the present data were calculated using the Monte Carlo code MORGAINE and  $\alpha$ -d cluster model  ${}^6\text{Li}$  wave functions.

## **Declaration**

The data presented in this thesis were obtained by the Nuclear Structure group of the University of Glasgow in collaboration with the Nuclear Physics group of the University of Lund(Sweden) where the experiments were performed. I participated fully in the execution of the experiment. The analysis and interpretation of the experimental data is my own work. This thesis was composed by myself.

**Iskender AKKURT**

## Acknowledgements

There are so many people who supported me in many different ways during my study in Glasgow. Firstly I would like to express my special thanks to my supervisor Dr. John R.M. Annand, spokesman of the  $(\gamma, n)$  project at Max-Lab. Without his help and encouragement this work would never have been possible. My special thanks also for Dr. Cameron McGeorge who always found time to discuss any question I had. I also thank Dr. Ian Crawford, Dr. Ken Livingston and Dr. Gary Miller for being involved in this project and for all their help. The other members of the group, namely (alphabetical order) Dr. David Ireland, Dr. Douglas McGregor, Dr. Jim Kellie, Dr. Peter Harty, Dr. Sam Hall, thank you all. I would like to thank Prof. R.O.Owens, leader of the group, firstly for giving me this opportunity and funding me during my overseas visits. I would also like to thank Prof. Saxon, the head of the Physics Department at the University of Glasgow for funding my attendance of overseas conferences. My office mates Robin, Stefan, lately Ruth and Lotte, and also Stephen, Dan, Farooq, Calum, Andrew and all other students in the group, thank you all. I should not forget Dr. Ian Anthony, Andy Sibbald and also Scot Lumsden, thanks for your help with all kinds of computer problems. Outside of the department, I would like to thank friends of ours Billy McKenzie and his wife Gwenda. Thanks for all your help especially for being Scottish grandparents of my son (Hamish). Thanks also to every member of the Turkish Students' Society here in Glasgow University. It was good experience for me to be president of the society for one year.

On the Swedish side my special thanks to Dr. David Sims and Dr. Kevin Fissum. Thank you for all your help during the data analysis. I also thank other members of the collaboration namely Dr. Bent Schroder, Dr. Jan-Olof Adler, Dr. Kurt Hansen and all other Maxlab staff . I would also like to thank Dr. Jan Ryckebush from Gent University (Belgium), Dr. Peter Grabmayr from Tübingen University (Germany) and Prof. S. A. Sofianos from University of South Africa (South Africa) for providing theoretical calculations.

On the Turkish side, firstly I would like to thank my sponsor the Suleyman Demirel University for supporting me during the my study. Without this grant this work would never have been possible. My big thanks to my parents, sisters and brothers for all kinds of support and encouragement throughout my life.

Last, but certainly not least, I would like to thank my wife Suna and my lovely little son M. Fatih (10 months). Thank you both, especially you Suna, although you have had very hard time recently, you never stopped being patient and encouraging me.

To my son

# Contents

<b>1</b>	<b>Introduction</b>	<b>1</b>
1.1	General Introduction . . . . .	2
1.2	Photonuclear Physics . . . . .	3
1.3	The $(\gamma, N)$ Reaction Mechanism in the Intermediate Energy Region	5
1.4	Theoretical Models for Photoreactions . . . . .	8
1.5	The Structure of $^{16}\text{O}$ . . . . .	13
1.6	The Cluster Structure of $^6\text{Li}$ . . . . .	14
1.7	Previous Measurements on $^{16}\text{O}$ and $^6\text{Li}$ . . . . .	15
1.8	The goals of this work . . . . .	21
<b>2</b>	<b>The Experimental System</b>	<b>22</b>
2.1	Introduction . . . . .	23
2.2	The Photon Beam . . . . .	23
2.3	The Max-Lab Tagged Photon Facility . . . . .	27
2.3.1	The microtron and stretcher ring . . . . .	28
2.3.2	Tagging Spectrometer . . . . .	29
2.3.3	Tagging Efficiency . . . . .	31
2.3.4	The Photon beam monitor . . . . .	35
2.4	Time-of-Flight(TOF) Spectrometer . . . . .	36

2.4.1	Principle of Neutron Detection . . . . .	36
2.4.2	Neutron Detector Construction . . . . .	37
2.4.3	Electronics And Data Acquisition System . . . . .	39
2.4.4	Neutron Energy Determination(TOF Method) . . . . .	42
2.4.5	Particle Identification (PSD Method) . . . . .	46
2.4.6	Neutron Detection Efficiency . . . . .	49
2.5	The NaI(Tl) Detector . . . . .	52
2.5.1	Pulse-height Calibration of NaI . . . . .	54
2.5.2	NaI(Tl) Timing and n- $\gamma'$ coincidences . . . . .	55
2.6	Targets . . . . .	56
<b>3</b>	<b>Data Analysis</b>	<b>57</b>
3.1	Introduction . . . . .	58
3.2	Photon Energy . . . . .	59
3.3	PSD Analysis . . . . .	61
3.4	Neutron Time-of-Flight Calibration . . . . .	64
3.4.1	Time-Zero Calibration and Alignment . . . . .	64
3.4.2	Random Subtraction . . . . .	67
3.5	Missing Energy Spectra . . . . .	68
3.5.1	Background Subtraction . . . . .	70
3.6	Absolute Cross-sections and Experimental Uncertainties . . . . .	71
3.7	Measurement of Decay-gamma rays . . . . .	84
<b>4</b>	<b>Results and Discussion</b>	<b>87</b>
4.1	Introduction . . . . .	88
4.2	A Test Based on the $^2\text{H}(\gamma, n)$ Reaction . . . . .	88
4.3	$^{16}\text{O}(\gamma, n\gamma')$ Reaction . . . . .	90

4.3.1	Cross sections and Comparison with $(\gamma, N)$ Measurements	93
4.3.2	Comparison with Theoretical Calculations . . . . .	95
4.4	The ${}^6\text{Li}(\gamma, n)$ Reaction . . . . .	99
4.4.1	Cross sections and Comparison with $(\gamma, p)$ Measurements .	105
4.4.2	Comparison with Theoretical Calculations . . . . .	112
4.5	Summary and Outlook . . . . .	115
<b>A</b>	<b>Kinematics for the <math>A(\gamma, n)B</math> Reaction</b>	<b>118</b>
<b>B</b>	<b>Cross-section Results</b>	<b>122</b>

# List of Figures

1.1	Total photon absorption cross section per nucleon . . . . .	5
1.2	Possible reaction mechanisms at intermediate energy. . . . .	7
1.3	QFK prediction of $\frac{\sigma(\gamma, p_0)}{\sigma(\gamma, n_0)}$ for $^{16}\text{O}$ . . . . .	10
1.4	Energy level scheme and transition of $^{15}\text{O}$ . . . . .	13
1.5	The $^{16}\text{O}(\gamma, pn)$ missing energy spectrum. . . . .	16
1.6	The $^6\text{Li}(\gamma, p)$ proton energy spectrum. . . . .	18
1.7	Missing energy for $^6\text{Li}(\gamma, p)$ using tagged photons at Max-Lab. . .	19
1.8	Excitation energy of $^4\text{He}$ after $^6\text{Li}(\gamma, pn)^4\text{He}$ reaction. . . . .	20
2.1	A bremsstrahlung Spectrum obtained two different electron ener- gies. . . . .	24
2.2	The principle of photon tagging. . . . .	25
2.3	Max-Accelerator in Lund(Sweden). . . . .	28
2.4	Experimental area showing the tagger, neutron and photon detec- tors. . . . .	30
2.5	Schematic view of the collimation of the photon beam. . . . .	31
2.6	Electronic circuit for the tagging efficiency measurement. . . . .	33
2.7	ADC spectrum from the tagging efficiency photon detector. . . . .	33
2.8	Tagging efficiency measurement for each focal plane counter. . . . .	34

2.9	Calculated and measured tagging efficiencies as a function of photon energy. . . . .	35
2.10	Photon beam monitor. . . . .	36
2.11	One of the two neutron detectors arrays. . . . .	38
2.12	Electronic circuit for the measurement of $(\gamma, n)$ reaction. . . . .	40
2.13	Time-of-flight spectrum of relativistic electrons. . . . .	42
2.14	Neutron time-of-flight spectrum from the $^{16}\text{O}(\gamma, n)$ reaction. . . . .	43
2.15	Neutron resolution as a function of kinetic energy. . . . .	45
2.16	Pulse-shape signals from NE213 for neutrons and gamma-rays. . . . .	46
2.17	Neutron-gamma discrimination by the PSD method. . . . .	47
2.18	PSD setting procedure. . . . .	48
2.19	Neutron detection efficiency as a function of neutron energy. . . . .	50
2.20	Neutron detector pulse-height spectra. . . . .	52
2.21	A schematic view of the NaI(Tl) photon detector. . . . .	53
2.22	Calibration of NaI detector. . . . .	54
2.23	A: $n$ - $\gamma'$ coincidence time spectrum, B: $\gamma'$ energy spectrum. . . . .	55
3.1	Flowchart of data analysis . . . . .	58
3.2	The relationship between Photon Energy and FPD counter. . . . .	60
3.3	Numbers of coincident hits in the FPD counters in A and multiplicity distribution of FPD counters in B. . . . .	60
3.4	Raw Pulse Shape spectrum showing with pedestal. . . . .	62
3.5	Pulse Shape spectrum without pedestal. . . . .	62
3.6	A PSD scatter plot, showing the selection region of photons. . . . .	63
3.7	Ladder TDC calibration spectrum and corresponding linear fit. . . . .	65
3.8	Time Calibration of all Ladder TDC channels. . . . .	66

3.9	Time resolution corresponding to each FPD Counter. . . . .	67
3.10	TOF spectrum of neutrons and random contribution . . . . .	68
3.11	Missing energy spectrum related with Fig. 3.10 . . . . .	69
3.12	Missing energy spectrum after subtraction of random . . . . .	70
3.13	Contribution of background to the missing energy spectrum. . . .	71
3.14	A missing energy spectrum with a gaussian fit. . . . .	72
3.15	Random TOF Spectrum . . . . .	75
3.16	Duty factor of the electron beam. . . . .	76
3.17	FPD total counts for a particular run. . . . .	78
3.18	Live time efficiency of the data acquisition system . . . . .	80
3.19	Neutron Transmission efficiency for the measurement of the $^{16}\text{O}(\gamma, n_{123})$ reaction. . . . .	82
3.20	A: Missing Energy spectrum of $^{16}\text{O}(\gamma, n)^{15}\text{O}$ , B: Equivalent miss- ing energy plot, but with a TOF-NaI coincidence. . . . .	84
3.21	Decay Photon Energy ( $E_{\gamma'}$ ) spectra at $45^\circ$ neutron detection angle for two different missing energy regions in $^{15}\text{O}$ (ground state in A, unresolved 5.2-6.2 MeV states in B). . . . .	85
4.1	Missing Energy for $^2\text{H}(\gamma, n)$ reaction. . . . .	88
4.2	Cross-section for the $^2\text{H}(\gamma, n)$ reaction and comparison with pre- vious data . . . . .	89
4.3	Missing Energy Spectrum for the $^{16}\text{O}(\gamma, n)$ reaction obtained at $45^\circ$ neutron detection angle, using 50-70 MeV tagged photons. . .	91
4.4	De-excitation $\gamma$ -ray spectrum obtained in $^{16}\text{O}(\gamma, n\gamma')$ . . . . .	91
4.5	High resolution missing energy spectrum for $^{16}\text{O}(\gamma, n)$ reaction taken at Max-Lab. . . . .	92

4.6	Cross-section of $^{16}\text{O}(\gamma, n_0)$ and $^{16}\text{O}(\gamma, n_{123})$ reaction and comparison with previous measurements. . . . .	94
4.7	Cross-section of high resolution $^{16}\text{O}(\gamma, n)$ and comparison with previous $^{16}\text{O}(\gamma, N)$ data. . . . .	95
4.8	Cross-sections for $^{16}\text{O}(\gamma, n_0)$ reaction and comparison with theory.	96
4.9	Cross-sections for $^{16}\text{O}(\gamma, N)$ reactions and comparison with theory . . . . .	98
4.10	Missing energy for $E_\gamma=50.7-64.2$ MeV of $^6\text{Li}(\gamma, n)$ . . . . .	100
4.11	Missing energy for the $^6\text{Li}(\gamma, n)$ reaction at $45^\circ$ neutron detection angle. . . . .	101
4.12	Missing energy for the $^6\text{Li}(\gamma, n)$ reaction at $105^\circ$ neutron detection angle . . . . .	102
4.13	Excitation energy spectrum from the $^7\text{Li}(^3\text{He}, dt)^5\text{Li}$ reaction. . .	103
4.14	Excitation energy spectrum from the $^6\text{Li}(p, d)^5\text{Li}$ reaction at $25^\circ$ (lab) detection angle. . . . .	103
4.15	Missing energy spectra for $^6\text{Li}(\gamma, p)$ and $^6\text{Li}(\gamma, n)$ reactions. . . .	104
4.16	Missing energy spectrum for the $^6\text{Li}(e, e'p)$ reaction. . . . .	105
4.17	Angular distributions of $^6\text{Li}(\gamma, n)$ and comparison with equivalent $^6\text{Li}(\gamma, p)$ data. . . . .	106
4.18	Cross-section as a function of photon energy for the $^6\text{Li}(\gamma, N)$ reaction in the 3-9 MeV missing energy range. . . . .	107
4.19	Cross-section as a function of photon energy for the $^6\text{Li}(\gamma, N)$ reaction in the 3-15 MeV missing energy range. . . . .	107
4.20	Cross-section as a function of photon energy for the $^6\text{Li}(\gamma, N)$ reaction in the 20-30 MeV missing energy range. . . . .	108

4.21	Cross-sections for the ${}^6\text{Li}(\gamma, n)$ reaction in the 20-30 MeV missing energy range, as a function of photon energy, and comparison with ${}^4\text{He}(\gamma, n)$ measurements. . . . .	108
4.22	Angular distributions of ${}^6\text{Li}(\gamma, N)$ and ${}^4\text{He}(\gamma, N)$ reactions. . . . .	109
4.23	Cross section for the ${}^6\text{Li}(\gamma, n)$ reaction as a function of missing momentum. . . . .	110
4.24	Cross sections for the ${}^6\text{Li}(\gamma, n)$ reaction in 20-30 MeV missing energy region, as a function of missing momentum and comparison with ${}^4\text{He}(\gamma, n)$ measurement. . . . .	111
4.25	Missing energy spectra for the ${}^6\text{Li}(\gamma, n)$ reaction and comparison with theoretical calculations. . . . .	112
4.26	Angular distributions of ${}^6\text{Li}(\gamma, N)$ reactions and ${}^4\text{He}(\gamma, N)$ reactions compared with theoretical calculations for ${}^4\text{He}(\gamma, N)$ . . . . .	113
4.27	Cross section as a function of missing momentum for the ${}^6\text{Li}(\gamma, n)$ ( $E_m=20-30$ MeV) and ${}^4\text{He}(\gamma, n)$ reactions . . . . .	114
A.1	Kinematics for the $A(\gamma, n)B$ Reaction . . . . .	119

# List of Tables

1.1	Some breakup threshold energies of ${}^6\text{Li}$ . . . . .	14
2.1	Racetrack microtron parameters . . . . .	29
2.2	Pulse Stretcher mode parameters. . . . .	29
3.1	FoM for each cell . . . . .	64
3.2	Systematic uncertainties for neutron yield. . . . .	73
3.3	Stolen Coincidence parameters. . . . .	76
3.4	Target parameters . . . . .	77
3.5	Solid Angle 9 cells for A, 7 cells for B array . . . . .	79
3.6	Cross-section uncertainty parameters . . . . .	84
4.1	Energy Level scheme of ${}^{15}\text{O}$ . . . . .	93
4.2	Excited states of ${}^5\text{Li}$ . . . . .	99
B.1	The measured cross-section ( $\mu\text{b}/\text{sr}$ ) for photodisintegration of the deuteron. . . . .	122
B.2	The measured cross-sections ( $\mu\text{b}/\text{sr}$ ) for the ground state ( $n_0$ ) of ${}^{15}\text{O}$ . . . . .	123
B.3	The measured cross-sections ( $\mu\text{b}/\text{sr}$ ) for the 5.2-6.2 MeV ( $n_{123}$ ) unresolved states of ${}^{15}\text{O}$ . . . . .	123

B.4	The measured cross-sections ( $\mu\text{b}/\text{sr}$ ) for the 5.2 MeV ( $n_{12}$ ) states of $^{15}\text{O}$ . . . . .	123
B.5	The measured cross-sections ( $\mu\text{b}/\text{sr}$ ) for the 6.2 MeV ( $n_3$ ) state of $^{15}\text{O}$ . . . . .	124
B.6	The measured cross-sections ( $\mu\text{b}/\text{sr}$ ) for the $^6\text{Li}(\gamma, n)$ reaction at 3-9 MeV missing energy ( $\sigma_{3-9}^n$ ) using tagged photons of average energy 58 MeV. . . . .	124
B.7	The measured cross-sections ( $\mu\text{b}/\text{sr}$ ) for the $^6\text{Li}(\gamma, n)$ reaction at 3-15 MeV missing energy ( $\sigma_{3-15}^n$ ) using tagged photons of average energy 58 MeV. . . . .	125
B.8	The measured cross-sections ( $\mu\text{b}/\text{sr}$ ) for the $^6\text{Li}(\gamma, n)$ reaction at 20-30 MeV missing energy ( $\sigma_{20-30}^n$ ) using tagged photons of average energy 58 MeV. . . . .	125
B.9	The measured cross-sections ( $\mu\text{b}/\text{sr}$ ) for the $^6\text{Li}(\gamma, n)$ reaction at 3-9 MeV missing energy range ( $\sigma_{3-9}^n$ ) for various photon energy bins. . . . .	125
B.10	The measured cross-sections ( $\mu\text{b}/\text{sr}$ ) for the $^6\text{Li}(\gamma, n)$ reaction at 3-15 MeV missing energy ( $\sigma_{3-15}^n$ ) for various photon energy bins. . . . .	126
B.11	The measured cross-sections ( $\mu\text{b}/\text{sr}$ ) for the $^6\text{Li}(\gamma, n)$ reaction at 20-30 MeV missing energy range ( $\sigma_{20-30}^n$ ) for various photon energy bins. . . . .	126

# Chapter 1

## Introduction

## 1.1 General Introduction

Nuclear structure physics, which started with the discovery of the atomic nucleus by Rutherford, is close to one hundred years old. During this time much progress has been made, including the discovery of the neutron by Chadwick, the proposal of the mesonic theory of the nuclear force by Yukawa and the development of the shell model of nuclear structure by Mayer and Jensen. Despite all of these developments the nature of the interaction between nucleons (the N-N interaction) is not quantitatively understood at a fundamental level. Individual nucleons in the nucleus are composed of quarks and gluons whose interaction can be described by the theory of Quantum Chromodynamics (QCD). QCD can not be solved at distances of the order the nucleon radius. Thus quarks and gluons are not the most appropriate degrees of freedom for nuclei, except at very short range, and in general nucleons, mesons and isobars are more appropriate. Usually semi-empirical models, based on meson exchange, are used to describe the N-N force, but even using relatively simple forms, many-body calculations of the nuclear wavefunction for  $A > 4$  are difficult.

Nuclear structure information may be obtained by simply observing radioactive decay, e.g.  $\beta$  decays. However nuclear reactions, where an energetic probe interacts with the nucleus, generally provide more information. A nuclear reaction measurement is characterised by a beam of particles incident on a target containing the nucleus of interest, with one or more products of the reaction being emitted and detected. The incoming probe can be a strong, weak or electromagnetically interacting particle, chosen on the basis of its characteristics. The photon is a very good probe to investigate nuclear structure, because the electromagnetic interaction is very well known and relatively weak, so that the

nuclear system is only weakly perturbed. It is described by quantum electrodynamics(QED) which is one of the most accurately known theories in physics. However the relative weakness of the interaction has the disadvantage that the reaction cross-sections are small and therefore a relatively long time is needed to perform an experiment.

## 1.2 Photonuclear Physics

Photonuclear reaction studies start historically with an experiment on photo-disintegration of the deuteron by Chadwick and Goldhaber [24] using  $\gamma$ -rays emitted from a thorium source. After that many different techniques for producing a beam of photons have been tried and currently the tagged bremsstrahlung technique at high duty factor electron accelerators is in common use. Methods for producing photons will be discussed in more detail in the following chapter.

The interaction of photons with nuclei is energy dependent, because of the changing wavelength of the photons, and the photon energy range below 1 GeV may be conveniently divided into three regions, on the basis of the physical process believed to dominate in a region. Fig. 1.1 shows the total photoabsorption cross-section per nucleon for various nuclei, which shows prominent features discussed in the following.

### The Giant Resonance Region

In the energy region between 10-40 MeV, the total photon absorption cross-section exhibits a broad peak (Fig.1.1). Here the photon's wavelength is similar to the dimensions of the nucleus. Therefore the photon interacts with the nucleus as a whole rather than with individual nucleons. Photonucleon emission is well

described by a collective excitation of the nucleus to 1-particle, 1-hole states and subsequent nucleon emission by an evaporation process. Since the momentum transfer from the photon to the target nucleus is relatively small in this photon energy range, the photoexcitation is predominantly of an electric dipole (E1) character.

### The Quasi-deuteron Region

The region from 40-140 MeV is also called the intermediate energy region and the work of this thesis is concentrated here. Since the photon energy is higher, the photon wave-length is smaller than in the giant resonance region. In this region a large part of the total absorption cross-section is due to the  $(\gamma, pn)$  reaction through the absorption of the photon by a correlated neutron-proton pair. For this reason this region is sometimes called *quasi-deuteron*. The photon may interact with a single nucleon or with a virtual meson exchanged between nucleons (correlated pair) and the relative importance of these two mechanisms is still not well understood. Single nucleon processes could give some information on high-momentum components of the nucleon in the nucleus and the absorption on pairs may give information on meson exchange currents. The reaction mechanisms in the intermediate energy region will be discussed more deeply in section 1.3.

### The Nucleon Resonance Region

In the photon energy range above the pion ( $\pi$ ) production threshold at 140 MeV, excitation of nucleon resonances becomes important. The most prominent of these is the  $\Delta(1232)$  resonance which peaks at  $\sim 330$  MeV and can be thought of as the first excited state of the nucleon, where one of the constituent quarks has undergone a spin-isospin flip transition.

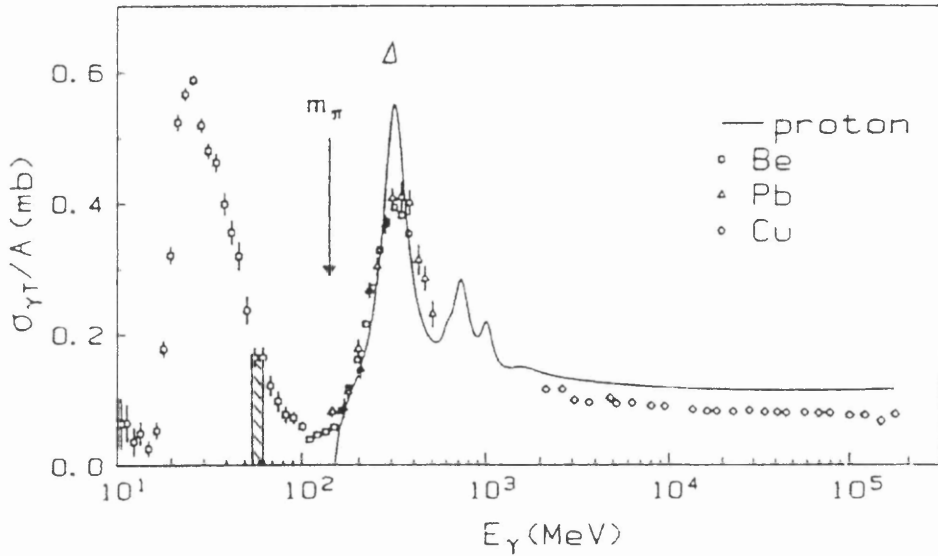


Figure 1.1: Total photon absorption cross section per nucleon [2] (hatched area shows the photon energy range of the present measurement).

Above the  $\Delta(1232)$  resonance several higher resonances are observed for the proton although for nuclei these are smeared out.

### 1.3 The $(\gamma, N)$ Reaction Mechanism in the Intermediate Energy Region

At intermediate energies, the reaction mechanism has been under debate in recent years. In the study of single-arm,  $(\gamma, N)$  reactions ( $N=p,n$ ), it is expected that the photon will interact, in a simplified picture, either with a single nucleon current in a quasi-free knockout process(QFK) or with meson-exchange currents (MEC) between correlated nucleons. The QFK process, leaves the residual nucleus in a one-hole (1h) state relative to the target nucleus (Fig.1.2A). A high

momentum mismatch between incoming photon and outgoing nucleon, typically  $\sim 300 \text{ MeV}/c$  for  $E_\gamma \sim 60 \text{ MeV}$  which must be made up by the nucleon's internal kinetic energy, should suppress the QFK process in  $(\gamma, N)$  reactions. If  $(\gamma, N)$  proceeds by QFK, then it should probe the high-momentum tail of the single-particle wave function. Since the photon can only couple weakly to the magnetic moment of the uncharged neutron, QFK predicts that cross-sections of  $(\gamma, n_0)$  are much smaller than corresponding  $(\gamma, p_0)$  cross-sections. The zero subscript denotes that the residual,  $A-1$  system is left in the ground state. However early bremsstrahlung measurements have shown, surprisingly, that cross-sections for the  $(\gamma, n_0)$ [40] and  $(\gamma, p_0)$ [36] reactions are similar in magnitude and this has been confirmed by recent tagged photon measurement[6, 9, 67]. This similarity has been explained in a phenomenological way by Schoch[77] in terms of the modified quasi-deuteron mechanism (MQD), in which the photon is absorbed on a pn pair and one of them is reabsorbed into the residual nucleus (see sec 1.4). The more microscopic Hartree-Fock-Random-Phase-Approximation (HF-RPA) approach of the Gent group[75], which considers photon absorption on MEC and multi-step processes (MSP), thus including the effects of long and medium range N-N correlations, also predicts the approximate equality of the cross-sections.

Absorption of photons by correlated nucleon pairs (mainly p-n) leaving the residual nucleus in a two-hole (2h) state(Fig.1.2D) is thought to be the dominant mechanism at intermediate energy. For  $(\gamma, N)$  one of nucleons is reabsorbed into the initial or to another orbital leaving the residual nucleus in a 1h or two-hole, one-particle (2h-1p) state (Fig.1.2CB respectively). For all these processes the knocked-out nucleons interact strongly with the residual system. Final state interactions (FSI) sometimes referred to as rescattering, may have a large effect on the cross-section.

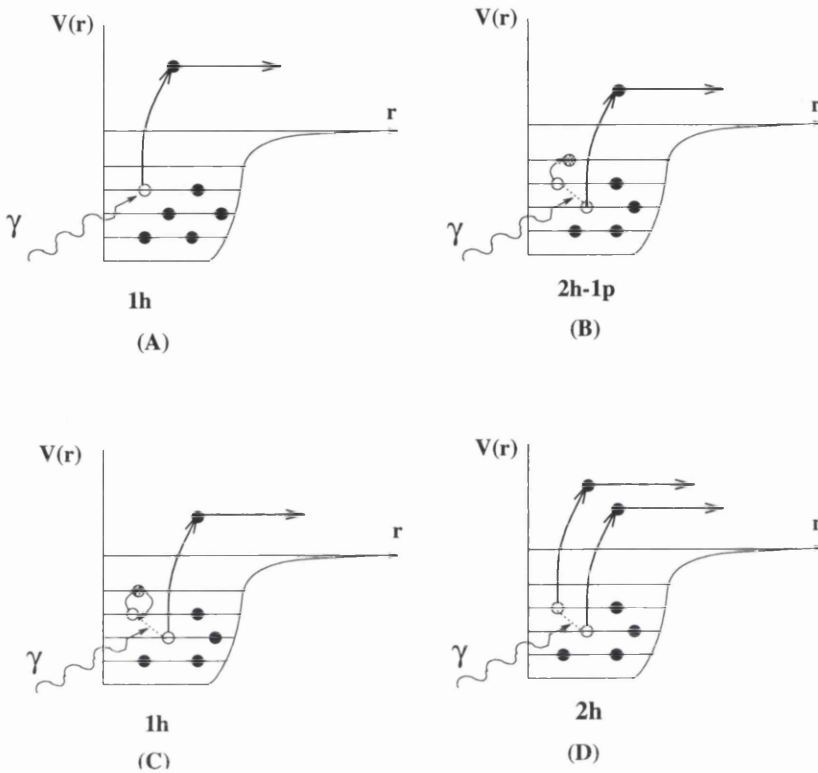


Figure 1.2: Possible reaction mechanisms at intermediate energy.

In order to clarify the reaction mechanism in this energy range a broad body of  $(\gamma, N)$  data should be studied :

1. Both  $(\gamma, n)$  and  $(\gamma, p)$  need to be measured, because QFK of a single proton should be much stronger than single uncharged neutron knockout. On the other hand,  $\gamma$  absorption on a pn pair should lead to comparable  $(\gamma, n)$  and  $(\gamma, p)$  cross-sections.
2. Measure over a broad range of photon energy and missing momentum as the different reaction mechanisms have different photon energy and momentum dependence.
3. Make measurements in which discrete states are identical in the mass  $A-1$  nucleus, because different reaction mechanisms can populate excited states

of different structure.

4. Measure over a range of A because FSI effects can change with A.

In recent years the development of tagged photon facilities, following on from high-duty-factor electron accelerators, has resulted in a number of  $(\gamma, N)$  experiments [6, 9, 67, 45, 82, 86] with good enough energy resolution to be able to resolve different individual residual states in light nuclei ( $A=4-40$ ). These results suggest that absorption of photons by MEC, and FSI are very important in the intermediate energy region. As the detection of a charged particle (proton) is much easier than a neutral particle, most of the measurements have focused on the  $(\gamma, p)$  reaction [26, 45, 46, 55, 67, 68, 86].

## 1.4 Theoretical Models for Photoreactions

Assuming QFK the differential cross-section for a  $(\gamma, N)$  reaction in the Plane Wave Impulse Approximation (PWIA), where it is assumed that outgoing nucleon can be represented by a plane wave, can be written as [58]

$$\frac{d\sigma}{d\Omega} = C(P_\gamma, \theta_N, A) \cdot |\Phi(P)|^2 \quad (1.1)$$

where C is a kinematical factor,  $\theta_N$  is the emission angle of the emitted nucleon, A is the target nucleus mass number and  $|\Phi(P)|^2$  is the momentum distribution of the bound nucleon inside the nucleus. The missing momentum  $P_m$  in a QFK process,

$$\mathbf{P}_m = \mathbf{P}_\gamma - \mathbf{P}_N \quad (1.2)$$

where  $P_N$  and  $P_\gamma$  are the momentum of the emitted nucleon and the incoming photon.

As FSI is not included in the PWIA, this effect must be further considered. As the detected particle travels out of the nuclear potential well its momentum decreases and it is more realistic to use the Distorted Wave Impulse Approximation (DWIA), where the wave function of the detected (outgoing) particle is distorted by a suitable optical potential. Findlay and Owens[36] used a DWIA analysis to extract nucleon momentum densities from  $(\gamma, p)$  and  $(e, e'p)$  measurements.

Although the  $(\gamma, p_0)$  cross-section has been reasonably well described by DWIA [16] at intermediate energy it has failed in the case of  $(\gamma, n_0)$  cross-sections and it is of course not equipped to explain  $(\gamma, pn)$ . Fig.1.3 shows a QFK prediction for the ratio of cross-sections  $\left(\frac{\sigma(\gamma, p_0)}{\sigma(\gamma, n_0)}\right)$  which is compared with experimental results on  $^{16}\text{O}$ . The similarity of cross-sections for  $(\gamma, n_0)$  and  $(\gamma, p_0)$  reactions was explained by Schoch[77] by introducing the modified-quasi-deuteron (MQD) model.

The MQD model is based on Levinger's quasi-deuteron (QD) model[57] where the photon is absorbed on a p-n pair, instead of a single nucleon, resulting in pn emission. According to Levinger the photon absorption cross-section  $\sigma$  for a complex nucleus at intermediate energy is proportional to the free deuteron photodisintegration cross-section  $\sigma_d$  at the same photon energy.

$$\sigma = L \times \frac{NZ}{A} \times \sigma_d \quad (1.3)$$

where  $\frac{NZ}{A}$  represents the possible number of p-n pairs per unit volume. The value of  $L$  is related to the relative probability that a neutron and proton are closely correlated in the nucleus compared to the deuteron. Levinger estimated the value of  $L$  to be 6.4. If photon absorption is on a quasi-deuteron both nucleons share the momentum and energy of the photon and so the problem of momentum mismatch is avoided. Recently McGeorge et al. [66] reported that a

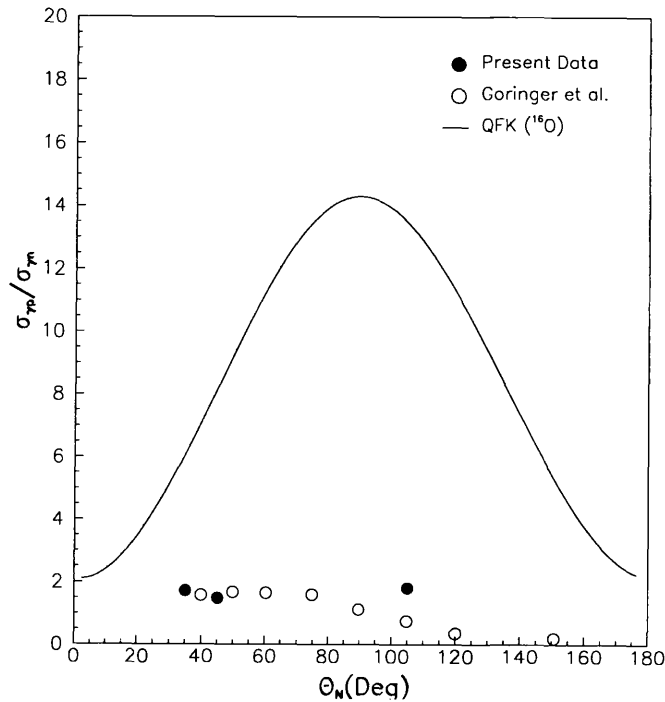


Figure 1.3: QFK prediction of  $\frac{\sigma(\gamma,p_0)}{\sigma(\gamma,n_0)}$  for  $^{16}\text{O}$  (solid curve) and comparison with data (filled circles: neutron data from present measurement and ref.[6], proton data from ref. [67]. open circles: neutron data from ref. [40] and proton data from ref.[36]).

good description of  $(\gamma,2N)$  on  $^{12}\text{C}$  was obtained using the QD model.

Although the QD model has been popular in phenomenological analyses of the data the physical significance of  $L$  was questioned by Eden et al. [33] who pointed out that not all pairs in a complex nucleus will couple in an antisymmetric wavefunction to the same orbital angular momentum, spin and isospin as a deuteron.

In the modified version (MQD) one of the knocked-out nucleons is reabsorbed by the nucleus and the photon energy is transferred to a single nucleon whereas the momentum is shared by the pair. If the nucleon returns to the same orbit

then  $(\gamma, N)$  populates 1h states in the residual nucleus. If it returns to a different orbit then the residual state is 2h-1p in character (see Fig.1.2). The cross-section for the  $(\gamma, N)$  reaction can be written as,

$$\frac{d\sigma(E_\gamma, \Theta_N)}{d\Omega} = \frac{L}{A} \cdot \left[ \frac{d\sigma(E_\gamma, \Theta_N)}{d\Omega_{cm}} \right]_d \cdot J \cdot P_s \cdot A(E_\gamma, \Theta_N) \quad (1.4)$$

where J is the Jacobian for the various coordinate transformations necessary in the calculation,  $P_s$  is a phase space factor,  $A(E_\gamma, \Theta_N)$  is the ability of the nucleus to absorb the transferred momentum and  $\left[ \frac{d\sigma(E_\gamma, \Theta_N)}{d\Omega_{cm}} \right]_d$  is the deuteron disintegration cross-section. Sene' et al. [80] described the  ${}^7\text{Li}(\gamma, p_0)$  and the  ${}^7\text{Li}(\gamma, n_0 + n_2)$  cross-sections at several angles, for photon energies between 60 MeV and 120 MeV using the MQD model. The  $n_2$  means that the residual system is in the second excited state. Although the MQD model describes  $(\gamma, N)$  reactions reasonably well a major drawback of this model is the use of plane waves for the outgoing nucleon.

The QD model is a phenomenological model since the details of the dynamics of the quasideuteron photodisintegration are contained within the empirical real deuteron cross-section. Therefore more microscopic models are needed for a fundamental understanding of the photon absorption mechanism and include the model of Gari and Hebach [39], the HF-RPA models of Cavinato et al.[20, 21, 22], Rykebusch et al. [75] and the MEC model developed by Benenti et al.[14].

Gari and Hebach [39] used shell-model wavefunctions in photonuclear reactions for the first time in the 1980's. Their calculations were carried out for photon energies 40-140 MeV and for the reactions  $(\gamma, N)$  and  $(\gamma, NN)$ . They calculated cross sections assuming the nuclear current  $\mathbf{J}(\mathbf{r}, \mathbf{t})$  has components arising from:

- one-body nucleon currents only, calculated from shell-model wave func-

tions(SM)

- including MEC effects (SM+MEC)
- including correlation effects (SM+CORR)
- including both MEC and correlation effects (SM+MEC+CORR)

The nuclear current can now be written

$$\mathbf{J} = \mathbf{J}_N + \mathbf{J}_{MEC} + \mathbf{J}_{CORR} \quad (1.5)$$

They found that the contributions of these components to  $(\gamma, N)$  reactions are different. For the  $(\gamma, p)$  reaction individual contributions of CORR and SM are very small, and SM+MEC is almost fully responsible for the measured cross-section. In the case of  $(\gamma, n)$  CORR effects are more important. The SM contribution is very small when it is compared with  $(\gamma, p)$  and the SM+MEC contribution is somewhat smaller. The recent  $^{16}\text{O}(\gamma, p_0)$  cross-section measurement by Miller et al. [67] is explained well by this model. Cavinato et al. [20, 21, 22] have produced a model that provides a unified description of photoabsorption by closed-shell nuclei ( $^{12}\text{C}$ ,  $^{16}\text{O}$ ,  $^{40}\text{Ca}$ ) at energies from the GDR region to pion threshold. The calculation which is similar in spirit to that of Gari and Hebach, has been performed using the formalism of the RPA, which describes long-range-correlations (residual collective effects) and final-state rescattering. The similar HF-RPA model developed in Gent[75], which will be discussed in section 4.2.2, predicts that MEC effects and final-state scattering are important in  $(\gamma, N)$  reactions. The effects of MEC were investigated by Benenti et al. [14] using a two-body current operator in an extension of the Pavia DWIA model. This calculation will also be discussed in section 4.2.2.

The models described above can be applied to complex nuclei such as  $^{12}\text{C}$ ,  $^{16}\text{O}$  or  $^{40}\text{Ca}$  where the mean-field assumption of the shell model can be justified. Lighter nuclei deviate from this picture and  $^6\text{Li}$  for example has a cluster structure consisting of an  $\alpha$ -particle core orbited by a p-n pair.

## 1.5 The Structure of $^{16}\text{O}$

$^{16}\text{O}$  with 8 protons and 8 neutrons, has closed proton and neutron shells and is well suited to a shell-model description. It is also light enough that final state interactions should not obscure the effects of the primary interaction.

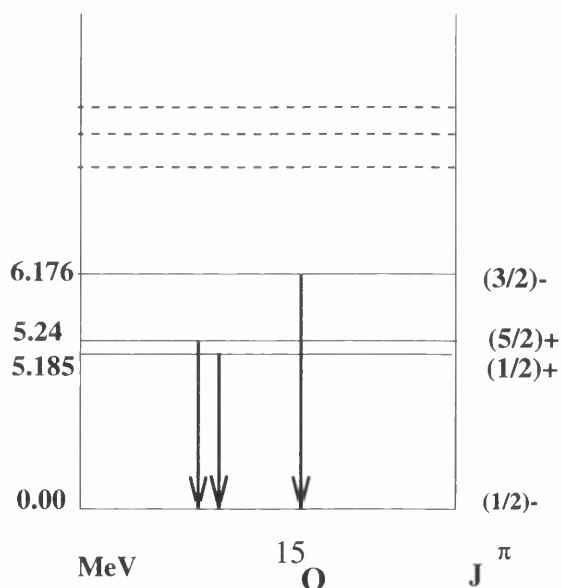


Figure 1.4: *Energy level scheme and transition of  $^{15}\text{O}$ .*

The  $(\gamma, n)$  reaction which has a threshold of 15.7 MeV, may leave the residual  $^{15}\text{O}$  nucleus in the ground or some excited state. The configuration of these states are:  $(1p_{1/2})^{-1}$  for the  $\frac{1}{2}^-$  (ground state),  $(1p_{3/2})^{-1}$  for the  $\frac{3}{2}^-$  (6.2 MeV) state, which both are 1h in character and  $(1p_{1/2})^{-2} (2s_{1/2})$  for the  $\frac{1}{2}^+$  (5.18 MeV)

state and  $(1p_{1/2})^{-2} (1d_{5/2})$  for the  $\frac{5}{2}^+$  (5.24 MeV) state which both are 2h-1p in character. A level diagram is given in Fig.1.4 where the ground and first three excited states are shown. The decay- $\gamma$  ray branching ratio from the excited states of 5.2-6.2 MeV to the ground state is 100 %, which means there are no cascades through these states.

## 1.6 The Cluster Structure of ${}^6\text{Li}$

${}^6\text{Li}$ , with 3 neutrons and 3 protons has interesting structure which has been investigated both experimentally and theoretically. The configuration for both protons and neutrons is  $(1s_{1/2})^2(1p_{3/2})^1$  which suggests a picture of a  $\alpha$ -core and two valence nucleons.

Reaction	Threshold(MeV)
${}^6\text{Li} \longrightarrow n + {}^5\text{Li}$	5.7
${}^6\text{Li} \longrightarrow p + {}^5\text{He}$	4.59
${}^6\text{Li} \longrightarrow d + {}^4\text{He}$	1.475
${}^6\text{Li} \longrightarrow t + {}^3\text{He}$	15.796
${}^6\text{Li} \longrightarrow p + d + t$	21.287
${}^6\text{Li} \longrightarrow d + d + d$	25.322
${}^6\text{Li} \longrightarrow p + n + {}^4\text{He}$	3.7
${}^6\text{Li} \longrightarrow n + d + {}^3\text{He}$	22.053
${}^6\text{Li} \longrightarrow p + p + n + t$	23.512
${}^6\text{Li} \longrightarrow p + n + d + d$	27.546
${}^6\text{Li} \longrightarrow p + p + n + n + d$	29.7706

Table 1.1: *Some breakup threshold energies of  ${}^6\text{Li}$*

In table 1.1 some threshold energies for  ${}^6\text{Li}$  photodisintegration are listed. It can be seen that the smallest threshold energy is for deuteron and p-n pair emission, which was explained by Schmid[79] by assuming that the photon interacts with the two valence nucleons and the  ${}^4\text{He}$  ( $\alpha$ -core) stays intact. Thus a shell-model description of  ${}^6\text{Li}$ , where the nucleons are assumed to move independently within a mean field, is not valid and several cluster models have been proposed. Some models treat  ${}^6\text{Li}$  as an  $\alpha$ -d cluster [59], some as  $\alpha$ -pn[54, 71, 89] and some as t-h or t-d-p [60]. Kukulín et al.[53] calculated the weight of the cluster configuration  $\alpha$ -d in the total wave-function of  ${}^6\text{Li}$  in a three-particle model ( $\alpha$ -NN). It was found that  $\alpha$ -d clusters are responsible for 65% of the total wave-function. Ferroni et al. [35] made a calculation of photoneutron cross-sections where they described  ${}^6\text{Li}$  as an  $\alpha$ -d cluster. This prediction was in good agreement with the experimental work done by Costa et al.[25]. The possibility of h-t cluster and  $\alpha$ -d cluster configurations in  ${}^6\text{Li}$  were investigated by Burkova et al [18] who also included MEC and FSI effects in the calculation. In a comparison with experimental data which was taken by herself, the  $\alpha$ -d model gave a better description of  ${}^6\text{Li}$  than the h-t model.

## 1.7 Previous Measurements on ${}^{16}\text{O}$ and ${}^6\text{Li}$

Although most previous photonuclear measurements have focused on  $(\gamma, p)$  reactions there have been some interesting studies performed on  $(\gamma, n)$  reactions.

### Measurements on ${}^{16}\text{O}$

${}^{16}\text{O}$  has been a popular target to measure both  $(\gamma, N)$  and  $(\gamma, NN)$  reactions as good shell-model calculations of its wavefunction are available.

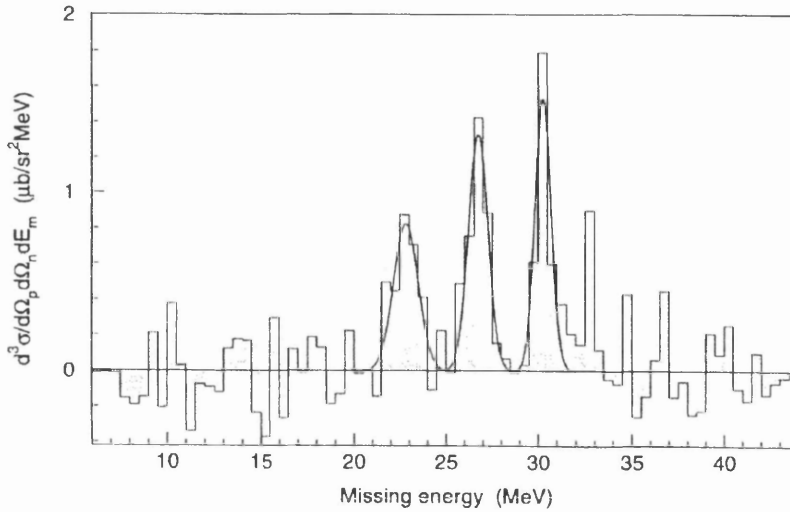


Figure 1.5: The  $^{16}\text{O}(\gamma, pn)$  missing energy spectrum obtained at Max-Lab [47].

An early  $(\gamma, n)$  measurement was performed by Goring et al.[40] using the end-point kinematics method (see section 2.2). In this measurement, for the first time, a photon energy above giant resonance and an energy resolution comparable to that of  $(\gamma, p)$  [36, 64] was obtained. At 60 MeV photon energy, neutrons were detected over the angular range  $40\text{-}149^\circ$  and the  $90^\circ$  cross-section was measured over the energy range 60-160 MeV. Energy resolution was not good enough to resolve excited states in  $^{15}\text{O}$  and therefore  $(\gamma, n_0)$  cross-sections only were measured. More recently, data were taken at Sendai[69] using tagged photons (section 2.2). These measurements were made at  $45, 60$  and  $90^\circ$  neutron detection angle in the energy range 25-100 MeV. The latest measurements [6] were performed at Max-Lab with 60 MeV tagged photons, using the same neutron detector as the present measurement. These measurements were performed at  $35, 50, 70, 90$  and  $110^\circ$  neutron detection angle with low energy resolution (FWHM  $\sim 3$  MeV), at  $30, 40$  and  $80^\circ$  with medium energy resolution (FWHM  $\sim 2$  MeV)

and at  $60^\circ$  with high energy resolution (FWHM  $\sim 1$  MeV). This last measurement has given the only available data where it was possible to resolve the 5.2 MeV doublet and 6.2 MeV states, as will be shown in Fig.4.5. An equivalent high resolution measurement[67] of  $^{16}\text{O}(\gamma, p)$  was performed at Max-Lab using 60 and 75 MeV tagged photons and  $35\text{-}125^\circ$  proton detection angles. Good energy resolution ( $\sim 800$  keV) was obtained and the 5.3 and 6.3 MeV states were resolved at all angles. Recently a high resolution  $^{16}\text{O}(\gamma, pn)$  measurement[47] has been performed at Max-Lab using tagged photons of average energy 72 MeV. Here, with  $\sim 2$  MeV missing energy resolution, the states of the residual  $^{14}\text{N}$  nucleus were resolved for the first time. A missing energy spectrum of this measurement is shown in Fig.1.5 where the ground, 3.95 MeV and 7.03 MeV states of the residual  $^{14}\text{N}$  nucleus were resolved. The threshold for the reaction is 23 MeV and no population of the first excited state at 2.31 MeV is observed.

### Measurements on $^6\text{Li}$

Although there has not been any previous tagged photon  $^6\text{Li}(\gamma, n)$  measurement, a very early measurement was done in the GDR region by Costa et al [25], using bremsstrahlung produced by a 100 MeV electron beam, and this data were evaluated by Ferroni et al [35] later. These data show two maxima in the total photoneutron cross-section, one around a photon energy of 11 MeV which is the result of photoemission of a valence neutron and another around a photon energy of 26 MeV which corresponds to the photoexcitation of the  $\alpha$  core within the  $^6\text{Li}$  nucleus. Photoneutron cross-sections were also measured by Berman et al.[15] as a function of photon energy (5.7-32 MeV), using photons from the annihilation in flight of fast positrons (see section 2.2). It was reported that there may be present in the ground state of  $^6\text{Li}$  an appreciable, bound h-t configuration, in

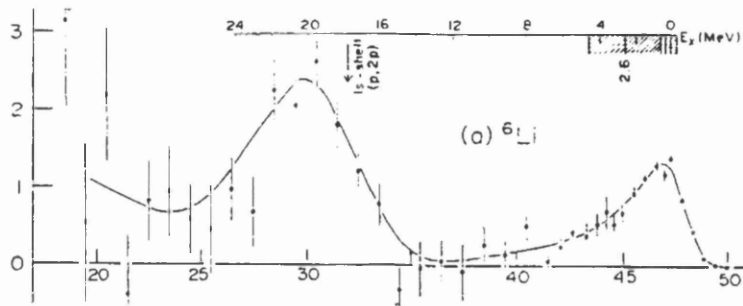


Figure 1.6: The  ${}^6\text{Li}(\gamma,p)$  proton energy spectrum obtained using the bremsstrahlung difference technique [64].

contrast to the finding of Costa et al. [25].

The  ${}^6\text{Li}(\gamma,p)$  reaction has been studied using bremsstrahlung and tagged photons. For example an early  ${}^6\text{Li}(\gamma,p)$  measurement by Matthews et al.[64], using the bremsstrahlung difference technique (see section 2.2), showed clear population of the ground state of  ${}^5\text{He}$  (around 45-50 MeV proton energy in Fig.1.6) and also a broad structure in the 14-23 MeV excitation energy range (around 30 MeV proton energy in Fig.1.6). Carlos et al[19] measured the  ${}^6\text{Li}(\gamma,p)$  cross-section at  $90^\circ$  proton detection angle with 30-100 MeV tagged photons. In the detected proton energy spectrum a clear peak corresponding to the  ${}^5\text{He}$  ground state and a large bump around 20-30 MeV missing energy range were observed. This measurement was in good agreement with a QD model calculation at photon energies higher than 80 MeV. Wade et al[87] measured the  ${}^6\text{Li}(\gamma,pn)$  reaction using 67 MeV end point bremsstrahlung. It was concluded that a substantial contribution to the  ${}^6\text{Li}(\gamma,p)$  reaction at  $\sim 30$  MeV missing energy is from the  $(\gamma,pn)$  channel. More recently a number of tagged photon measurements on  ${}^6\text{Li}$  have been performed at Max-Lab[26, 27, 46, 68, 74]

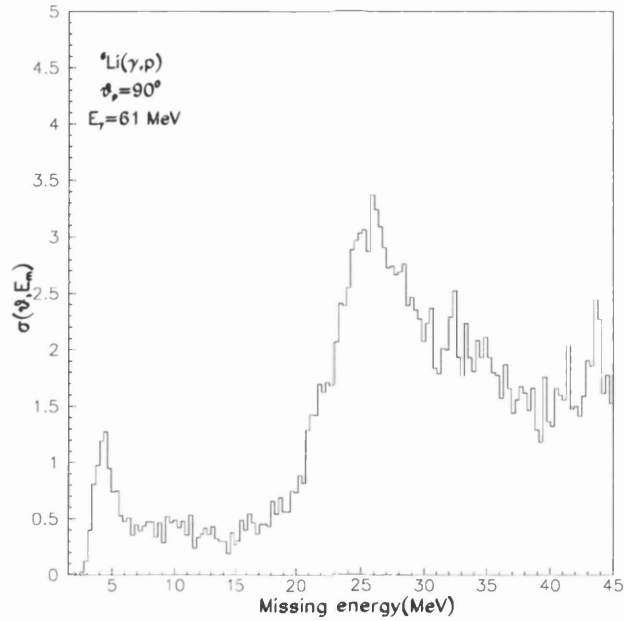


Figure 1.7: Missing energy for  ${}^6\text{Li}(\gamma, p)$  using tagged photons at Max-Lab[68].

$$\begin{aligned}
 {}^6\text{Li}(\gamma, c) & \quad c=p, d, t, h \\
 {}^6\text{Li}(\gamma, cc') & \quad c = p \quad c' = n, d, t \\
 & \quad c = d \quad c' = t, h \\
 & \quad c = t \quad c' = d, h
 \end{aligned}$$

The  $(\gamma, p)$  measurement was performed at Max-Lab[46, 68] at  $90^\circ$  proton detection angle, using 61 MeV photons. Fig.1.7 shows the missing energy spectrum obtained [68] in the  ${}^6\text{Li}(\gamma, p)$  reaction. The peak at  $\sim 4.6$  MeV is from 1p shell knockout leaving  ${}^5\text{He}$  in the unbound ground state. The weak "shoulder" at  $\sim 21.3$  MeV results from 1s knockout. Continuum structure resulting from the breakup of  ${}^6\text{Li}$  into more than two particles is also visible. A broad bump observed around 20-30 MeV is due to the three-particle breakup of  ${}^6\text{Li}$ .

The measurements of  ${}^6\text{Li}(\gamma, c)$  reactions performed by Dias et al. [26, 27] used tagged photons of average energies  $\sim 59$  and  $\sim 75$  MeV, and five different

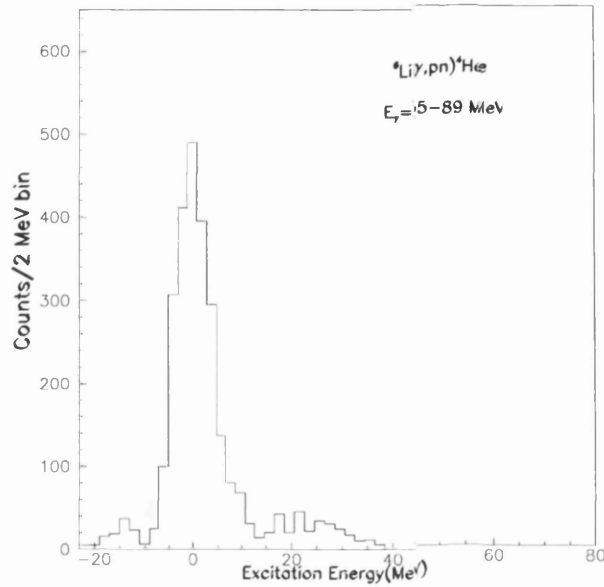


Figure 1.8: *Excitation energy of  ${}^4\text{He}$  after  ${}^6\text{Li}(\gamma, pn){}^4\text{He}$  reaction [51].*

detection angles ( $30\text{-}150^\circ$ ). The  ${}^6\text{Li}(\gamma, p)$  measurement confirmed the previous measurement [68] performed at Max-Lab.

${}^6\text{Li}(\gamma, pn)$  measurements have been performed at Max-Lab [51] and Mainz[65] using tagged photons. Fig.1.8 is the missing energy spectrum of the  ${}^6\text{Li}(\gamma, pn)$  reaction[51] obtained using 55-89 MeV tagged photons at Max-Lab. The main contribution comes from  $1p1p$  p-n emission ( prominent peak in Fig.1.8), ie emission of the valence p-n pair. Much weaker  $1p1s$  and  $1s1s$  excitations (at higher excitation energy), which involve disintegration of the tightly bound  $\alpha$ -core, become more prominent at higher photon energies. The total cross-section for the  $(\gamma, pt)d$  reaction[74], where photons interact with the  $\alpha$ -core, was found to be larger than the  $(\gamma, pn)$ [51] reaction cross section up to 75 MeV photon energy.

## 1.8 The goals of this work

The  $(\gamma, N)$  project at Max-Lab is being carried out on light to medium mass ( $A=4,6,12, 16,40$ ) nuclei to provide structure information (mainly  $A=4,6$ ) and to gain information on the photon absorption mechanism (mainly  $A=12,16,40$ ) at 50-70 MeV photon energy. Results from this project have been published for  $^{12}\text{C}(\gamma, n)$ [9],  $^{16}\text{O}(\gamma, n)$  [6],  $^4\text{He}(\gamma, n)$ [81],  $^{40}\text{Ca}(\gamma, n)$  [82],  $^{16}\text{O}(\gamma, p)$  [67] and  $^{12}\text{C}(\gamma, p\gamma')$  [55] measurements. The measurements presented in this thesis represent a step of this project in which  $A=6,16$  nuclei have been used as the target.  $^{16}\text{O}(\gamma, n)$  has been previously measured, but mainly with poor resolution, and the aim has been to identify excited states of the  $^{15}\text{O}$  residual nucleus through their decay gamma rays. The main interest is in the mainly 2h1p doublet of states at 5.2 MeV, where the strength of excitation may be sensitive to MEC effects. In the case of the  $^6\text{Li}$  target, its cluster structure makes it an interesting choice for study. This has been studied in several photo-reactions at intermediate energy, but never through  $(\gamma, n)$  which is complementary to other reactions. Comparison of the  $(\gamma, n)$  measurement with other reactions such as  $(\gamma, p)$  will help the understanding of the cluster structure of  $^6\text{Li}$  and constrain microscopic many-body models of nuclear structure which are starting to produce quantitative predictions for  $A>4$ .

## **Chapter 2**

# **The Experimental System**

## 2.1 Introduction

The experiment was performed at Max-Lab (Lund-Sweden) using bremsstrahlung photons tagged at energies between 50 and 70 MeV, the Glasgow-Lund neutron time-of-flight spectrometer and for  $(\gamma, n\gamma')$  measurements a single large NaI(Tl) gamma-ray detector. In the following section more details about the apparatus which was used to perform the present measurement is given.

## 2.2 The Photon Beam

For photonuclear reaction studies one of the biggest problems is the difficulty of producing a monochromatic photon beam at a desired energy. Although there are several different methods to produce monochromatic photons the most common technique uses Bremsstrahlung emission. An electron may radiate a photon, of energy up to the incident electron energy, in the electric field of an atomic nucleus, so that if a beam of mono-energetic electrons impinges on a thin foil (radiator) a continuous energy distribution of bremsstrahlung photons is produced. In Fig.2.1A a typical bremsstrahlung spectrum [62] produced by electrons of energies 50 MeV (dashed curve) and 51 MeV (solid curve) is given. In Fig.2.1B these spectra were subtracted from each other resulting in a bremsstrahlung difference photon spectrum. In a photonuclear experiment the continuous energy spectrum of the bremsstrahlung beam implies that the energy of an individual photon absorbed by the target is unknown. For certain reactions on simple nuclei, such as  $d(\gamma, p)n$ , the reaction kinematics are completely determined by the energy and angle of the detected particle. If a reaction on a complex nucleus produces a residual (undetected) nucleus with well-spaced energy levels,

e.g.  $^{16}\text{O}(\gamma, n)^{15}\text{O}_{\text{ground}}$  where the ground state is separated from the first excited state by 5 MeV, photons close to the bremsstrahlung end-point may be selected by selecting only the highest energy neutrons[40]. Thus in certain experiments it is not necessary to measure the photon energy directly, but for most exclusive reaction measurements on complex nuclei it must be known.

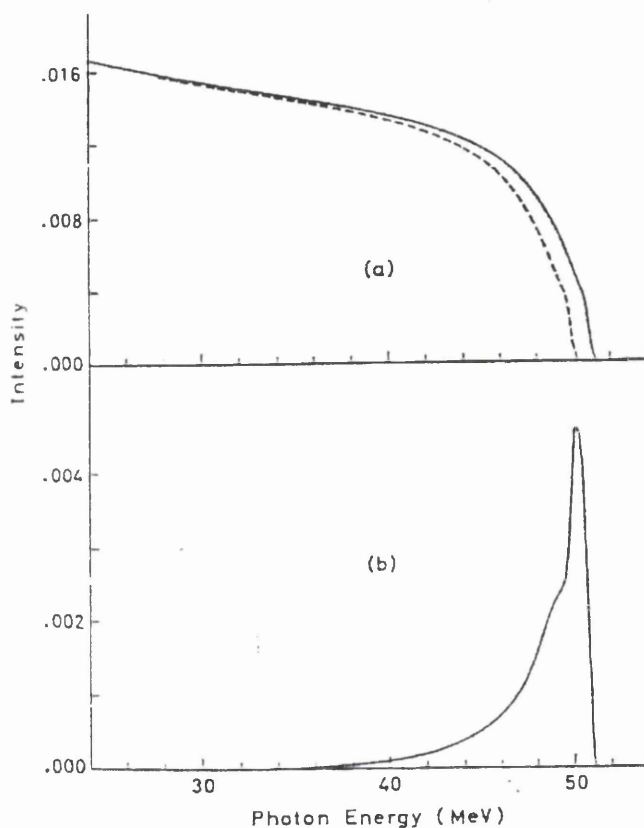


Figure 2.1: *a: Bremsstrahlung Spectrum obtained for electron energies 50 and 51 MeV [62]; b: the result when the distribution are subtracted.*

The bremsstrahlung difference technique is a possible solution. In Glasgow [62, 63] this technique was used to achieve a photon "energy resolution" of about 2 MeV. Two bremsstrahlung radiators of different  $Z$  (Be and Al), may be used to try to minimize for the tail in the difference spectrum (Fig.2.1B). However as the

shape of the bremsstrahlung spectrum is least well known around the end-point the bremsstrahlung difference method may give large systematic uncertainties. Statistical uncertainties may also be large as the bremsstrahlung intensity around the end point is relatively low, possibly limited by counting rates induced by the much higher intensities at lower photon energies.

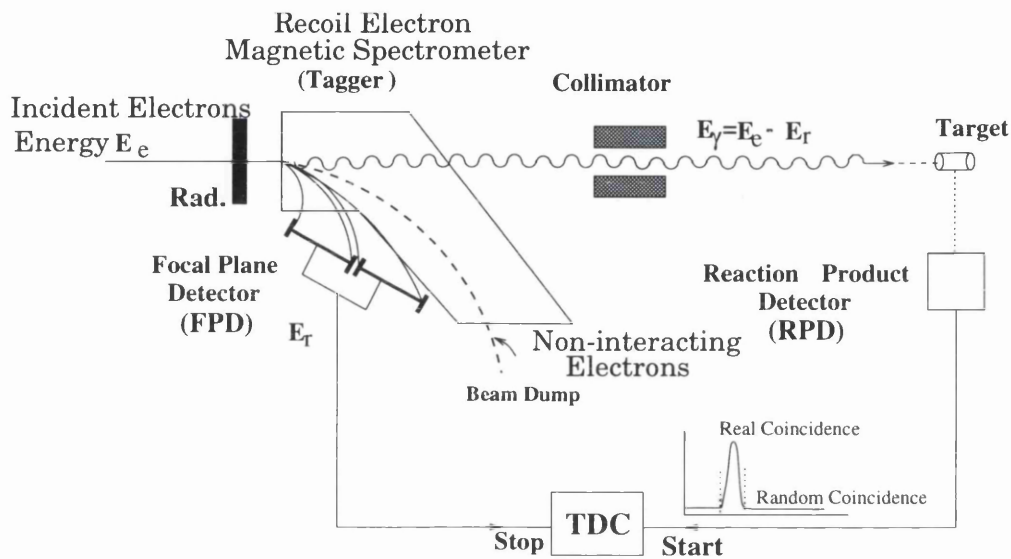


Figure 2.2: The principle of photon tagging. The time-to-digital converter(TDC) measures the time difference between the start and stop signals.

Many of the problems associated with bremsstrahlung experiments can be solved if the energy of the electron, after production of a bremsstrahlung photon, is measured. This method is called the photon tagging technique[88]. It can in principle yield a useful beam flux and give a good measure of beam energy and intensity. The principle of photon tagging is shown in Fig.(2.2). An incident monoenergetic electron with energy  $E_e$  impinges on a thin radiator and produces bremsstrahlung which passes through a collimator and interacts in the target. The beam is collimated in order to get a well-defined photon beam on the target. The magnetic spectrometer serves to momentum analyse the inelastic electrons

produced after the bremsstrahlung process and separate the non-interacting electron beam from the photon beam. The magnetic field of the spectrometer is measured by using a Nuclear Magnetic Resonance (NMR) probe. Knowing the field and the hit position of the electron on the focal-plane detector (FPD) the residual electron energy  $E_r$ , can then be determined. Therefore from the incident electron energy,  $E_e$ , the photon energy can be found by:

$$E_\gamma = E_e - E_r \quad (2.1)$$

A coincidence is required between the detected photo-reaction product and the recoiling electron in order to ascertain which photon causes the reaction(Fig.2.2). The rate of random coincidences depends on the instantaneous counting rates in the FPD and the reaction product detector(RPD),  $R_{random} \propto R_{FPD} \cdot R_{RPD}$ , both of which are roughly proportional to the instantaneous electron-beam intensity. Thus the tagging technique requires a high-duty-factor electron beam. For a pulsed beam, duty factor is defined as the ratio of the pulse duration to the time interval between pulses. For a given average beam current, instantaneous beam intensity is inversely proportional to duty factor.

In principle the tagged photon intensity is proportional to the FPD counting rate which can be measured accurately. Assuming the tagging magnet has very good intrinsic resolution the tagged-photon energy resolution is determined by the size of the individual elements of the FPD. Details of the photon tagging method for the present measurement will be given in following section.

It has to be mentioned that there are other methods of producing a quasi-monochromatic photon beam. When a positron beam, produced by bombarding a high- $Z$  target with electrons, is incident on a low  $Z$  target, electron positron annihilation produces a pair of photons each of energy 511 keV in the  $e^+, e^-$  cen-

tre of mass system. If the angle of the emitted photon is measured (which can be done by collimating the beam at an appropriate angle) it is possible to calculate its energy. The resulting photon beam contains both annihilation and positron bremsstrahlung components. The bremsstrahlung component has to be subtracted and is evaluated by producing electron instead of positron bremsstrahlung in a separate run. This method was used at the Saclay[31] and Livermore laboratories for photoneutron studies in the GDR region. However due to the low current of positrons, the photon flux is much lower than can be obtained with tagged bremsstrahlung.

In laser backscattering, laser photons at optical or ultraviolet(uv) wavelengths are scattered through  $\sim 180^\circ$  angle by energetic electrons (of a few GeV) circulating in a storage ring. The backscattered photon energy depends on the laser wavelength, the electron energy and the scattering angle. Normally this angle can not be determined accurately enough to give a reasonable photon energy resolution and the recoil electron must be momentum analysed to "tag" the photon. This method also gives low intensity compared to bremsstrahlung tagging, but is useful in polarized photon experiments as the polarization of the laser photon is essentially transferred to the backscattered photon.

## 2.3 The Max-Lab Tagged Photon Facility

A schematic view of the Max-Lab accelerator facility in Lund is shown in Fig.2.3. The Max accelerator consists of a 100 MeV racetrack microtron and a pulse stretcher/storage ring. A full description of the Max-Lab accelerator system can be found elsewhere[1]. Here it will be outlined briefly.

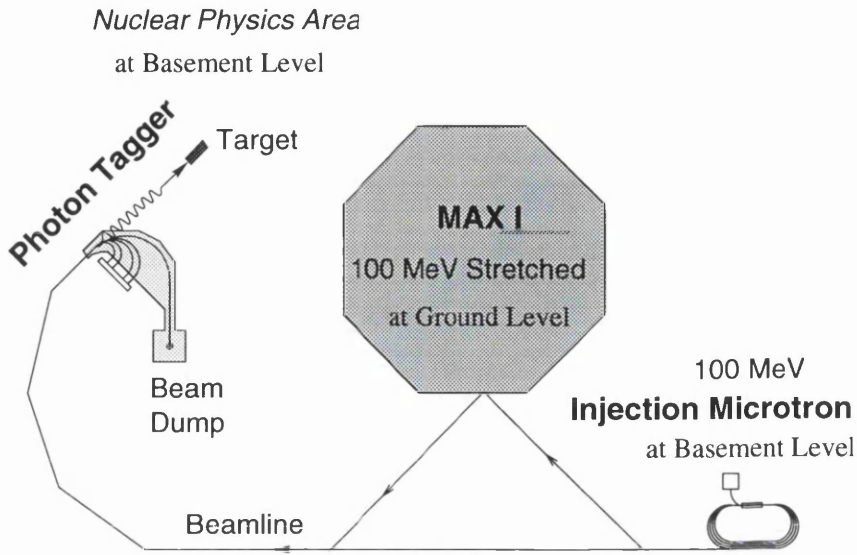


Figure 2.3: *Max-Accelerator in Lund(Sweden).*

### 2.3.1 The microtron and stretcher ring

The photon energy and flux are determined at Max-Lab by the bremsstrahlung tagging technique which requires a high-duty-factor electron beam. This is achieved by using a low-duty-factor microtron accelerator and a pulse stretcher ring. In tables 2.1 and 2.2 some features of the racetrack microtron and the stretcher ring are summarized. The microtron accelerates electrons to an energy of  $\sim 100$  MeV with an energy spread of 0.1 MeV. The energy used in the present work was 92.2 MeV. The electron beam emerging from the microtron has a pulse length of  $\sim 1 \mu s$  and a frequency of 50 Hz. The resultant duty-factor ( $5 \cdot 10^{-5}$ ) is much too small for photon tagging. In order to obtain a high-duty-factor, the beam is injected into a storage ring (32.4 meter circumference) and extracted gradually over the 20 ms period between injector pulses. This gives a macroscopic duty factor of up to  $\sim 80\%$ . This high duty factor electron beam of about 40 nA current is then steered to the nuclear physics area (Fig.2.4).

Max Energy	100 MeV
Pulse Current	10 mA
Pulse Length	0 – 1 $\mu$ s
Energy spread	0.1 MeV
Duty Factor	0.005%
Frequency	50 Hz

Table 2.1: *Racetrack microtron parameters [7]*

Electron Energy	75 – 100 MeV
Duty Factor	50 – 80 %
Extracted Current	< 100 nA
Current(inside the ring)	$\sim$ 100 $\mu$ A

Table 2.2: *Pulse Stretcher mode parameters [7]*

### 2.3.2 Tagging Spectrometer

The stretched electron beam is steered to the input of the tagging magnet (Fig.2.4) where it passes through an Al foil(radiator) of thickness  $50\mu\text{m}$  which produces bremsstrahlung photons. However most of the electron beam does not interact with the radiator and is bent by the spectrometer magnet into a beam dump consisting of borated water and a Faraday Cup to monitor the beam current.

The tagging spectrometer[1], placed behind the radiator, consists of a quadrupole-dipole (QD) system, with a maximum solid angle of  $\Delta\Omega = 22$  msr, and a 64 element electron FPD. The dipole design is of the Elbeck type which has the advantage of giving a straight focal plane. The FPD consists of 64 plastic scintillators. They are mounted in two groups(32 each), which can be moved

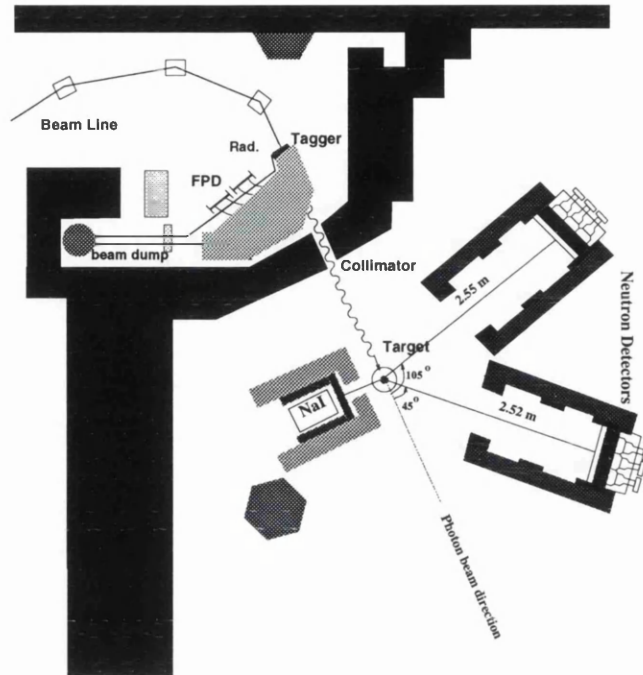


Figure 2.4: *Experimental area showing the tagger, neutron and photon detectors.*

independently along the straight focal plane to adjust the tagged range of the bremsstrahlung spectrum. Each FPD element is a 80 mm long NE102 plastic scintillator, connected via a light guide to a type R1635-02 8 mm photo-multiplier tube. The design of the focal plane scintillators and their associated high voltage, and discriminator circuits is based on one used at Mainz[43].

With a 95 MeV incident electron energy the focal-plane dispersion is 44 keV/mm so that each FPD scintillator covers  $\sim 300$  keV which defines the electron (and hence photon) energy resolution. Each FPD group spans a photon energy of  $\sim 9.5$  MeV. In this experiment the FPD was set up to tag photons in the ranges 49.6-58.8 MeV and 60.6 - 70.0 MeV.

### 2.3.3 Tagging Efficiency

An important quantity which must be measured in a tagged-photon experiment is known as the tagging efficiency. The tagging efficiency depends on the degree of proper alignment of the tagging system and is defined as the probability, given an electron is detected in the focal plane, of a photon passing through the collimator. The tagging efficiency is less than 1 is due to the collimation of the photon beam to a known size before interaction with the target.

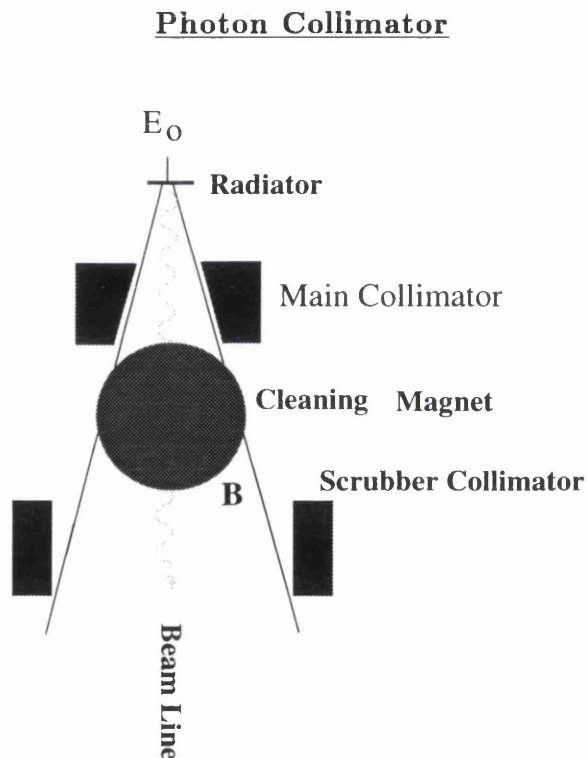


Figure 2.5: Schematic view of the collimation of the photon beam. The angle of divergence of the photon beam is exaggerated.

The photon beam was collimated by a 12 mm diameter collimator placed 1 m from the radiator in order to get a well-defined photon beam spot on the target (Fig. 2.4).

As shown in Fig.2.5 it consists of three parts:

- A tapered main collimator which defines the diameter of the photon beam.
- A cleaning magnet which deflects low energy electrons and positrons created in the main collimator
- A scrubber collimator to remove scattered photons and low energy electrons and positrons generated in the main collimator.

Polaroid photographic plates placed behind a metal converter were used to get an image of the collimated photon beam spot. The position of the central bright spot associated with the zero-degree peak of the bremsstrahlung angular distribution was used to check the alignment of the photon beam along the collimator axis.

### Tagging efficiency measurement

Tagging efficiency was measured periodically throughout the experiment using a large Pb/SCIFI(spaghetti) photon detector placed directly in the photon beam. The electron beam intensity was reduced to about 0.3% of the normal intensity to limit the counting rate of this detector, which has 100% photon detection efficiency.

A schematic diagram of the electronic setup and a typical ADC spectrum from the spaghetti detector are shown in figures (2.6) and (2.7) respectively. The OR of the FPD counters (Fig.2.6) triggered the data acquisition and was also used to gate the photon detector ADC.

The number of photons passing through the collimator and detected in the spaghetti detector  $N_\gamma$  was obtained by integrating the shaded region of the ADC

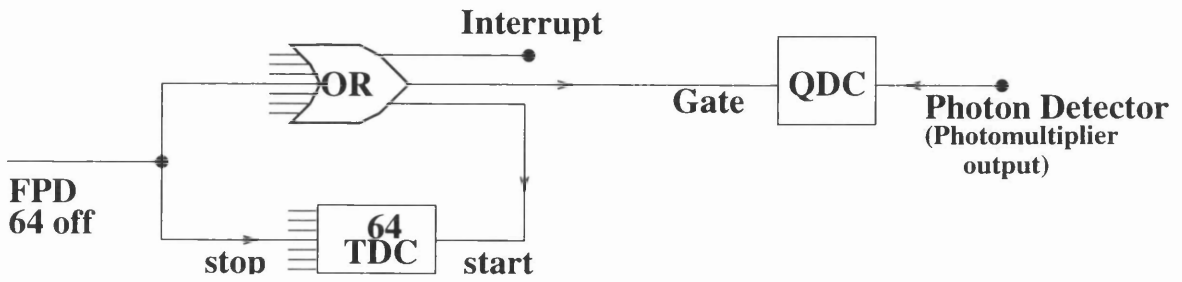


Figure 2.6: *Electronic circuit for the tagging efficiency measurement.*

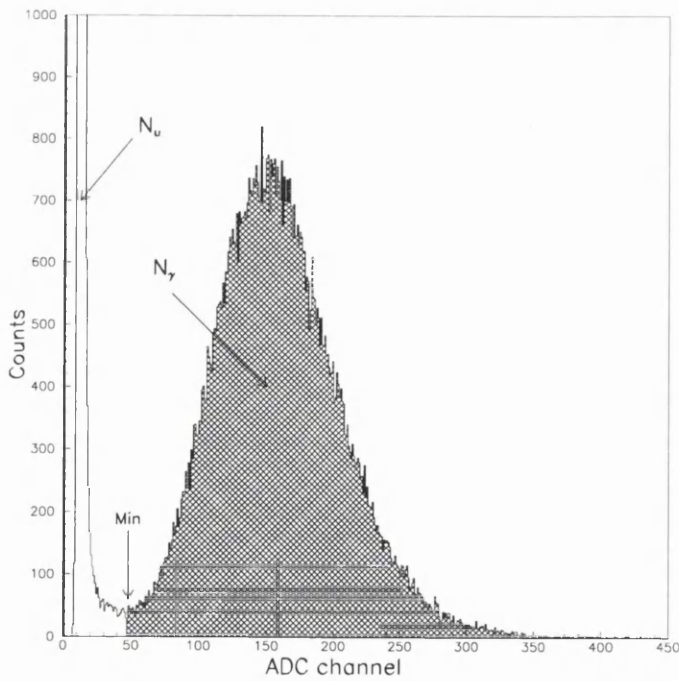


Figure 2.7: *ADC spectrum from the tagging efficiency photon detector.*

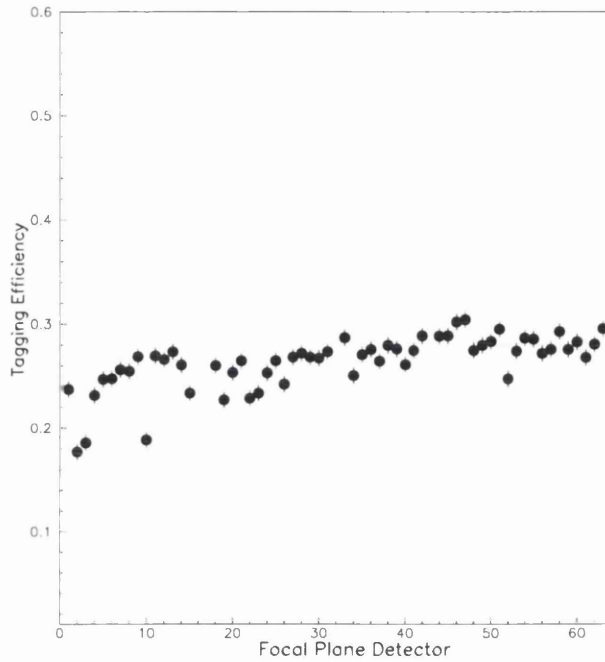


Figure 2.8: *Tagging efficiency measurement for each focal plane counter.*

spectrum(Fig.2.7). The number of tagged photons not detected,  $N_u$ , is registered in the pedestal(unshaded) region of the ADC spectrum. Tagging efficiency can be then obtained from the ratio

$$\epsilon_t = \frac{N_\gamma}{N_u + N_\gamma} \quad (2.2)$$

Fig.2.8 shows the measured tagging efficiency for the individual FPD counters. A Monte Carlo calculation of the tagging efficiency was made [1] using GEANT[17] subroutines. The calculated and measured tagging efficiencies for a  $50 \mu\text{m}$  Al foil and a 12 mm collimator, are shown in Fig.2.9. The observed difference between the measurement and calculation may be due to finite electron beam divergence, Møller electron scattering (which does not produce a photon) and multiple scattering in the radiator foil.

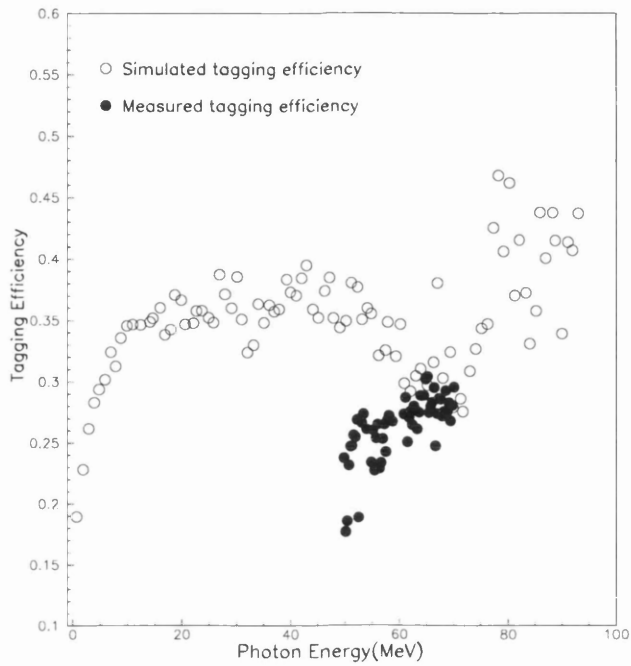


Figure 2.9: Calculated[1] and measured tagging efficiencies as a function of photon energy using 95 MeV electron beam.

### 2.3.4 The Photon beam monitor

A beam monitor was used to monitor the photon beam intensity during the run. As shown in Fig.2.10 it consists of three thin plastic scintillators each connected to a separate PM tube. The first scintillator was used to veto charged particles coming from the target. An Al foil was placed in front of the second scintillator in order to convert a fraction of the photons into  $e^+, e^-$  pairs which fire the second and third layer. This detector has a photon detection efficiency much less than 100% but it is stable. The rates from the 3 scintillator layers and from the logical combination  $2 \& 3 \& \bar{1}$  were continuously recorded in scalers and the ratio of  $\frac{2 \& 3 \& \bar{1}}{FPD}$  rates is related to the tagging efficiency.

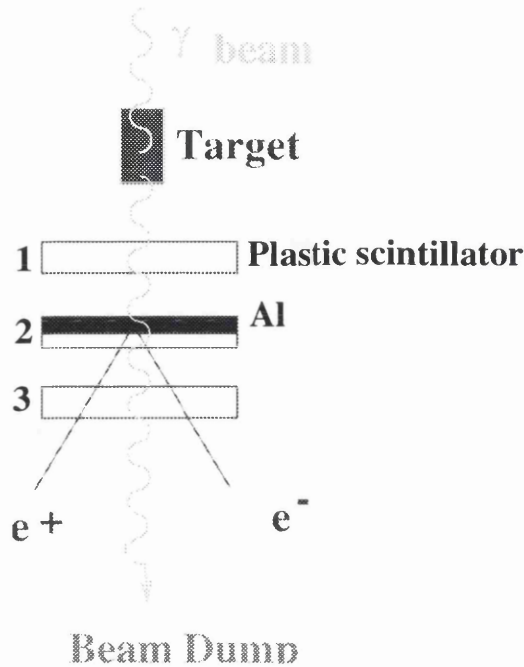


Figure 2.10: *Photon beam monitor.*

## 2.4 Time-of-Flight(TOF) Spectrometer

### 2.4.1 Principle of Neutron Detection

The neutron carries no charge and therefore has no coulomb interaction with the atomic electrons of the detecting medium. All neutron detectors utilize some type of nuclear conversion of the incident neutron into one or more secondary charged particles, which can then be detected directly. A neutron may interact elastically or inelastically with the nuclei of the detector material. In elastic scattering a fraction of the neutron energy is transferred to the recoil nucleus, dependant on scattering angle and nuclear mass. Energy transfer to the recoil nucleus is maximized when the recoil mass is minimized and therefore the  $H(n,p)$  scattering process is the most useful for converting neutrons to detectable, energetic charged particles(protons). Thus materials with a high hydrogen content such

as organic compounds are often used for neutron detection. Many compounds of this type scintillate, i.e. molecules excited by the passage of an energetic charged particle de-excite, producing photons in the visible or near-ultraviolet (uv) region. If the produced light is collected and amplified in a photomultiplier then an easily measurable electronic signal results. Many organic scintillators are non-linear whereby the amplitude of the light signal depends not only on the energy deposited but also on the velocity of an ionising particle. For a given energy a light, fast particle (eg. recoil p) produces more light than a heavy slow particle (eg. recoil  $\frac{A}{2}X$  nucleus) and thus is generally easier to detect. In organic scintillators inelastic  $n + {}^{12}\text{C}$  reactions involving charge exchange or break up also produce detectable charged particles and thus for neutrons of energy above reaction threshold these channels contribute significantly to the total light output. Contributions from  $n+p$  and various  $n + {}^{12}\text{C}$  reactions produce a pulse-height response which is a very complicated function of (and thus not a good measure of) neutron energy. Often time of flight (TOF) is preferred for energy determination (see section 2.4.4). Organic scintillators are also sensitive to gamma-rays which are detected via Compton and pair-production electrons. Related to the non-linearity in light output, a slow ion (p,d etc) produces relatively more slow decay scintillation components than a relativistic electron. This is observed in organic liquids and certain crystalline organic solids and may be used as a way of particle identification (see section 2.4.5).

## 2.4.2 Neutron Detector Construction

Two neutron detector arrays were built, each one (Fig. 2.11) consisting of an NE213-liquid-scintillator-filled aluminum tank of internal dimensions 60cm  $\times$

60cm×10cm. This is subdivided into nine cells, each 20cm × 20cm × 10cm, arranged in a 3X3 array. All inside surfaces of the tank were cleaned with solvent and painted with the high reflectance paint NE562. Glass windows, 196×196×10 mm, one for each cell, were glued on to a dural(Al alloy) window frame using high-vacuum epoxy. All cells were optically isolated although the liquid scintillator

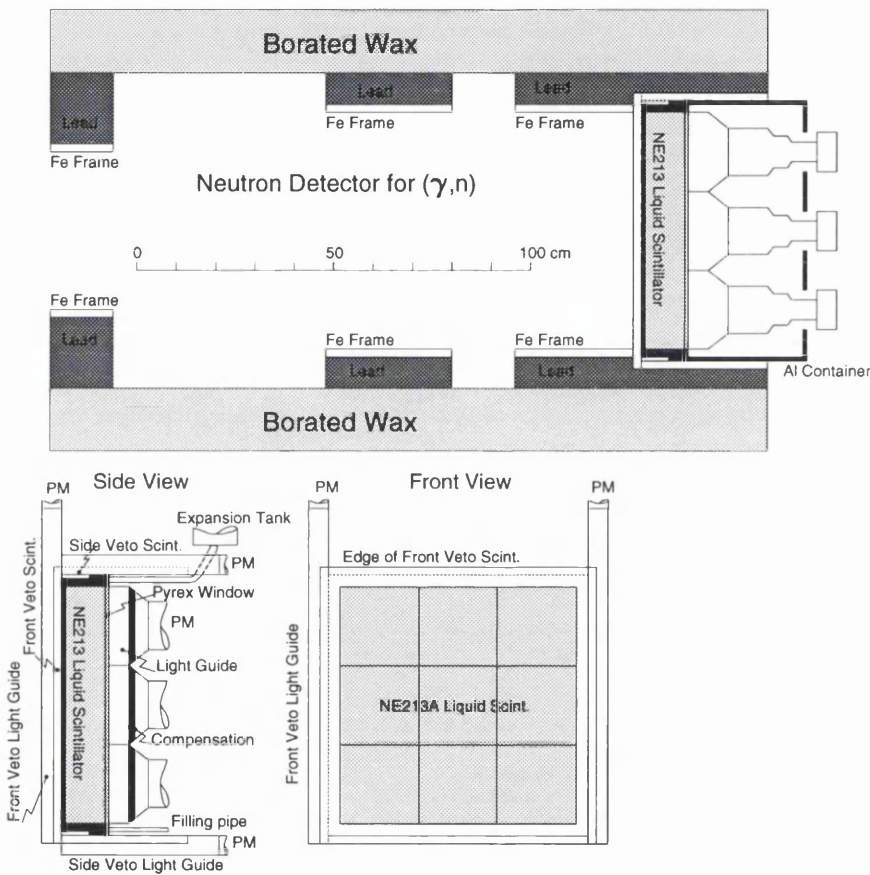


Figure 2.11: One of the two neutron detectors arrays showing shielding (upper) and details of the detector(lower).

was allowed to flow between different cells. Each cell was optically coupled, via a glass window and 100 mm thick lucite light guide, to a 130 mm diameter EMI type 9823KB photomultiplier(PM) tube.

Sheets of 2cm thick NE110 plastic scintillator around the liquid scintilla-

tor(Fig. 2.11), veto cosmic rays and any other charged particles incident on the detector. The plastic scintillator was coupled, via a fluorescent, wavelength-shifting light guide (NE172) to a 2" Philips PM tube, type XP2262B.

The entire apparatus is surrounded by lead, iron and borated wax shielding, and mounted on a steel table which can be positioned using airpads. More detail about the neutron detectors can be found elsewhere [11].

### 2.4.3 Electronics And Data Acquisition System

A diagram of the electronics required to convert the analogue signals from the detectors into digital words containing pulse height, time and scaler information is given in Fig.(2.12).

Anode pulses from the NE213 detectors are fed via 38 m of RG213, 50  $\Omega$  cable from the experimental cave to a separate counting room, where they are split 3 ways by a resistive network to produce inputs for a charge-integrating analog-to-digital-converter (QDC), a constant fraction discriminator(CFD) and a Pulse Shape discrimination (PSD) hardware module. The QDC digitizes the pulse amplitude, which is not used for neutron energy determination, but is necessary to calculate the neutron detection efficiency and also is useful for n/ $\gamma$  discrimination purposes(see section 2.4.5). The CFD module converts an analog signal into a logic signal and contains circuitry to compensate for walk in the trigger timing. The threshold of the module was set to  $\sim 4.4 \text{ MeV}_{ee}$  (MeV electron equivalent) for the present measurement, where  $E_\gamma \geq 50 \text{ MeV}$ . One output of the CFD, after suitable delay, drives the stop input of a time-to-digital converter(TDC) which shows which neutron detector(s) has fired. The PSD module, which is a vital piece of electronics, will be discussed in section 2.4.5. Signals from the veto de-



tectors are recorded in a QDC and fed to a CFD, whose trigger time is recorded in a TDC. The veto CFD outputs are OR'ed and used to inhibit the passage of NE213A CFD signals to the NE213A OR which generates all QDC and TDC starts. A latch circuit ensures that any triggers are inhibited when the system is busy. The PSD module takes  $0.56\mu\text{s}$  to identify the event to be either neutron in which case an interrupt to the data acquisition system is made, or a gamma ray in which case all ADC's are fast cleared.

Signals from the 64 scintillators of the tagger FPD are fed to dual-threshold discriminators and after delay they produce stop inputs for 64 FASTBUS based FPD TDC's, which are started by the NE213A OR. The neutron TOF information is recorded in the FPD TDC's which show Tagger-TOF (FPD-NE213A) coincidences. Input signals to the trigger system are inhibited when system is busy and during the 1 ms period during and after injection of an electron beam pulse into the stretcher ring.

The electronic circuit for the detection of decay  $\gamma$ -rays is shown in the insert of Fig.2.12. Signals from the detector were split two ways, one for a QDC and the other for a CFD, which drives a TDC stop (started by the NE213A OR). When a neutron is detected in the TOF spectrometer the pulse time and amplitude from a NaI  $\gamma$ -ray counter are recorded and  $(\gamma, n\gamma')$  events are signalled by triple, Tagger-TOF-NaI coincidences.

The values of all TDCs and QDCs are read out through CAMAC and FASTBUS and then transferred to a VME-Bus computer connected to a SUN workstation. Here they are written to an exabyte tape. Scalers were read out every 10 s, and were connected to the 64 focal plane counters, the electron-beam Faraday cup, neutron detectors, the  $\gamma'$  detector and the photon-beam monitor. A count-down timer records the timing of the event with respect to the accelerator

injection cycle.

#### 2.4.4 Neutron Energy Determination(TOF Method)

The pulse-height signal from a neutron detector is not usually suitable to determine neutron energy (see section 2.4.1). Alternatively it can be determined by measuring the neutron time-of-flight.

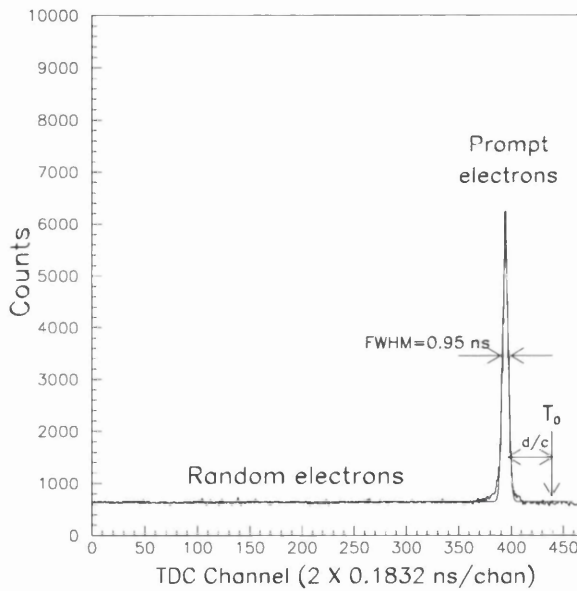


Figure 2.13: *Time-of-flight spectrum of relativistic electrons (arrow shows time-zero point in TDC).*

For a neutron with rest mass  $M_n(\text{MeV}/c^2)$  travelling along a flight path of length  $d(\text{m})$  in a time  $t_{tof}(\text{ns})$  the kinetic energy  $T_n(\text{MeV})$  of the neutron is given by the relativistic expression:

$$T_n = M_n \left[ \frac{1}{\sqrt{1 - \beta^2}} - 1 \right] \quad (2.3)$$

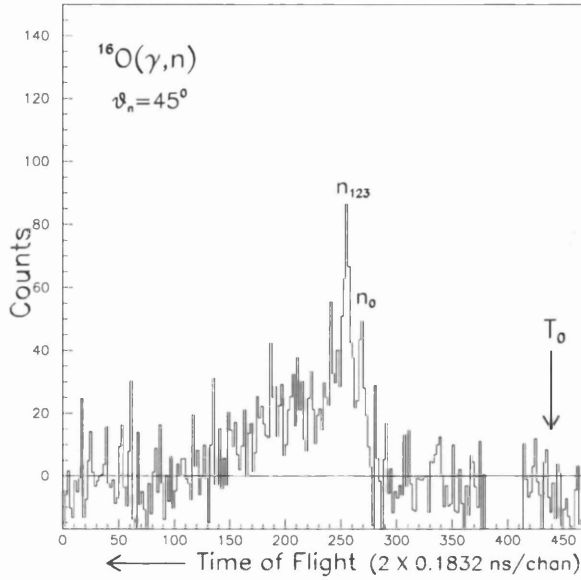


Figure 2.14: Neutron time-of-flight spectrum from the  $^{16}\text{O}(\gamma, n)$  reaction for the photon energy range of 51.9-53.7 MeV. The peak labeled  $n_0$  results from excitation of the  $^{15}\text{O}$  ground state while that labeled  $n_{123}$  results from unresolved  $^{15}\text{O}$  states at 5.2-6.2 MeV excitation.

$$\beta = \frac{v}{c} = \frac{1}{c} \cdot \frac{d}{t_{tof}} \quad (2.4)$$

$$t_{tof} = (t_n - t_0) \quad (2.5)$$

where;

$t_{tof}$  is the time difference between the neutron detector hit time ( $t_n$ ) and the time-zero ( $t_0$ ) point in the TOF spectrum, which corresponds to the time of neutron production in the target,

$M_n$  is the rest mass of the neutron,

$d$  is the distance of the detector from the target (flight path),

$c$  is the speed of light.

The time difference between a start signal from a neutron detector and a stop signal from the FPD is used to determine the time-of-flight of the neutrons. This time difference contains contributions from signal propagation delays in detectors and cables. In order to get the absolute flight time of the neutron, the  $t_0$  point was extrapolated from a measurement of relativistic electrons produced by tagged bremsstrahlung. For this, the forward veto detectors were put in coincidence with the NE213A detectors (as opposed to anticoincidence for normal running) and the PSD modules were disabled so that high-energy, light-speed electrons were selected. A resulting FPD TDC spectrum is shown in Fig.(2.13) where one can see a well-defined peak, whose full width at half maximum (FWHM) gives the time resolution of the detection system, sitting on a random background. The time-zero point is a time  $d/c$  earlier than the coincidence peak position (time runs from high to low channel). Under normal running conditions where neutrons are selected, the TDC spectrum of Fig. 2.14 results after subtraction of random coincidences. The gap after the time-zero point results from the subtraction procedure (see section 3.4.2). Peaks resulting from the  $^{16}\text{O}(\gamma, n_0)$  and  $^{16}\text{O}(\gamma, n_{123})$  reactions are clearly visible when the photon energy is restricted to a suitably small range. The continuum tail in the distribution results from unresolved higher excited states of  $^{15}\text{O}$  and from  $^{16}\text{O}(\gamma, pn)$  where the proton goes undetected. This TOF spectrum was obtained with a flight path of 2.5 m which gives a neutron kinetic energy resolution of  $\sim 3$  MeV. The best resolution obtainable at MAX-Lab is  $\sim 1$  MeV FWHM for  $\sim 40$  MeV neutrons, limited by the available flight paths ( $\leq 6$  m).

### Energy Resolution

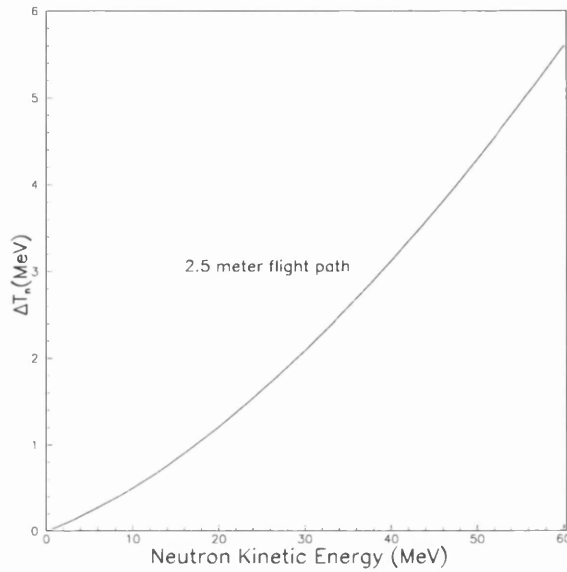


Figure 2.15: *Neutron resolution as a function of kinetic energy.*

In TOF measurements the energy resolution depends on the uncertainties in the measurement of time difference ( $\Delta t_{tof}$ ) and flight path ( $\Delta d$ ). The uncertainty of the neutron flight-time measurement is due to the intrinsic timing resolution of the neutron detector and the FPD's and to the time-pickoff accuracy of the electronics. The flight-path measurement uncertainty is mainly due to the target size and neutron detector thickness. The neutron kinetic energy resolution ( $\Delta T_n$ ) is then given by[37]:

$$\Delta T_n = \frac{\beta^2}{1 - \beta^2} (T_n + M_n) \sqrt{\left(\frac{\Delta d}{d}\right)^2 + \left(\frac{\Delta t_{tof}}{t_{tof}}\right)^2} \quad (2.6)$$

where  $T_n$  is the neutron kinetic energy,  $M_n$  is the neutron mass (939.56 MeV)  $d$  is the flight path,  $\Delta d$  is the uncertainty of the flight path,  $t_{tof}$  is the flight time of the neutron, and  $\Delta t_{tof}$  is the uncertainty of the neutron flight time. In Fig.2.15

the energy resolution is given as a function of neutron kinetic energy for a 2.5 meter neutron flight path.

### 2.4.5 Particle Identification (PSD Method)

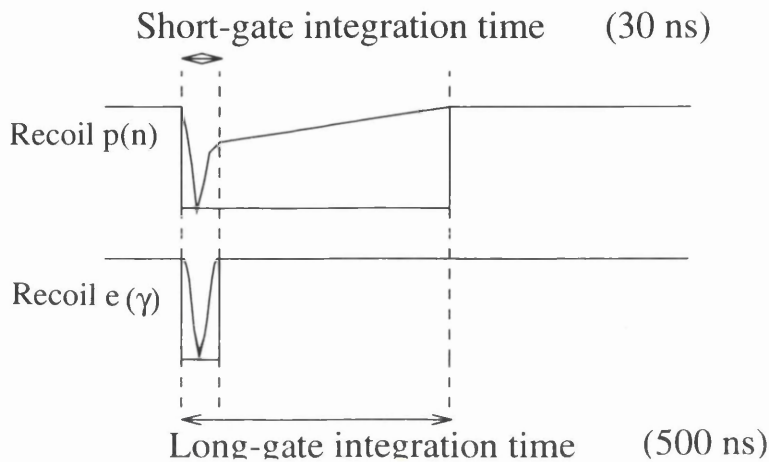


Figure 2.16: *Pulse-shape signals from NE213 for neutrons and gamma-rays.*

As was mentioned earlier, charged particles (electrons, protons etc) incident on the neutron detectors were vetoed by forward plastic scintillators. However chargeless particles (photons and neutrons) can not be differentiated using this technique. Since the liquid scintillator is sensitive to  $\gamma$  rays as well as neutrons, one major difficulty encountered in the detection of neutrons is the large background of energetic  $\gamma$  rays. A widely used method for discrimination between the scintillations due to neutrons and  $\gamma$  rays in liquid organic scintillators is the Pulse Shape Discrimination (PSD) method.

Scintillations in certain liquids have several decay components which result from different molecular de-excitation processes. The effective shape of the scintillation pulse depends on the velocity of the interacting particle. Fast particles (relativistic electrons) produce relatively little of the long-decay-time components

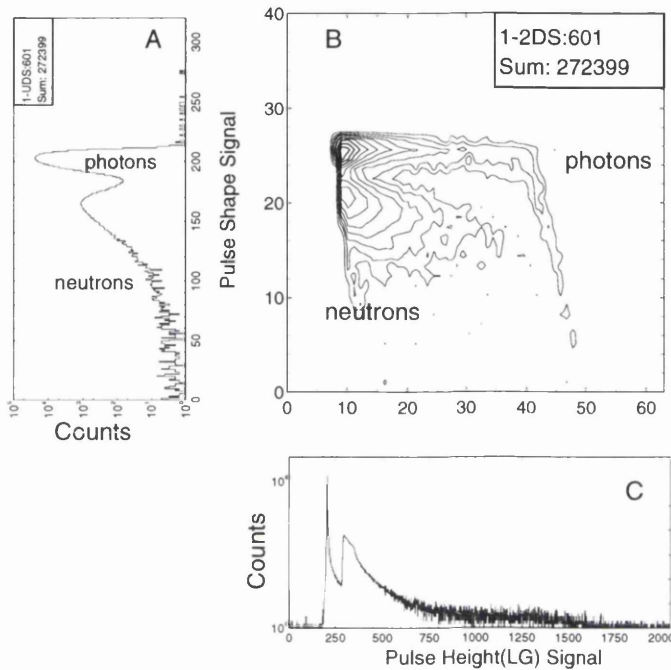


Figure 2.17: Neutron-gamma discrimination by the PSD method. (The tail on the photon band of the scatter plot is the result of a saturation effect in the PSD box)

compared with slower and more heavily ionising particles (protons). Therefore it is possible to separate out the neutron signals from the gamma signals by analysing the shape of the emitted light pulse (Fig. 2.16). As commercially available PSD modules (e.g. the Link Systems P.S.D 5010) were too slow for the present measurements, a module working on similar principles but capable of handling counting rates up to 500 kHz was designed in Glasgow University [8]. The anode signal from the liquid scintillator is split and fed to two charge integrators, one of which is provided with a 30 ns gate to integrate fast components and the other with a 500 ns gate to integrate both slow and fast components.

The timing of these gates with respect to the anode signal is shown schematically in Fig.2.16.

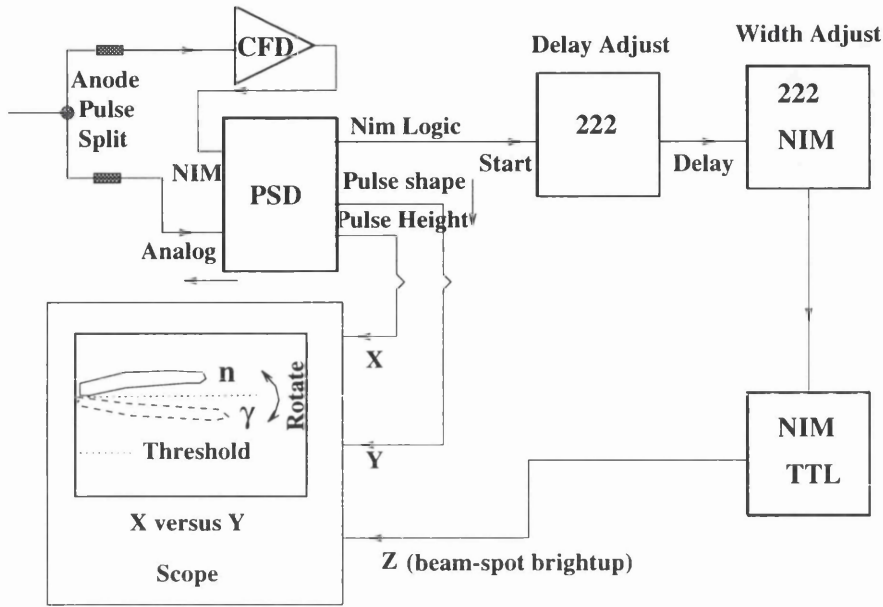


Figure 2.18: PSD setting procedure.

The voltages from the integrators are fed to a difference amplifier whose output voltage, the so-called pulse-shape (PS), is defined as:

$$PS = LG - k \cdot SG + C \quad (2.7)$$

Where LG is the voltage from the long-gate integrator, SG is the voltage from the short-gate integrator,  $k (< 1)$  is a constant which is determined by a variable attenuator and C is a variable DC offset applied as a DC current at the integrator inputs. If PS (Fig. 2.17A) is plotted against pulse height (Fig. 2.17C) separated loci related to neutrons and photons can be seen in the two-dimensional plot (Fig. 2.17B). In this plot the PS axis has been compressed by a factor of 8 and the pulse height axis has been compressed by a factor of 32.

Before using the module, it has to be setup correctly, initially using a Pu-Be  $n/\gamma$  source[50] and the setup shown in Fig.2.18. This fast initial setup uses an

oscilloscope operated in X-Y mode instead of a computer display. The parameters  $k$  and  $C$  (in equation 2.7) are varied on front-panel potentiometers so that the bulk of the  $\gamma$ 's are rejected, but no neutrons are rejected. The module is fine tuned using beam and online computer two-dimensional plots (Fig.2.17).

### 2.4.6 Neutron Detection Efficiency

Since neutron detection requires a nuclear interaction, the neutron detection efficiency

$$\epsilon_n = \frac{\text{neutrons registered}}{\text{neutrons incident}} < 1 \quad (2.8)$$

An accurate knowledge of the detection efficiency is an important prerequisite for absolute neutron flux measurement with organic scintillation counters.

Because the interaction probabilities (cross-sections) between incoming neutrons and nuclei vary with different detector materials and different neutron energies, the efficiency is a function of neutron energy, detector material and detector dimensions. The size of the detector is important as sufficient material must be in the path of the neutron in order to provide a reasonable probability of interaction. Neutron detection efficiency can be increased by using a thick detector, but it is more difficult to achieve uniform light collection from a large volume scintillator and the energy resolution will worsen as the neutron flight path uncertainty increases.

For the present experiment the neutron detection efficiency was calculated using the Monte-Carlo code STANTON[23]. STANTON uses measured cross-sections for  $H(n,p)$ ,  $^{12}C(n,3\alpha)$   $^{12}C(n,p)$  and other  $n+^{12}C$  reaction channels to calculate the detector response for a given neutron energy, hit position and hit

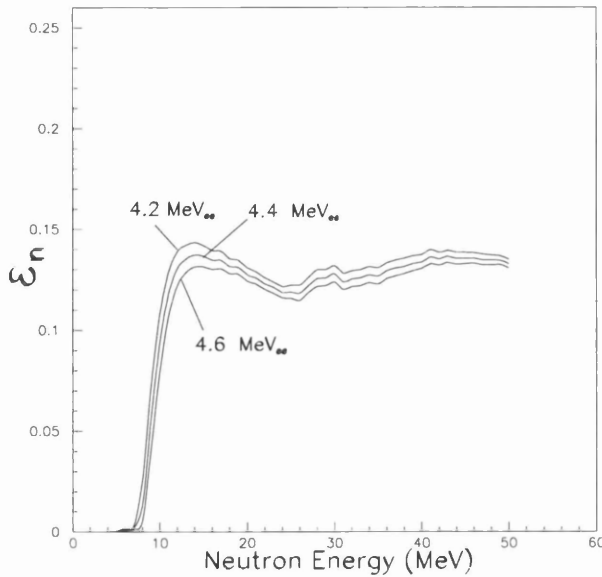


Figure 2.19: *Neutron detection efficiency as a function of neutron energy. The three lines show the effect on efficiency as the detection threshold is varied.*

direction. However the code does not include the  $^{12}\text{C}(n,d)$  reaction channel. The calculated detection efficiency was checked using two other Monte-Carlo codes [30, 29] which include the  $^{12}\text{C}(n,d)$  reaction channel. They give values for the efficiency smaller than STANTON[5]. Fig.2.19 shows a sample STANTON calculation for a  $20 \times 20 \times 10$  cm NE213 liquid scintillator and neutron energies 5-50 MeV. The effect of small uncertainties in the detection threshold, possibly caused by pulse-height calibration uncertainties or inaccuracy in the (non-linear) proton response curve (equation 2.9) are shown.

### Pulse-height Calibration

For the calculation of neutron detection efficiency, the detection threshold of the recoil charged particle has to be known. This requires calibration of the pulse-

height signal. The neutron detection threshold energy is determined in hardware by the threshold level set in the associated CFD (see sec 2.4.3) and in software by cuts made on NE213 detector, pulse-height spectra during offline analysis. Pu-Be n/ $\gamma$ [50], Pu-Be surrounded by teflon ( $C_2H_2F_4$ ),  $^{60}Co$  and  $^{228}Th$  sources were used to calibrate the relationship between pulse-height in spectrum channel and recoil electron energy. The non-linear response of the NE213 liquid scintillator to protons is usually expressed in terms of the linear equivalent electron energy using the empirical expression [90]:

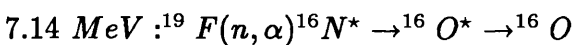
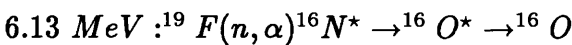
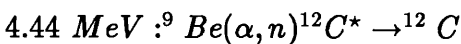
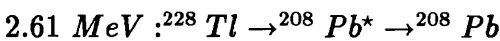
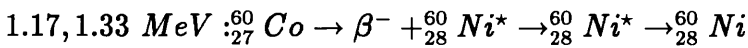
$$E_e = 0.83 \times E_p - 2.82 \times (1 - e^{-0.25 \times E_p^{0.93}}) \quad (2.9)$$

where the parameters were determined from fits to measured proton response. According to this expression an 8.16 MeV proton induces for example a pulse in the scintillator equivalent in height to a pulse induced by a 4.4 MeV electron. At low energy the interaction of  $\gamma$ 's in the liquid scintillator is mainly by Compton scattering.

The Compton edge (maximum possible) electron energy is given by

$$E_e = \frac{E_\gamma}{1 + \frac{m_0 c^2}{2E_\gamma}} \quad (2.10)$$

Fig.2.20A shows Compton electron energy spectra taken with various sources. Edge determination follows the method of Knox et al [52]. The  $\gamma$ -ray lines employed for the calibration were as follows:



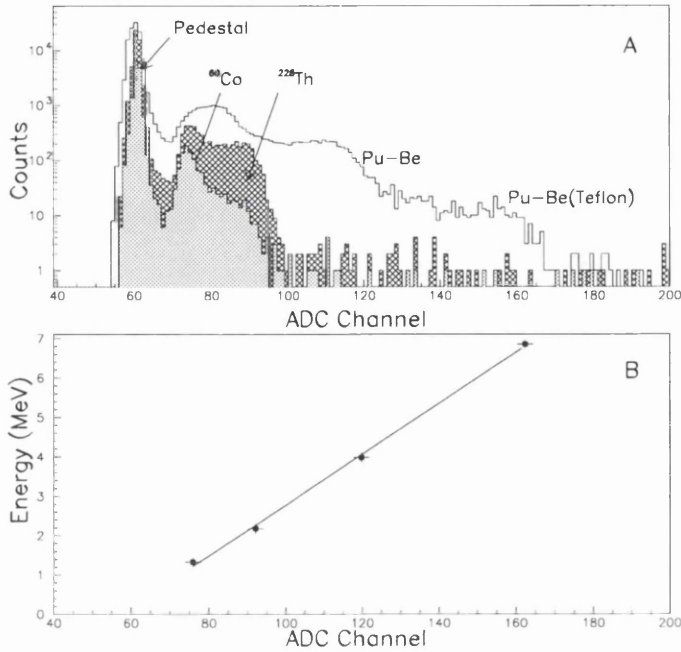


Figure 2.20: Neutron detector pulse-height spectra from  $^{60}\text{Co}$ ,  $^{228}\text{Th}$ , Pu-Be sources in A and a linear fit of energy against channel number in B.

The two highest lines are produced by neutron interactions with fluorine (F) in the teflon. A linear fit of the Compton edge versus observed channel number (Fig. 2.20B) gives the calibration.

## 2.5 The NaI(Tl) Detector

When studying  $(\gamma, N)$  reactions it is important to have the best possible energy resolution. Using the longest possible (6m) flight path at Max-Lab one can get  $\sim 1$  MeV FWHM which is often not fine enough to separate discrete states in the A-1 system left after nucleon knockout. A-1 excited states may also be identified by detection of their decay  $\gamma$ -rays and in this case the experimental resolution is

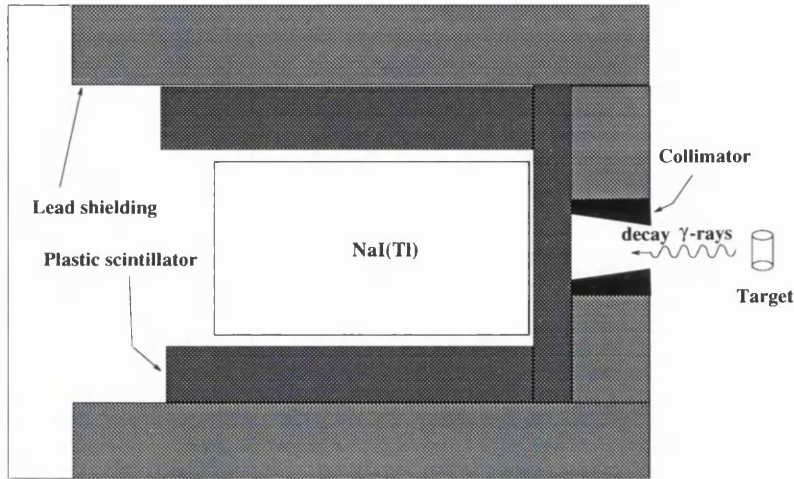


Figure 2.21: A schematic view of the NaI(Tl) photon detector.

given by the resolution of the  $\gamma'$  detector. Following a pioneering measurement of  $^{12}\text{C}(\gamma, p\gamma')$  at Max-Lab [55], the feasibility of a  $(\gamma, n\gamma')$  measurement, which is more difficult as it requires the simultaneous detection of two neutral particles, has been tested. This has been done in a triple coincidence  $(\gamma, n\gamma')$  measurement where the decay  $\gamma'$  were detected by a  $25.4 \times 25.4$  cm NaI(Tl) scintillation detector (Fig.2.21). A thin plastic detector, placed in front of it vetos incident charged particles. Lead surrounds the detector to shield it from background in the "target cave" and a front collimator ensures that only a 15 cm diameter spot is illuminated on the detector. Using this technique, which had not been used previously in a photoneutron experiment, an energy resolution of  $\sim 200$  keV was thought possible for the states of interest, a factor 5 better than is possible with  $(\gamma, n)$ . The full energy peak efficiency of the NaI detector is 60 % when illuminated by 6 MeV photons through the front collimator, as calculated in a GEANT simulation[11].

### 2.5.1 Pulse-height Calibration of NaI

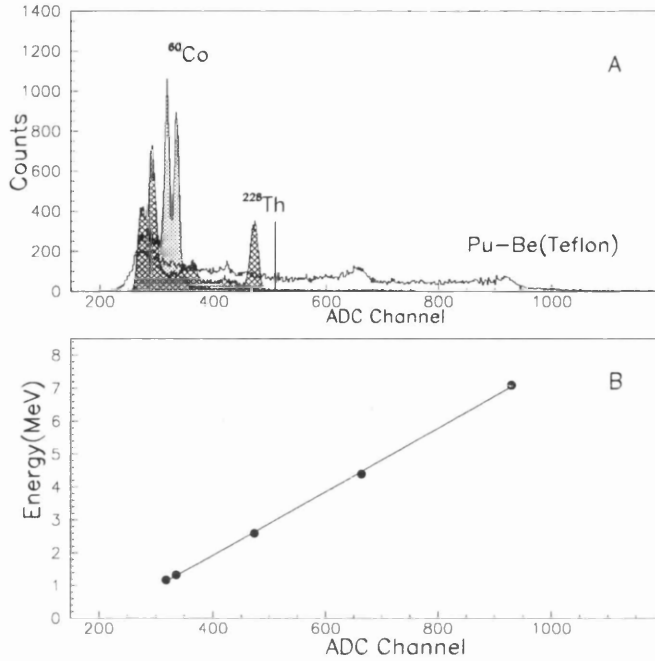


Figure 2.22: Calibration of NaI detector with Co,Th,Pu-Be source(A) and corresponding linear fit(B).

The pulse-height from the NaI(Tl) detector should be proportional to the energy deposited by photons. Pulse-height calibration was done using  $^{60}\text{Co}$ (1.17,1.33 MeV), Th(2.6 MeV), Pu-Be(4.4 MeV) and Pu-Be+Teflon(7.1 MeV) sources. Since 6.1 MeV was not resolved this point was not used in the calibration procedure. Figure(2.22A) shows calibration spectra where  $\gamma$ -ray lines are clear at 1.17,1.33,2.6,4.4 and 7.1 MeV and a linear fit of peak energy versus peak channel is shown in Fig.2.22B.

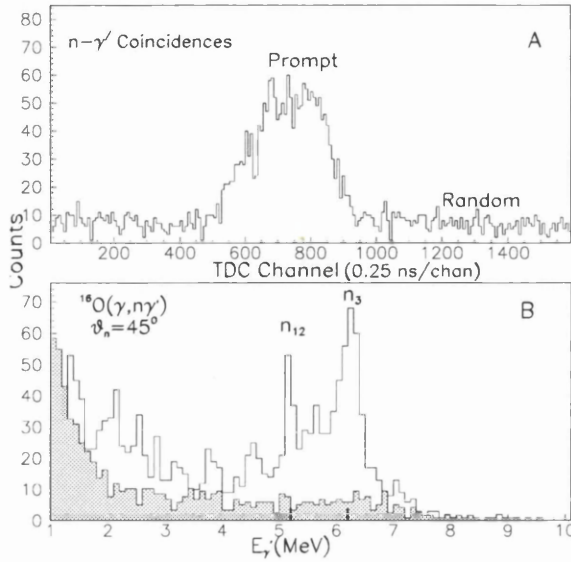


Figure 2.23: *A:  $n$ - $\gamma'$  coincidence time spectrum, B:  $\gamma'$  energy spectrum obtained after  $n$ - $\gamma'$  coincidences were selected (Shaded area shows the contribution of random coincidences).*

### 2.5.2 NaI(Tl) Timing and $n$ - $\gamma'$ coincidences

Since NaI(Tl) is a very efficient  $\gamma$ -ray detector it is very sensitive to backgrounds produced by the electron and photon beam. Therefore the  $\gamma'$  produced in the target have to be isolated. A TDC which was started by the neutron detectors, and stopped by the NaI was used to determine whether the neutron and photon detectors simultaneously fired or not. Fig.2.23A shows coincidences between  $\gamma'$  detected in the NaI and neutrons detected in TOF. A corresponding NaI pulse-height spectrum, after selection of coincidences, is shown in Fig.2.23B, where the 5.2 and 6.2 MeV excitations are clearly seen. Tagger coincidences were not required and most of the counts result from relatively low energy bremsstrahlung photons. The random contribution to the energy spectrum was obtained by mak-

ing a cut on the random coincidence part of the NaI TDC (Fig.2.23A) spectrum. In Fig.2.23B the random contribution is shown in the shaded area.

## 2.6 Targets

Li,  $D_2O$  and  $H_2O$  targets were used for the present measurements at Max-Lab. The  ${}^6\text{Li}$  target was a cylinder 5 cm long by 4 cm diameter prepared by the *Central Bureau voor Nucleaire Metingen* in Geel (Belgium). It encased in a thin Al can to prevent oxidation of the metal. The water targets had dimensions of 6.7 cm  $\times$  9 cm and were contained in thin aluminium cans. An empty can was used to estimate background contributions. The targets were placed with their axes centered on the photon beam axis and aligned parallel to it.

# Chapter 3

## Data Analysis

### 3.1 Introduction

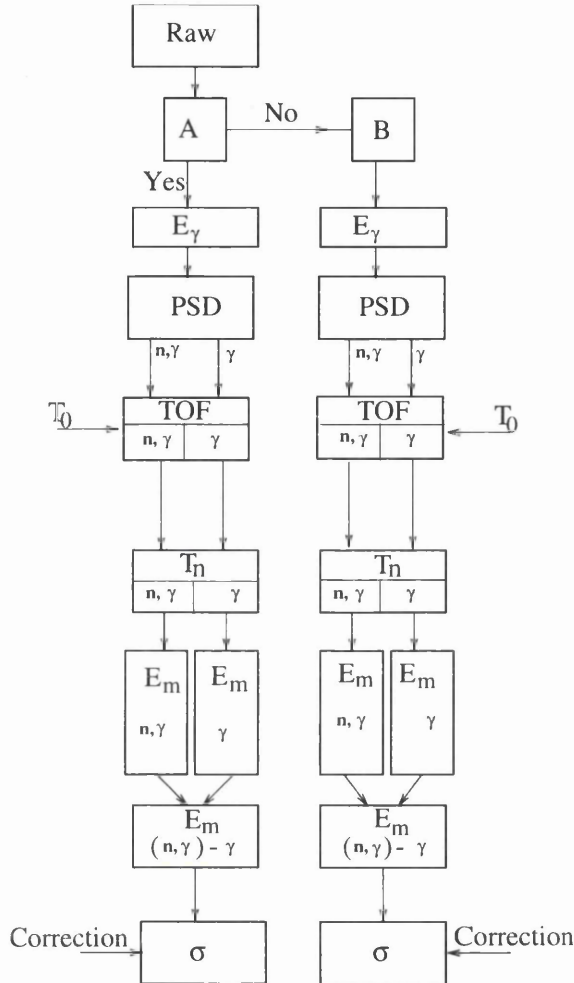


Figure 3.1: *Flowchart of data analysis (A and B relate to the two neutron detector arrays).*

In this chapter the data analysis procedures for  $(\gamma, n)$  experiments will be described. The data taken at Max-lab were analysed using Glasgow University Nuclear structure group computer facilities. The main analysis programs were ACQU [10], used to convert from raw QDC and TDC values to physical quantities and Physics Analysis Workstation(PAW) [72], the Cern-written software package. Most of the analysis described here was performed using ACQU C-written

uds (user-defined spectrum) functions, written specifically to handle  $(\gamma, n)$  experimental data and linked to the main kernel of the ACQU software system. Since all events from the two different neutron detector arrays were recorded simultaneously the first step of data analysis was to split the data in two parts according to which neutron detector fired(Fig.3.1).

The main steps in the data analysis of  $(\gamma, n)$  reaction data, as shown in Fig.3.1, are:

- Determine the photon energy
- Separate neutron events from photons (PSD)
- Determine the neutron kinetic energy (TOF)
- Determine the missing energy of the residual system on the basis of two-body kinematics.
- Determine the cross-sections for the population of different states in the residual nucleus and determine experimental uncertainties.

## 3.2 Photon Energy

The tagged photon energy was obtained from the hit position of the associated recoil electron on the tagger Focal Plane Detector (FPD) (see sec2.2). Figure(3.2) shows how photon energy is related to the 64 FPD counters for an electron energy of 92.2 MeV and with the FPD arrays positioned for maximum tagged photon energies. The FPD TDC's which recorded the time relation between neutron-detector hits and FPD hits were used to determine which FPD channels showed a coincidence hit. The distribution of number of hits across the FPD is

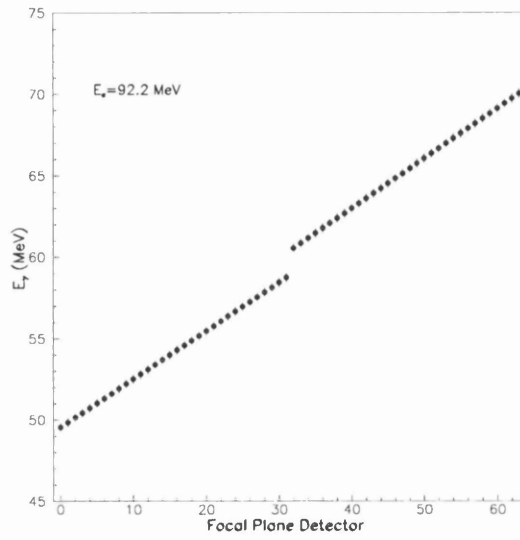


Figure 3.2: *The relationship between Photon Energy and FPD counter.*

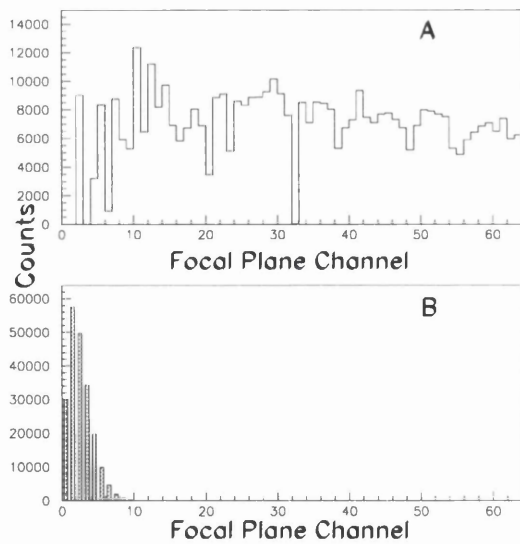


Figure 3.3: *Numbers of coincident hits in the FPD counters in A and multiplicity distribution of FPD counters in B.*

shown in Fig.3.3A. Normally several hits (Fig.3.3B) were recorded in each event with the average multiplicity dependent on the detector counting rates and the selected width of the coincidence time window. Each hit, possibly representing a different photon energy, was stored and analysed separately in the subsequent reconstruction of the event kinematics. In Fig.3.3A the irregular distribution results from uneven gains in the FPD resulting in varying electron detection efficiency. Some FPD channels did not work.

### 3.3 PSD Analysis

The PSD technique, as described in section 2.4.5, was used to perform identification of neutrons and gammas. For each individual neutron cell, the pulse height and pulse shape are digitized and stored. A typical two-dimensional plot of pulse shape versus pulse height in Fig.3.6 shows clear separation of neutron and gamma-ray events.

Each time a cell fires the others are also read out and this "empty readout" produces the peak labeled pedestal in Fig.3.4. This was removed by applying a condition that the particular cell fires giving the distribution of Fig.3.5. This spectrum can then be plotted against pulse-height giving the two-dimensional contour spectrum as shown in Fig.3.6.

Although it is possible to reject gammas in the offline analysis using a one dimensional pulse-shape spectrum (Fig.3.5), it is better to do it in a two-dimensional scatter plot (see Fig.3.6). This is because the pulse-shape signal is not always linear along the whole pulse-height region and if the module is not setup correctly the photon bands can be rotated (see section 2.4.5) off the horizontal.

The quality of the  $n/\gamma$  separation can be parametrised by using a Figure-of-

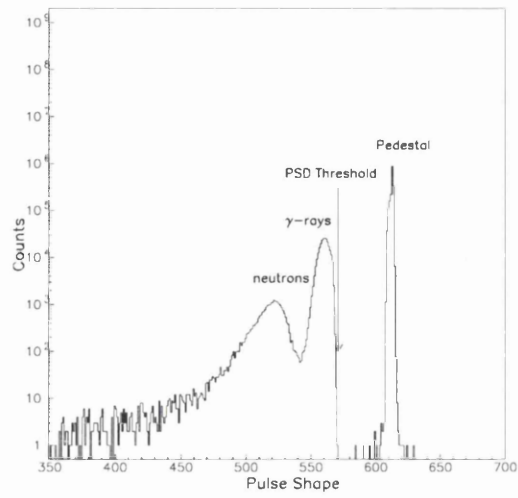


Figure 3.4: *Raw Pulse Shape spectrum showing with pedestal.*

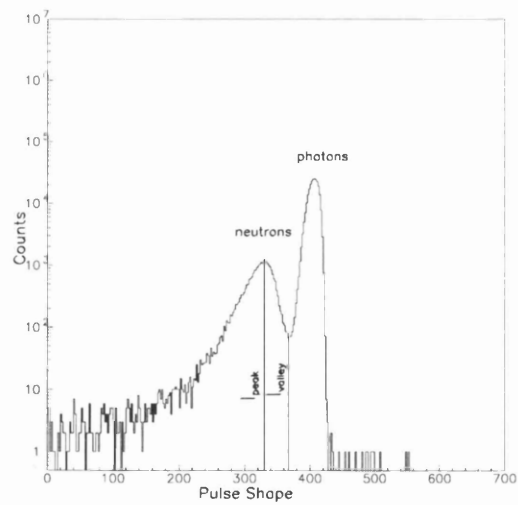


Figure 3.5: *Pulse Shape spectrum without pedestal.*

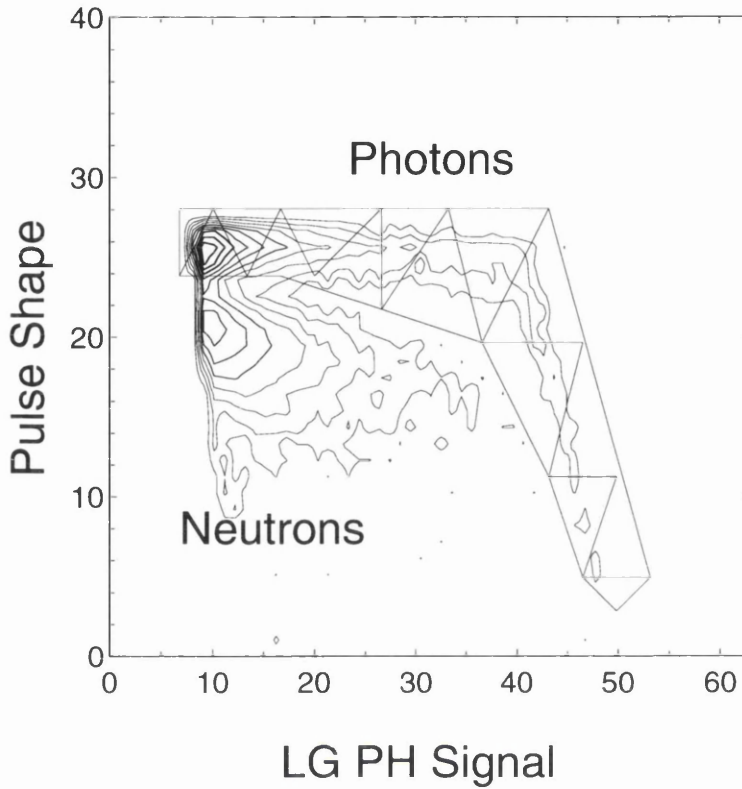


Figure 3.6: A PSD scatter plot, showing the selection region of photons.

Merit(FoM) which is defined as the ratio of the peak-to-valley of the pulse shape spectrum viewed in one dimension (Fig.3.5).

$$FoM = \frac{I_{peak}}{I_{valley}} \quad (3.1)$$

The FoM for the 16 working cells of detectors A and B are shown in table 3.1 where it can be seen that A is on average better than B. Since B was placed at a more forward angle than A, it sees more gamma rays with respect to neutrons. This may partially explain the better peak/valley performance of A. However it is also likely that the liquid scintillator in A is in better condition. Fluctuations in individual cells are more probably due to variations in photomultiplier and

Cell	A1	A2	A3	A4	A5	A6	A7	A8	A9
FoM	3.55	18.19	2.08	10.	17.1	2.04	2.08	7.9	13.
Cell	B1	B2	B3	B4	B5	B6		B8	
FoM	1.06	5.19	3.9	2.34	1.31	3.62		1.9	

Table 3.1: *FoM for each cell*

electronics performance.

## 3.4 Neutron Time-of-Flight Calibration

Neutron energy is determined by TOF which is recorded in TDC's, started by the neutron detectors and stopped by the post-bremsstrahlung electron FPD detectors.

Time-to-channel conversion was calibrated using an ORTEC 462 time calibrator set to provide stop pulses at  $n \times 20$  ns intervals after the start where  $n$  is a "random" integer. Fig.3.7A shows a typical TDC calibration spectrum and Fig.3.7B a linear fit of time against channel. The gradient gives the TDC conversion gain which is shown in Fig.3.8 for all 64 FPD TDC's.

### 3.4.1 Time-Zero Calibration and Alignment

TOF spectra have 16 possible starts (from the A and B detector) and 64 possible stops (from the FPD) and each of the  $16 \times 64$  start-stop combinations will produce a time-zero peak (section 2.4.4) in a slightly different position due to slight differences in particle trajectories and propagation delays through electronics. It is desirable in the offline analysis to align all time-zero's to fall at the same

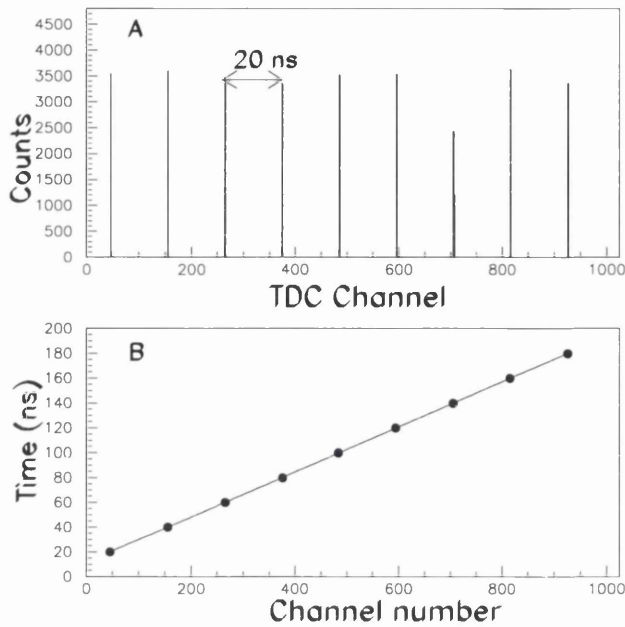


Figure 3.7: *Ladder TDC calibration spectrum calibration and corresponding linear fit.*

channel.

The first step is to select a single cell in the TOF array and locate the prompt electron peak in each of the 64 FPD TOF spectra, giving the FPD alignment offsets. Using these an OR FPD time spectrum is generated for each A-B element, yielding the A-B alignment offsets. The FWHM of the FPD time-zero peaks give an indication of the time resolution of the system. These are shown in Fig.3.9. Once the TOF spectra were calibrated and aligned, the reaction kinematics could be determined from the neutron kinetic energy, angle and the photon energy. TOF was reconstructed for each neutron cell which registered a hit (usually 1 cell only) and for each FPD channel which registered a hit (usually  $> 1$  hits), resulting in spectra of the type displayed in Fig.3.10. The contents of the spectrum arise

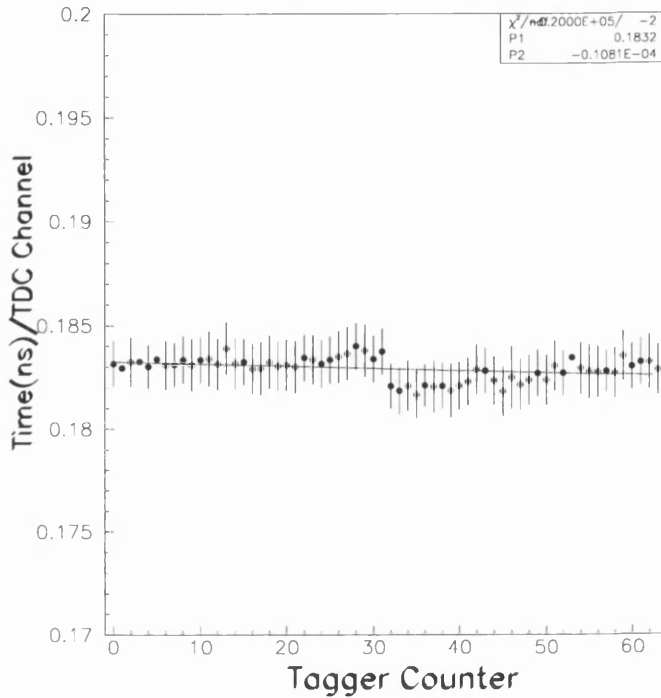


Figure 3.8: *Time Calibration of all Ladder TDC channels.*

from three sources:

- Neutrons from the target produced by tagged photons, which give the structured region between channels 120 and 280 in Fig.3.10 (unshaded histogram).
- Neutrons from the target produced by untagged photons which make random coincidences with the FPD. These give the essentially flat background on which the forementioned structure sits.
- Neutrons from non-target material (target holders, air, beam dumps, beam lines etc. in the reaction cave) which may be produced by tagged or untagged photons. This contribution was evaluated in separate "empty target

holder” runs and in nearly all cases was found to be negligible compared to ”target in” runs.

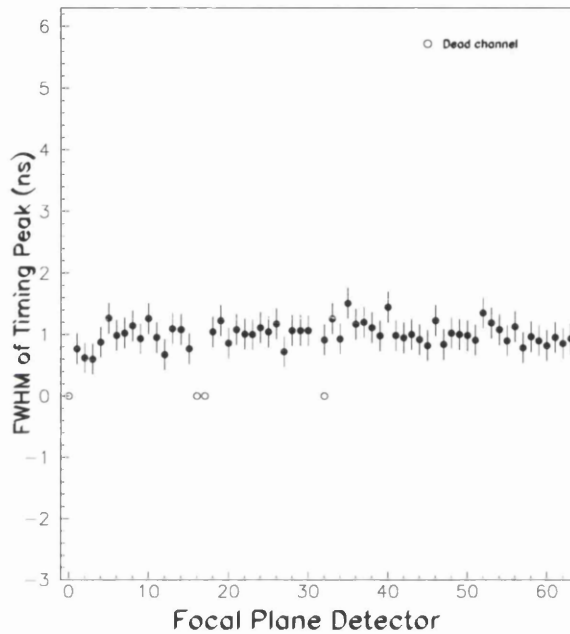


Figure 3.9: *Time resolution corresponding to each FPD Counter. (Single neutron detector B<sub>4</sub> used for start detector).*

### 3.4.2 Random Subtraction

For the purpose of random subtraction a purely random spectrum should be produced. A good approximation to a random spectrum may be obtained by selecting photons instead of neutrons by PSD (Fig.3.6) but otherwise reconstructing the TOF spectrum as before. This was possible because the PSD modules were adjusted to allow some detected photon events to be recorded. Fig.3.10 (shaded histogram) shows the resulting TOF spectrum which has been normalized to

give the same integrated counts as the unshaded spectrum in channel regions 0-100 and 275-375 where no structure is observed. The prominent peak in the photon "TOF" spectrum falls in the same channel as the time-zero calibration peak (Fig.2.13).

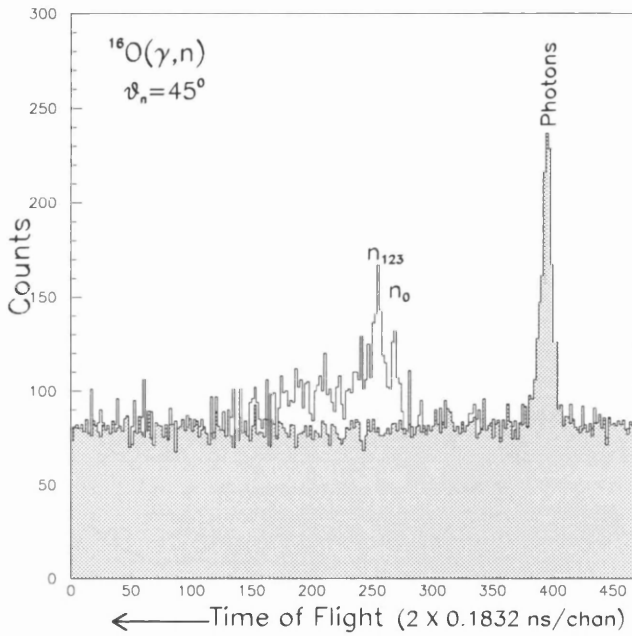


Figure 3.10: *TOF spectrum of neutrons (open area) and random contribution (shaded area).*

### 3.5 Missing Energy Spectra

The missing energy for a  $(\gamma, n)$  reaction is given by

$$E_m = E_\gamma - T_n - T_{recoil} = -Q + E_x \quad (3.2)$$

where  $E_\gamma$  and  $T_n$  are the energy of the tagged photon and the detected neutron

respectively,  $Q$  is the threshold energy for the reaction and  $E_x$  is the excitation energy of the  $A-1$ , residual nucleus.  $T_{recoil}$  is the recoil kinetic energy of the residual nucleus and is calculated from  $E_\gamma$  and  $T_n$  utilizing the conservation of energy and momentum (see appendix A).

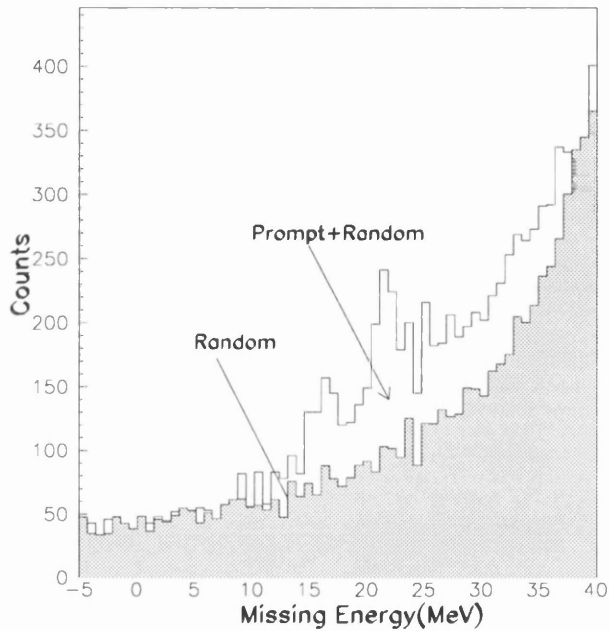


Figure 3.11: Missing energy spectrum related with Fig. 3.10 (shaded area shows the random contribution).

When the data are converted from TOF to missing energy the spectra of Fig.3.11 are produced where the unshaded and shaded histograms result from the equivalent TOF histograms of Fig.3.10. Fig. 3.12 shows a random subtracted missing energy spectrum, for a 51.2-56.0 MeV tagged-photon energy region and  $45^\circ$  neutron detection angle, for the  $^{16}\text{O}(\gamma, n)^{15}\text{O}$  reaction. The peak at  $\sim 15.7$  MeV is due to the residual  $^{15}\text{O}$  nucleus being left in the ground state.

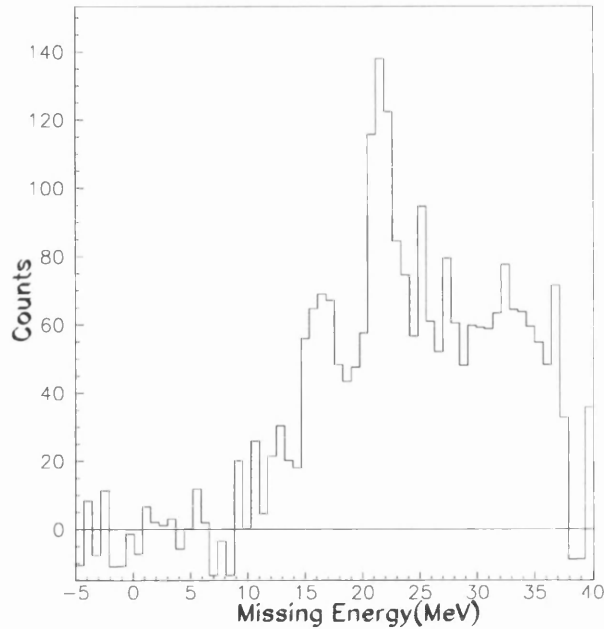


Figure 3.12: *Missing energy spectrum after subtraction of random*

The larger peak at  $\sim 22$  MeV is from unresolved excited states (5.2-6.2 MeV).

### 3.5.1 Background Subtraction

As the neutron detectors also record neutrons produced in non-target material, as well as the target itself, a correction must be made for these background neutrons. Some run time was devoted to a measurement of this background, by using an empty target container instead of the full target. After the same analysis procedure had been applied to the empty-target run, the background neutron spectrum was normalized to the same number of incident photons as the target-in run and then subtracted. The background contribution to the missing energy spectrum is shown in Fig.3.13, where it can be seen that its contribution to the missing energy spectrum is negligible (shaded area).

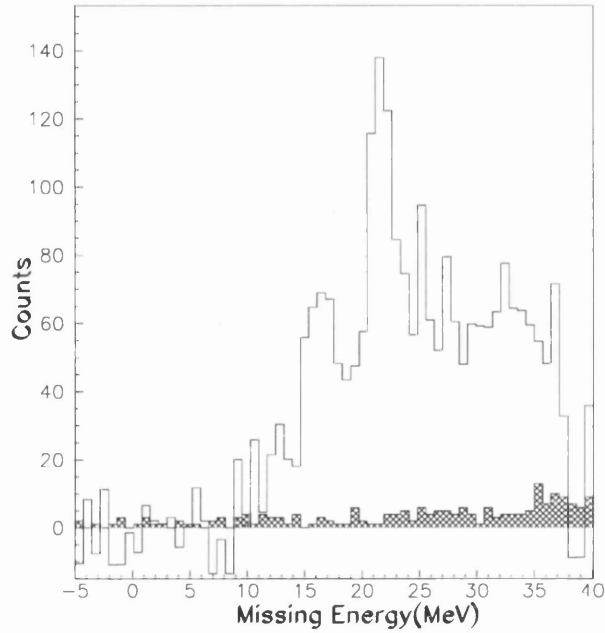


Figure 3.13: Contribution of background to the missing energy spectrum.

### 3.6 Absolute Cross-sections and Experimental Uncertainties

Several correction factors have to be considered for the calculation of the  $(\gamma, n)$  reaction differential cross-section. It is given by:

$$\frac{d\sigma}{d\Omega} = \frac{N_n}{N_\alpha \cdot N_e \cdot \Omega_n \cdot \epsilon_t \cdot \epsilon_l \cdot \epsilon_n \cdot \eta \cdot \epsilon_s} \quad (3.3)$$

where:

$N_n$ : Neutron yield in the missing energy peak

$\epsilon_s$ : Stolen coincidence correction

$N_\alpha$ : Number of target nuclei per unit area [ $cm^{-2}$ ]

$N_e$ : Number of electrons in the focal plane

$\Omega_n$ : Solid Angle

$\varepsilon_t$ : Tagging efficiency

$\varepsilon_l$ : Live time efficiency

$\varepsilon_n$ : Neutron detection efficiency

$\eta$ : Neutron transmission factor (through target)

These variables are discussed in the following

### Neutron Yield:

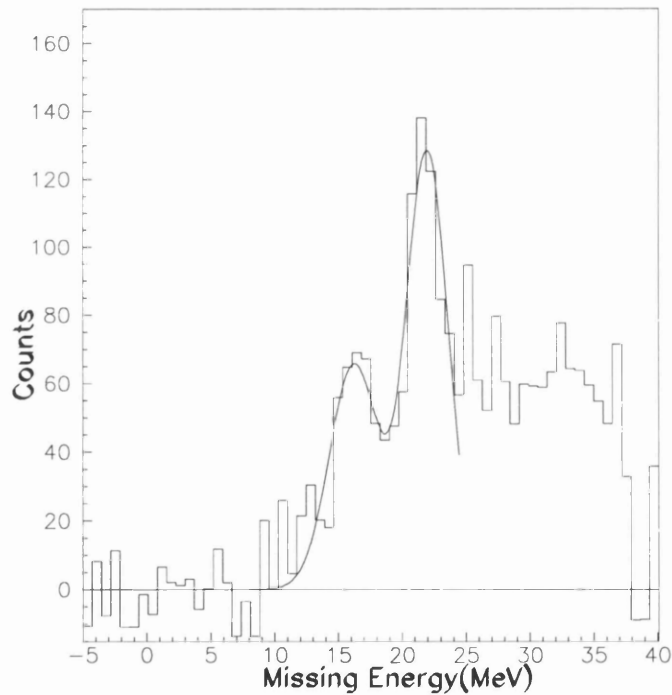


Figure 3.14: A missing energy spectrum of the  $^{16}\text{O}(\gamma,n)$  reaction with a gaussian fit of the ground and unresolved 5.2-6.2 MeV states.

The number of neutrons was obtained by integrating missing energy (or TOF). Peaks in missing energy were integrated by fitting one or more Gaus-

sians to the region of interest using PAW[72] (see Fig.3.14). The area of the Gaussian was obtained from the fit parameters:

$$N_n = k \times \sigma \times \sqrt{2\pi} \quad (3.4)$$

where  $k$  is the maximum value and  $\sigma$  is the width of the peak. The uncertainty in the fitting process is obtained from contributions of  $k$  and  $\sigma$  to  $N_n$ .

$$\left(\frac{\Delta N_n}{N_n}\right)^2 = \left(\frac{\Delta k}{k}\right)^2 + \left(\frac{\Delta \sigma}{\sigma}\right)^2 \quad (3.5)$$

The  $\Delta k$  and  $\Delta \sigma$  come from the error matrix calculated during the non-linear least-squares fitting procedure. The systematic uncertainty due to the fitting process is labelled sys. error(fit) in table 3.2.

As can be seen from Fig.3.11 the net neutron yield is dependent on the shape and normalization of the random spectrum. This will give rise to a systematic uncertainty. Estimation of this systematic uncertainty was done following the procedure described by Van Hoorebeke[46].

$E_m$ (MeV)	R	sys. error(rand. sub.) [%]	sys. error(fit) [%]	Total[%]
15.7	0.3365	1.7	0.35	1.73
21	0.5862	1.5	3.29	3.61

Table 3.2: *Systematic uncertainties due to the fit and random subtraction procedures for neutron yield.*

For each peak

$$N_n^{net} = N_n^{prompt} - N_n^{random} \quad (3.6)$$

$$\Delta N_n^{net} = \Delta N_n^{random} \quad (3.7)$$

$$R = \frac{N_n^{net}}{N_n^{random}} \quad (3.8)$$

then we can write for the relative error on  $N_n^{net}$

$$\frac{\Delta N_n^{net}}{N_n^{net}} = \frac{\Delta N_n^{random}}{N_n^{random}} \cdot \frac{1}{R} \quad (3.9)$$

$\Delta N_n^{random}$  was estimated by comparing two different normalization factors obtained in two different missing energy regions outside of possible  $(\gamma, n)$  kinematics. These were the regions of  $E_m < Q$  and  $E_m >$  neutron detection threshold (4.4 MeV<sub>ee</sub> threshold corresponds  $\sim 51$  MeV missing energy). These two regions gave similar results for the normalization factor ( $\Delta N_n^{random}$ ) to within 2.3% differences. In table 3.2 the systematic errors due to the random subtraction process and R are tabulated for different regions of missing energy (Fig.3.14).

### Stolen Coincidence( $\epsilon_s$ ):

When a random electron arrives at the FPD before a correlated electron, this random hit makes the system dead for a given time and thus the coincidence is lost. This effect is called stolen coincidence. The stolen coincidence correction for each FPD channel is given by [70]:

$$\epsilon_s = \exp\left(\frac{-dN_e}{dt} \times T_c\right) \quad (3.10)$$

where  $\frac{dN_e}{dt}$  is the instantaneous count rate in the FPD channel and  $T_c$  is the TDC start-stop time difference. The instantaneous FPD count rate, which is the average counting rate during the period in the 50 Hz accelerator cycle when the

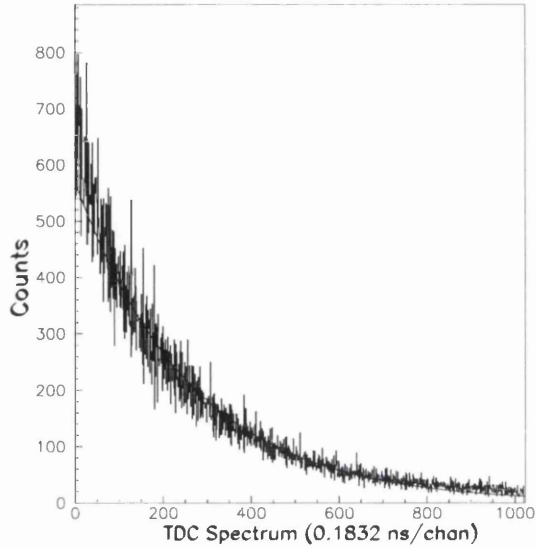
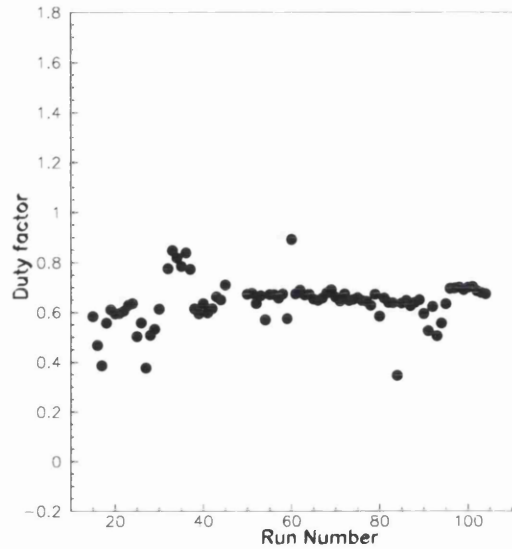


Figure 3.15: *Random TOF Spectrum.*

beam is active, was estimated [83] from the time-of-flight spectra on a run-by-run basis. The random coincidences in the TOF spectra have the form  $e^{-\frac{dN_e}{dt} \cdot t}$  [70] with  $t$  being the time. The value of  $\frac{dN_e}{dt}$  can be obtained by fitting an exponential to the TOF spectra. In order to reduce errors in the fitting procedure all FPD TOF spectra were combined. Although at normal photon tagging rates an average of 4 FPD produce a stop signal (see Fig.3.10) within the coincidence resolving time (multiplicity 4), the data were sorted so that only the earliest coincidence with a FPD was recorded. As shown in Fig.3.15 this procedure produces a random spectrum for each run which is well fitted by an exponential yielding  $\frac{dN_e}{dt}$ .  $\frac{dN_e}{dt}$  was calculated for each run and the mean value for all runs was used. The different analysis procedures produce the differences between the two random spectra shown in Fig.3.15 and Fig.3.10(shaded). The duty factor of the beam may be obtained by comparing the average and instantaneous FPD rates where the average rates are obtained from the FPD scalers, and this is plotted

Figure 3.16: *Duty factor of the electron beam.*

on a run-by-run basis in Fig.3.16. Errors on the duty factor  $\Delta d_f$  were obtained

$E_m$ [MeV]	$T_c$ [ns]	$\frac{dN_e}{dt}$ (per channel)	$\epsilon_s$
15.7	$98.231 \pm 0.643$	$3.203 \cdot 10^5 \pm 1.9 \cdot 10^4$	$0.969 \pm 0.0018$ (0.19%)
21	$93.212 \pm 0.61$	$3.203 \cdot 10^5 \pm 1.9 \cdot 10^4$	$0.9705 \pm 0.0017$ (0.18%)

Table 3.3: *Stolen Coincidence parameters.*

from the standard deviation of the duty factor for individual runs. The average duty factor of the beam was  $0.46 \pm 0.01$  for  $^2\text{H}$  runs,  $0.62 \pm 0.03$  for  $^{16}\text{O}$  runs and  $0.67 \pm 0.04$  for  $^6\text{Li}$  runs. The uncertainty on the stolen coincidence correction was calculated from equation 3.11,

$$\left(\frac{\Delta\epsilon_s}{\epsilon_s}\right)^2 = \left(\frac{dN_e}{dt} \times \Delta T_c\right)^2 + \left(T_c \times \Delta \frac{dN_e}{dt}\right)^2 \quad (3.11)$$

where  $\Delta T_c$  is the start-stop error which depends on the TDC calibration gain

$(0.1832 \pm 0.0012)$  and  $\Delta(\frac{dN_e}{dt})$  is the uncertainty in the instantaneous FPD rates, obtained from a combination of the standard deviation of the individual-run values and the errors of the fit procedure of Fig.3.15.

In table 3.3 the parameters and their uncertainties used to determine  $\epsilon_s$  are listed.

### Number of Atoms in Target( $N_\alpha$ ):

The number of atoms( $N_\alpha$ ) in a target is given by

$$N_\alpha = \frac{t \cdot \rho}{A} \times N_{avo} \quad (3.12)$$

where  $t$  is the thickness,  $\rho$  is the density,  $A$  is the mass number of the target nuclei and  $N_{avo}$  is the Avogadro number ( $6.02 \times 10^{23}$ ). The uncertainty in the number of target nuclei is due to the errors in measuring the dimensions and weights of targets. Details of the targets are shown in table 3.4.

Target	Density[ $\rho$ ]	Thickness[t]	Diameter[d]	Mass	$N_\alpha[10^{23}]$
	$g/cm^3$	cm	cm	A	$cm^{-2}$
Li	0.534	$5 \pm 0.1$	$4 \pm 0.1$	6.941	$2.315 \pm 2 \%$
$H_2O$	0.999	$9 \pm 0.1$	$6.7 \pm 0.1$	18.011	$3.005 \pm 1.1 \%$
$D_2O$	1.105	$9 \pm 0.1$	$6.7 \pm 0.1$	20.023	$2.99 \pm 1.1 \%$

Table 3.4: Target parameters

### Number of Electrons in the Focal Plane( $N_e$ ):

The number of recoil electrons in each FPD was counted with scalers. Since the scalers were read but not cleared the numbers were obtained from differences

between two successive readouts. However the number of electrons recorded in each FPD is less than the actual number due to dead time in the FPD electronics. This is estimated to be  $25 \pm 5$  ns and count rate is  $3 \times 10^5$  per FPD channel which gives  $\sim 0.75\%$  error on the number of electrons in FPD. Fig.3.17 shows total electron counts in each focal plane channel for a particular run in the measurement.

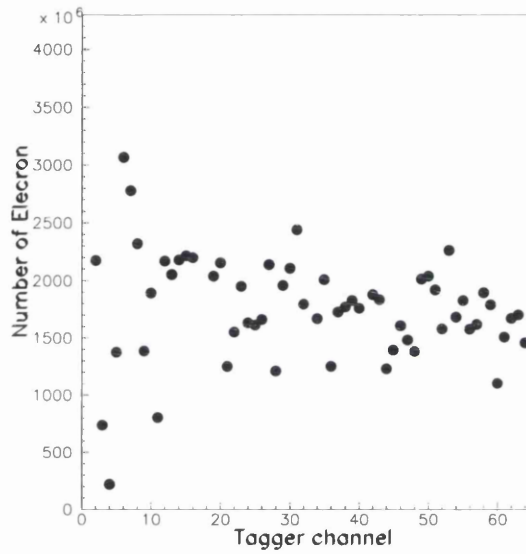


Figure 3.17: FPD total counts for a particular run.

### Solid Angle( $\Omega_n$ ):

The point source detector solid angle is approximated by:

$$\Omega_n = \frac{Area}{d^2} \quad (3.13)$$

where  $d$  is the distance from the target to the front face of the detector (flight path), and Area is the area of the front face ( $60\text{cm} \times 60\text{cm}$  square) of the neutron detector. This formula is valid when the flight path is much longer than

Array	d[m]	$\Omega$ [msr]
A	$2.550 \pm 0.005$	$55.3 \pm 1.7 \% \pm 2.5 \%$
B	$2.525 \pm 0.005$	$43.85 \pm 1.7 \% \pm 2.5 \%$

Table 3.5: *Solid Angle 9 cells for A, 7 cells for B array*

the detector size. A monte carlo simulation of a similar geometry [5] gave solid angles different from equation 3.13 by 2.5% which was taken as the error due to using the simple formula. In table 3.4 the flight path and related solid angle are tabulated. The additional 1.7 % systematic uncertainties are due to the flight path uncertainties.

#### Neutron Detection Efficiency( $\epsilon_n$ ):

As already mentioned in section(2.4.6) the neutron detection efficiency was calculated using the Monte-Carlo code STANTON [23] . This was performed for each neutron cell individually and the average value of all cells was then used in the cross section calculations. This was because of slightly different neutron incident angles, and detection thresholds for each cell. The calculation of the neutron detection efficiency is outlined in section 2.4.6 and is shown in Fig.2.19 for various detector thresholds. However for high energy  $n + {}^{12}\text{C}$  reactions the cross-sections are not so well known and some channels such as  ${}^{12}\text{C}(n,d)$  are not included in the code. To investigate these effects comparisons were made[5] with two other codes [30, 29] which include the  ${}^{12}\text{C}(n,d)$  reaction channel. Based on this the systematic uncertainty in the detection efficiency was estimated as 10%.

Live Time Efficiency( $\epsilon_l$ ):

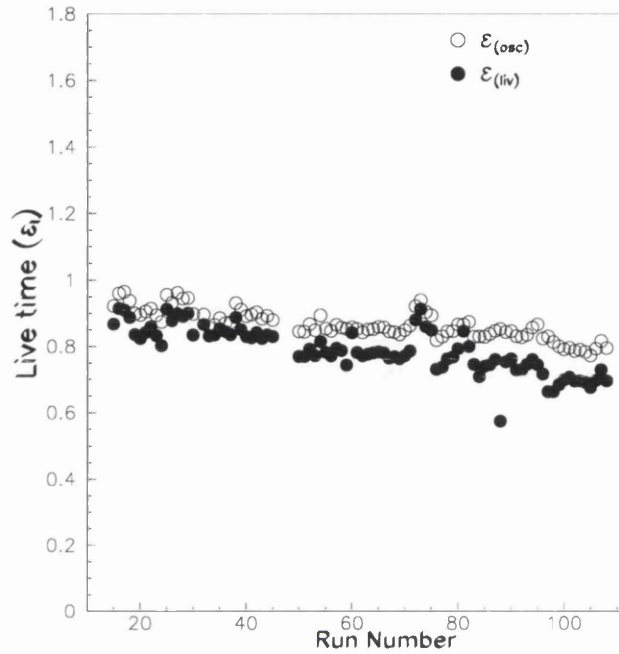


Figure 3.18: *Live time efficiency of the data acquisition system*

Since the electron scalers were not inhibited during the time of activation of the data acquisition system, when neutron triggers were inhibited, the live time efficiency of the electronics must be corrected in order to normalize the cross-section. In principle live time measurement can be made using an oscillator inhibited by the system busy signal.

$$\epsilon_{(osc)} = \frac{\text{Inhibited Clock}}{\text{Free Running Clock}} \quad (3.14)$$

However as the duty factor of the beam is not 100 % ,  $\epsilon_{(osc)}$  is greater than the actual live time efficiency and the effect of duty factor must be included.

Therefore live time efficiency was calculated via  $\varepsilon_{(osc)}$  using the formula of :

$$\varepsilon_{(liv)} = \frac{1}{d_f} \cdot [\varepsilon_{(osc)} - 1] + 1 \quad (3.15)$$

where  $d_f$  is the duty factor of the beam. It is clear that if the duty factor of the beam is 100% then  $\varepsilon_{(liv)}$  will be equal to the  $\varepsilon_{(osc)}$ . Live time efficiency as a function of each run in the experiment is shown in Fig.(3.18) for both  $\varepsilon_{(osc)}$  and  $\varepsilon_{(liv)}$ . The systematic uncertainty in  $\varepsilon_{(liv)}$  is due to the uncertainty in duty factor of the beam  $\Delta d_f$ . The uncertainty of the duty factor  $\Delta d_f$  was detailed before (see stolen coincidence subsection) and produces a percentage uncertainty in the live time of 1.7% for the  $^{16}\text{O}(\gamma,n)$  run.

### Tagging efficiency( $\varepsilon_t$ ):

The tagging efficiency, as discussed in section(2.3.3), depends on the pulse-height spectrum from the "spaghetti" detector. As shown in Fig.2.7 the separation of  $N_u$  and  $N_\gamma$  in equation 2.2 causes uncertainty in the calculation of the tagging efficiency. This was estimated as 3% for this measurement. To investigate the long term stability of tagging efficiency, a low-efficiency beam monitor was used to continuously investigate fluctuations in the ratio of monitor to FPD rate (see section 2.3.4). Fluctuation in this ratio was  $\leq 2\%$  which combined with the tagging efficiency uncertainty gave a total tagging efficiency error of 3.6%.

### Neutron Transmission Efficiency( $\eta$ ):

A small part of the neutron flux will not reach the detector due to attenuation in the target, air and the aluminium tank of the neutron detector. The transmission efficiency was determined in order to correct for this loss of neutrons.

The transmission efficiency  $\eta_i$  in material i (i= target,air,tank) is given by:

$$\eta_i = \exp(-\rho_i \sigma_i t_i) \quad (3.16)$$

where  $\rho_i$  is the number of target atoms per unit volume,  $\sigma_i$  is the attenuation cross-section, and  $t_i$  is the thickness of the material through which neutrons travel. The total attenuation then is obtained from the contribution of each material:

$$\eta_{total} = \prod_i \eta_i \quad (3.17)$$

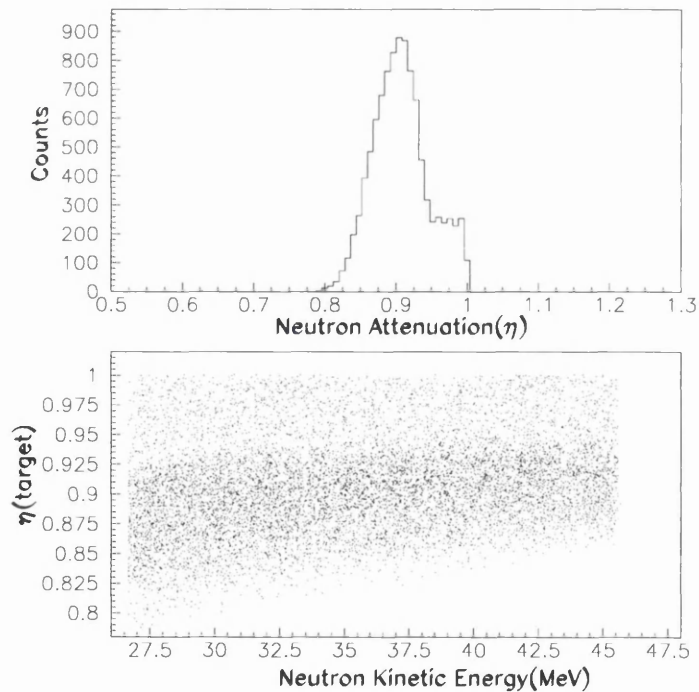


Figure 3.19: *Neutron Transmission efficiency for the measurement of the  $^{16}\text{O}(\gamma, n_{123})$  reaction.*

The total cross-section for a neutron induced reaction is described by

$$\sigma_{tot} = \sigma_{elastic} + \sigma_{reaction} \quad (3.18)$$

where the reaction cross-section includes all non-elastic processes. In previous tagged photon measurements [44, 33], it was assumed that  $\sigma_i = \sigma_{reaction}$  as it was argued that elastic scattering of neutrons into the detection solid angle is equal to the elastic scattering of neutrons out of the detection solid angle, which is consistent with an earlier observation of Drogg[32]. The transmission efficiency derived from  $\sigma_i = \sigma_{reaction}$  is  $\sim 5\%$  higher than obtained with  $\sigma_i = \sigma_{total}$ . From this result an uncertainty in  $\eta$  of 5% was used in the cross-section calculation. A monte carlo code[12] was used to obtain transmission efficiencies taking account of the variations in  $t_i$  caused by large-sized detectors and target, and the energy dependence of  $\sigma_i$ . In Fig.3.19(upper) the transmission efficiency for events which populate the  $\sim 6$  MeV states of  $^{15}\text{O}$  ( $\text{H}_2\text{O}$  target), for a 45 degree neutron detection angle, is shown. Mean values produced by this procedure were used to correct the cross-sections. In the lower plot transmission efficiency versus neutron kinetic energy is plotted.

### Total Systematic Uncertainties:

When the above uncertainties are added in quadrature the total is obtained

$$\begin{aligned} \left(\frac{\Delta(\frac{d\sigma}{d\Omega})}{\frac{d\sigma}{d\Omega}}\right)^2 &= \left(\frac{\Delta N_n}{N_n}\right)^2 + \left(\frac{\Delta N_\alpha}{N_\alpha}\right)^2 + \left(\frac{\Delta N_e}{N_e}\right)^2 + \left(\frac{\Delta \Omega_n}{\Omega_n}\right)^2 + \\ &\quad \left(\frac{\Delta \epsilon_t}{\epsilon_t}\right)^2 + \left(\frac{\Delta \epsilon_n}{\epsilon_n}\right)^2 + \left(\frac{\Delta \epsilon_l}{\epsilon_l}\right)^2 + \left(\frac{\Delta \eta}{\eta}\right)^2 + \left(\frac{\Delta \epsilon_s}{\epsilon_s}\right)^2 \end{aligned}$$

The systematic uncertainties associated with each parameter for the measurement of  $^{16}\text{O}(\gamma, n)$  are given in table(3.6).

As can be seen from table 3.6 the most important source of systematic error is the neutron detection efficiency. As already discussed, the calculation of

$E_m$ (MeV)	$\frac{\Delta N_n}{N_n}$	$\frac{\Delta N_\alpha}{N_\alpha}$	$\frac{\Delta N_e}{N_e}$	$\frac{\Delta \Omega_n}{\Omega_n}$	$\frac{\Delta \epsilon_t}{\epsilon_t}$	$\frac{\Delta \epsilon_n}{\epsilon_n}$	$\frac{\Delta \epsilon_l}{\epsilon_l}$	$\frac{\Delta \eta}{\eta}$	$\frac{\Delta \epsilon_s}{\epsilon_s}$	Total
15.7	1.7	1.1	0.75	3.0	3.6	10	1.7	5	0.19	12.4
21	3.6	1.1	0.75	3.0	3.6	10	1.7	5	0.18	12.8

Table 3.6: *Cross-section uncertainty parameters*

neutron detection efficiency by STANTON does not include all possible neutron interactions and thus the uncertainty is relatively large.

### 3.7 Measurement of Decay-gamma rays

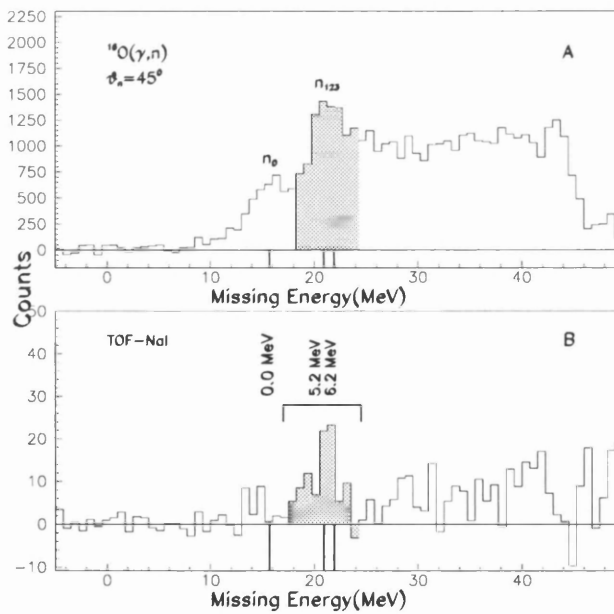


Figure 3.20: A: *Missing Energy spectrum of  $^{16}\text{O}(\gamma, n)^{15}\text{O}$  using  $E_\gamma = 50\text{--}70$  MeV tagged photons, B: Equivalent missing energy plot, but with a TOF-NaI coincidence.*

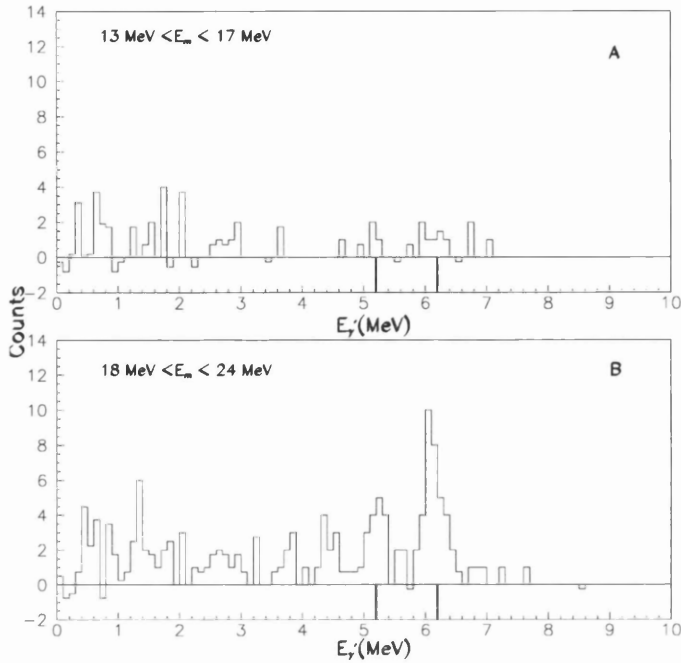


Figure 3.21: Decay Photon Energy ( $E_\gamma$ ) spectra at  $45^\circ$  neutron detection angle for two different missing energy regions in  $^{15}\text{O}$  (ground state in A, unresolved 5.2-6.2 MeV states in B).

In this section the data analysis procedure for the decay- $\gamma$ -ray measurement will be presented. As identification of decay- $\gamma$ -rays requires a triple coincidence (Tagger-TOF-NaI) a further step has to be applied in the analysis. The first step of the analysis is to identify the interesting region in missing energy (Fig.3.20A). When a coincidence with the NaI (see section 2.5.2) is further applied this gives the missing energy spectrum Fig.3.20B which suggests that the decay-photons are mainly from the 5.2-6.2 MeV states of  $^{15}\text{O}$ . As expected the extra NaI coincidence suppresses the ground state region of missing energy. Decay- $\gamma$  correlations were also checked by making cuts on regions of missing energy (Fig.3.20) and then examining the NaI pulse height spectrum. Fig.3.21A results if missing energy is

cut around the  $^{15}\text{O}$  ground state region. Fig.3.21B results if missing energy is cut around the region containing the 5.2 and 6.2 MeV states.

Cross-sections for the resolved 5.2 MeV ( $n_{12}$ ) and 6.2 MeV ( $n_3$ ) states were not calculated absolutely from the triple-coincidence data (Fig.3.21B). Firstly the cross-section for  $(\gamma, n_{123})$  which contains unresolved  $n_{12}$  and  $n_3$ , was obtained from double-coincidence  $(\gamma, n)$  data using the method described in the previous section. Secondly the strength ratio between the  $n_{12}$  and  $n_3$  states was obtained using the decay-gamma-ray photon energy spectra. Knowing the cross-section of  $n_{123}$  ( $n_{12}+n_3$ ) and the ratio  $(\frac{n_{12}}{n_3})$ , the cross-sections for the individual states were obtained. As the states are well separated the systematic error of the ratio is negligible compared to the systematic error of the  $(\gamma, n_{123})$  cross section.

## **Chapter 4**

# **Results and Discussion**

## 4.1 Introduction

In this chapter results from  $(\gamma, n)$  and  $(\gamma, n\gamma')$  measurements are presented. Measured missing energy spectra, de-excitation  $\gamma$ -ray spectra (for  $^{16}\text{O}(\gamma, n\gamma')$ ) and differential cross sections, as a function of photon energy and neutron detection angle, are presented and comparisons are made with previous  $(\gamma, N)$  measurements and also with the predictions of various models. The  $^{16}\text{O}(\gamma, n\gamma')$  measurement is the first in which decay gammas from the residual nucleus after  $(\gamma, n)$  have been detected. The  $^6\text{Li}(\gamma, n)$  results are the first tagged photoneutron data in the intermediate energy region.

## 4.2 A Test Based on the $^2\text{H}(\gamma, n)$ Reaction

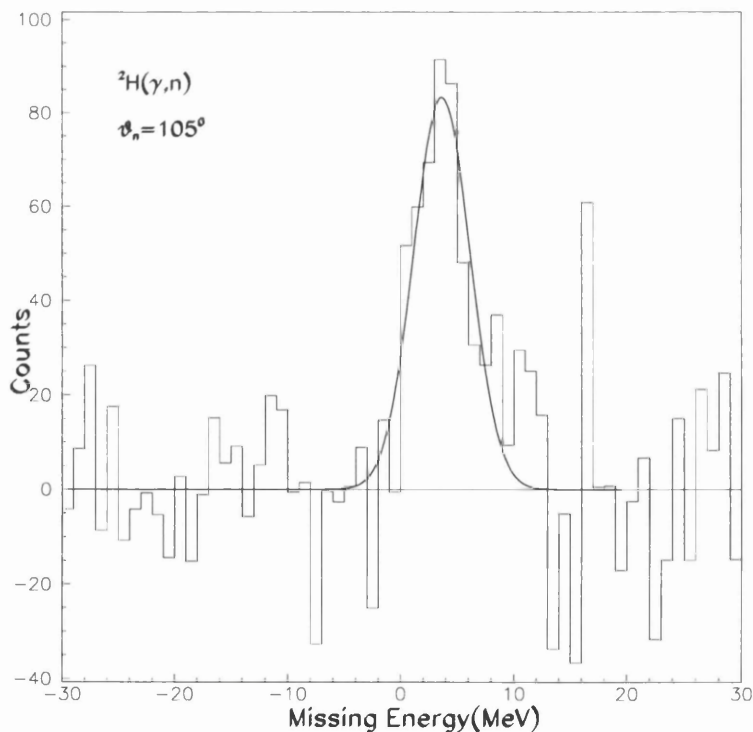


Figure 4.1: Missing Energy for  $^2\text{H}(\gamma, n)$  reaction using  $\sim 60$  MeV tagged photons.

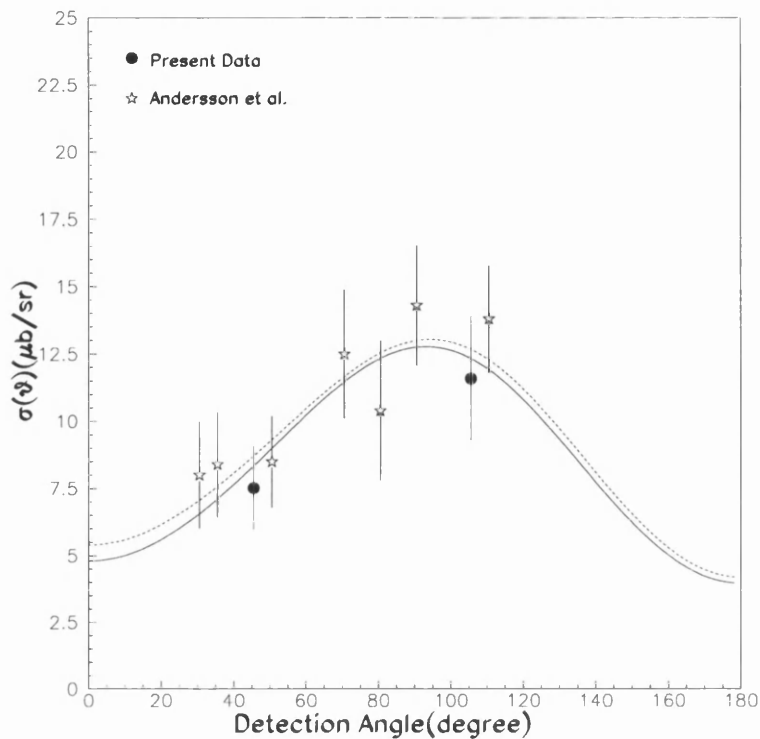


Figure 4.2: Cross-section for the  ${}^2\text{H}(\gamma, n)$  reaction and comparison with previous data obtained by Andersson et al.[5] and with the curves produced by the parametrisations of Jenkins et al.[48] (solid line) and Rossi et al.[73] (dotted line)(The error bars shows the combination of statistical and systematic uncertainties for both data points).

In photonuclear reactions the well-known two-body photodisintegration cross section of deuterium may be used in order to provide an overall check of cross section normalization. Therefore some of the run time was used for the measurement of  ${}^2\text{H}(\gamma, n)$  at the same energies and laboratory angles as  ${}^{16}\text{O}$  and  ${}^6\text{Li}$ . For this purpose measurements were made using a  $\text{D}_2\text{O}$  target. Spectra of missing energy were generated for  $\text{D}_2\text{O}$  and  $\text{H}_2\text{O}$  target runs, assuming  ${}^2\text{H}(\gamma, n)$  reaction kinematics and the  $\text{H}_2\text{O}$  spectrum was subtracted from the  $\text{D}_2\text{O}$  spectrum to give a spectrum due to deuterium. The resulting missing energy spectrum (Fig.4.1)

shows a clear peak at the expected value of 2.2 MeV which is the deuteron binding energy. In Fig.4.2 the measured differential cross section is compared with similar  ${}^2\text{H}(\gamma, n)$  data due to Andersson et al. [5]. The data are also compared with calculations made from parametrizations of all available data, which were compiled by Jenkins et al.[48] and Rossi et al.[73]. These parametrizations represent the "state of the art" regarding current knowledge of the two-body deuteron photodisintegration cross section. The consistency of the present data with previous measurements and with the parametrisation is very good, lending confidence that the absolute cross section evaluation is correct.

### 4.3 ${}^{16}\text{O}(\gamma, n\gamma')$ Reaction

Single arm  ${}^{16}\text{O}(\gamma, n){}^{15}\text{O}$  reaction cross sections were first extracted in order to compare with previous measurements. The threshold of the  ${}^{16}\text{O}(\gamma, n)$  reaction is 15.7 MeV and the  ${}^{15}\text{O}$  energy level scheme is listed in table 4.1. The missing energy spectrum for  ${}^{16}\text{O}(\gamma, n)$  with 50-70 MeV tagged photons is displayed in Fig.4.3. The ground state ( $\frac{1}{2}^-$ ) peak is observed at 15.7 MeV and is resolved from other peaks. For the present measurement, neutron kinetic energies of  $\sim 30$ -50 MeV and a flight path of  $\sim 2.5$  m resulted in  $\sim 3$  MeV missing energy resolution (see section 2.4.4). This is not good enough to separate 5.2 MeV doublet, 6.2 MeV and higher excitations which are included within the shaded area in Fig.4.3. The rest of the spectrum is due either to unresolved higher excitations of  ${}^{15}\text{O}$  or to other reaction channels where more particles are emitted.

As mentioned earlier, decay  $\gamma$ -rays from the 5.2 and 6.2 MeV excitations were measured in order to resolve these states (see section 2.5). Fig.4.4 shows the decay-photon energy spectra obtained after selecting events in the shaded

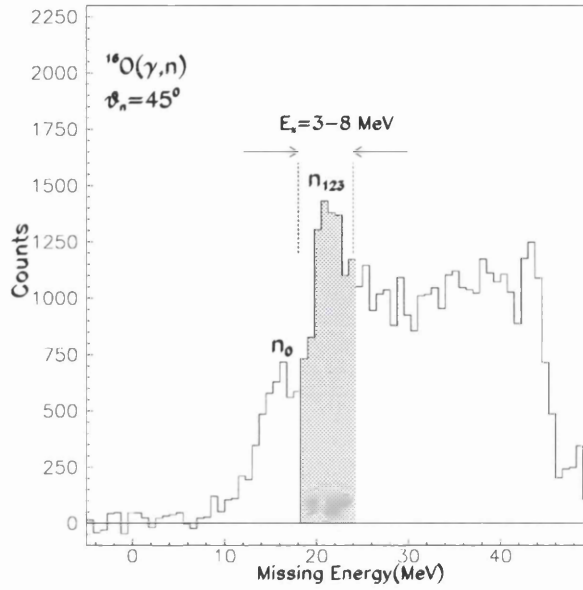


Figure 4.3: Missing Energy Spectrum for the  $^{16}\text{O}(\gamma, n)$  reaction obtained at  $45^\circ$  neutron detection angle, using 50-70 MeV tagged photons. The shaded area contains unresolved states at 5.2, 6.2 MeV and possibly higher excitations.

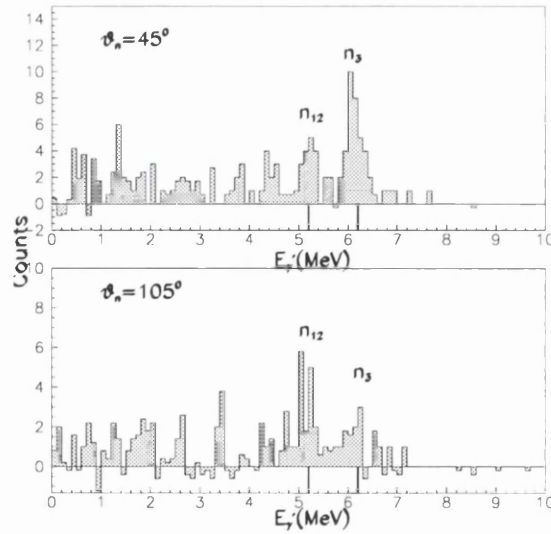


Figure 4.4: De-excitation  $\gamma$ -ray spectrum obtained in  $^{16}\text{O}(\gamma, n\gamma')$ , triggered by  $E_\gamma=50-70$  MeV tagged photons and  $E_x=3-8$  MeV of excitation energy (shaded area Fig.4.3).

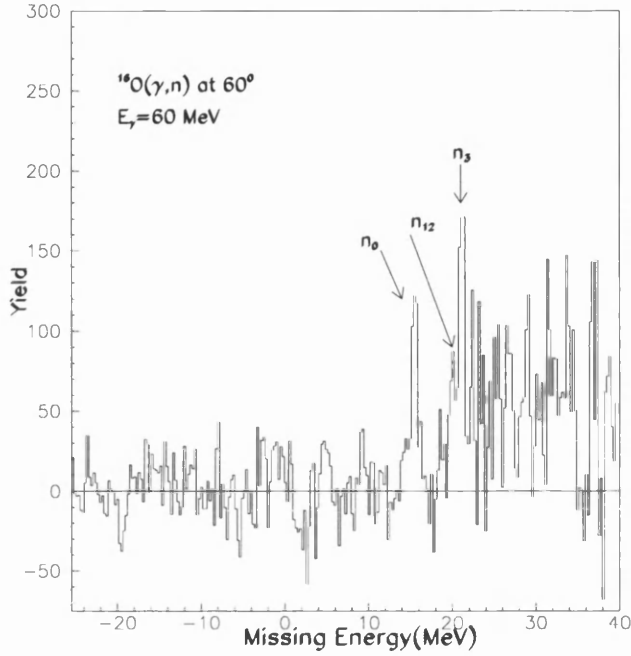


Figure 4.5: *High resolution missing energy spectrum for  $^{16}\text{O}(\gamma, n)$  reaction taken at Max-Lab[5].*

area of the missing energy spectrum of Fig.4.3. Note that the NaI resolution is not good enough to resolve the 5.2 MeV doublet. It is clear from Fig.4.4 that the relative strengths of the  $\gamma'$  peaks vary with the detection angle of the neutron. A  $\gamma$ -ray energy resolution of  $\sim 300$  keV (FWHM) was obtained (Fig.4.4) which is a factor  $\sim 10$  better than from a direct  $(\gamma, n)$  measurement with a 2.5 metre flight path. The best obtainable  $(\gamma, n)$  resolution at Max-Lab is 1 MeV using a 6 meter flight path, which is the maximum available in the reaction cave. A measurement[6] performed using this flight path at  $60^\circ$ , for photons of average energy 60 MeV is shown in Fig.4.5. In this spectrum the  $n_{12}$  and  $n_3$  states are barely resolved. Comparison with Fig.4.4 shows the improvement obtained in resolution from the decay  $\gamma$ -ray technique. Although the  $(\gamma, n)$  counting rate

$E_x$ [MeV]	$E_m$ [MeV]	$J^\pi$	T	Character
$n_0$ (gs)	15.7	$\frac{1}{2}^-$	$\frac{1}{2}$	1h
$n_1$ (5.18)	20.88	$\frac{1}{2}^+$	$\frac{1}{2}$	2h-1p
$n_2$ (5.24)	20.94	$\frac{5}{2}^+$	$\frac{1}{2}$	2h-1p
$n_3$ (6.2)	21.9	$\frac{3}{2}^-$	$\frac{1}{2}$	1h

Table 4.1: *Energy Level scheme of  $^{15}\text{O}$  for the first four states [3].*

(Fig.4.5) was greater than  $(\gamma, n\gamma')$  (Fig.4.4) the latter had a relatively small background subtraction. The big improvement in resolution obviously makes separation of the 5.2 and 6.2 MeV states easier and more reliable.

### 4.3.1 Cross sections and Comparison with $(\gamma, \text{N})$ Measurements

Differential cross sections were measured at an average photon energy of 60 MeV and at  $45^\circ$  and  $105^\circ$  neutron detection angles.  $^{16}\text{O}(\gamma, n)$  cross sections were obtained for  $(\gamma, n_0)$  and  $(\gamma, n_{123})$  and are shown in Fig.4.6 where they are compared with previous measurements of  $(\gamma, n)$  cross sections summarized in section 1.6. The data are compared with those of Goringer et al.[40] (open square in Fig.4.6A), O'keefe et al.[69] (open circles) Andersson et al.[6] (open star) and Schoch et al.[78] (open square in Fig.4.6B). Reasonable agreement is found between the present and previous  $(\gamma, n)$  data. The error bars of the present and ref.[6] show the total uncertainty, while other data are statistical only.

The high resolution  $(\gamma, n\gamma')$  cross sections obtained from the present measurement are compared with the high resolution  $(\gamma, n)$  data of Andersson et al.

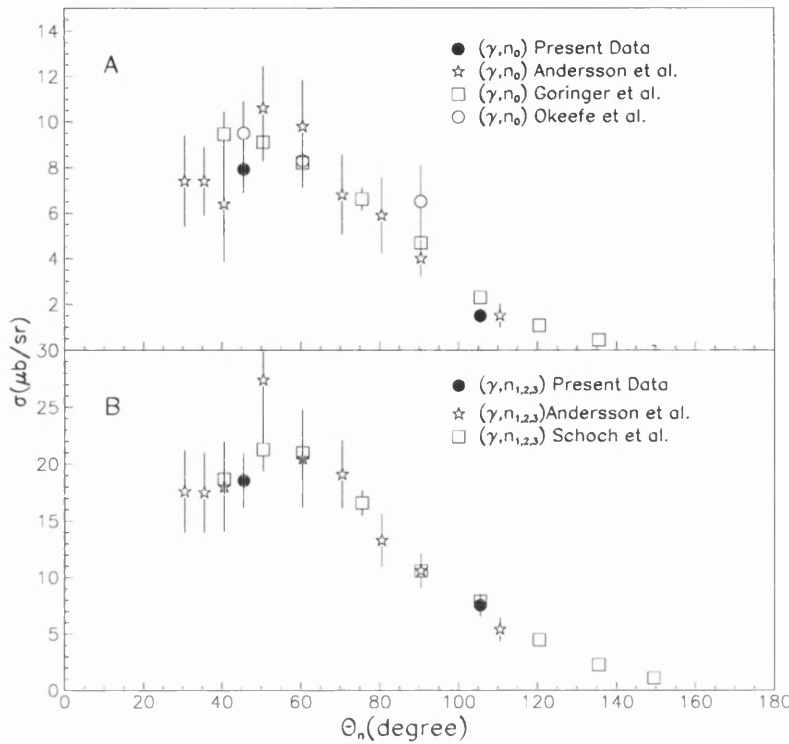


Figure 4.6: Cross-section of  $^{16}\text{O}(\gamma, n_0)$  and  $^{16}\text{O}(\gamma, n_{1,2,3})$  reaction and comparison with previous measurements [6, 40, 78, 69].

[6] and an equivalent high resolution ( $\sim 800$  keV)  $^{16}\text{O}(\gamma, p)$  measurement [67] which was also performed at Max-Lab. These high resolution  $(\gamma, N)$  data are shown in Fig.4.7 where only statistical error bars are included in the  $(\gamma, p)$  measurement. The similarity between  $(\gamma, n)$  and  $(\gamma, p)$  cross sections is evidence for the importance of photon absorption by correlated nucleons. However  $(\gamma, n_0)$  and  $(\gamma, n_3)$  seem to be systematically smaller than  $(\gamma, p_0)$  and  $(\gamma, p_3)$  at forward angles.  $(\gamma, n_{12})$  has a relatively weak angular dependence and seems to drop more slowly with increasing angle than the equivalent  $(\gamma, p_{12})$ .

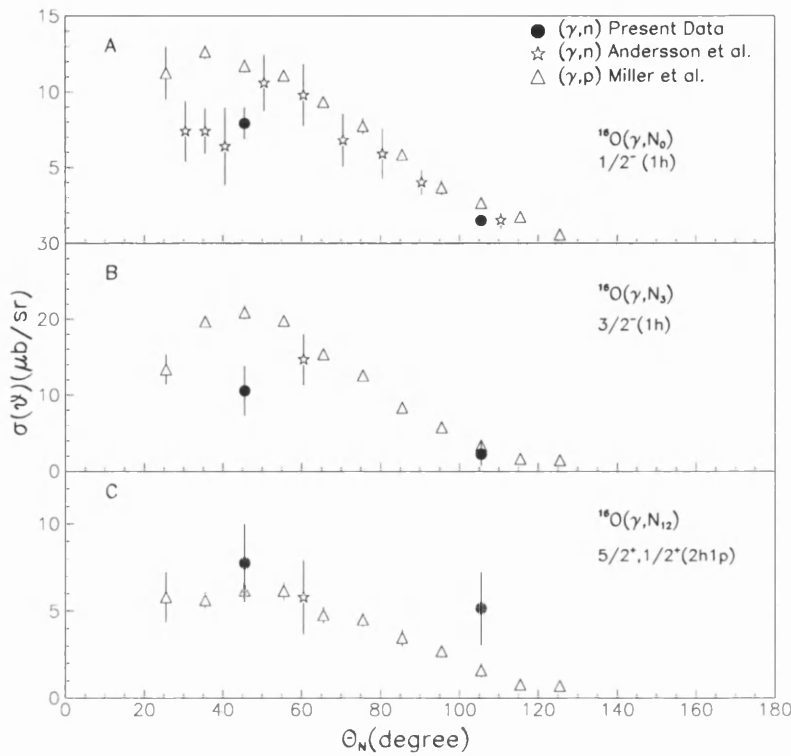


Figure 4.7: Cross-section of high resolution  $^{16}\text{O}(\gamma, n)$  and comparison with previous  $^{16}\text{O}(\gamma, N)$  data[6, 67] taken at Max-Lab.

### 4.3.2 Comparison with Theoretical Calculations

The measured cross sections are compared with the results of coupled-channels calculations which were performed within a continuum Hartree-Fock, Random Phase Approximation (HF-RPA) framework, by the Gent group[75]. In this model single-proton and neutron knockout from the  $1s_{\frac{1}{2}}$ ,  $1p_{\frac{3}{2}}$  and  $1p_{\frac{1}{2}}$  orbitals is considered. Consequently differential cross sections for the  $\frac{1}{2}^-$  (ground) and  $\frac{3}{2}^-$  ( 6.2 MeV) states, which are mainly 1h in character, were obtained. As the states were assumed to be purely 1h, the calculations have been multiplied by spectroscopic factors, extracted from an equivalent analysis of  $^{16}\text{O}(e, e'p)$  data

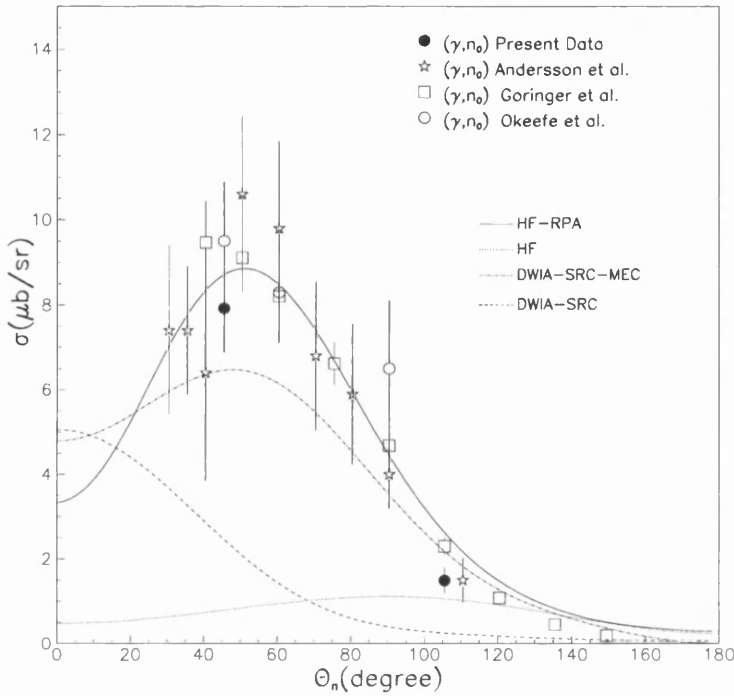


Figure 4.8: Cross-sections for  $^{16}\text{O}(\gamma, n_0)$  reaction and comparison with theoretical calculations (HF-RPA and HF are from Gent [75], DWIA-SRC and DWIA-SRC-MEC are from Pavia [14]).

which are a measure of the hole component strength. The nuclear current operator, obtained from minimal substitution in the Hamiltonian, has both one and two-body terms. Two-body terms result from momentum-dependent components of the Skyrme effective N-N interaction, which is used in the Hartree-Fock procedure to construct the initial nuclear wave function. Siegert's theorem is not used, as it might have given double counting of MEC effects. The theoretical predictions are compared with  $(\gamma, n)$  data in Fig.4.8 and both  $(\gamma, n)$  and  $(\gamma, p)$  (labelled collectively  $(\gamma, N)$ ) data in Fig.4.9. The full calculation is labelled HF-RPA in Fig.4.8 and Fig.4.9A,B where it can be seen that a consistent

theoretical treatment gives a good account of  $(\gamma, n)$  data (Fig.4.8) and  $(\gamma, N)$  data (Fig.4.9A,B). A similar calculation which neglected the effects of channel couplings and final state rescattering (no RPA) was made using the same Skyrme interactions (labeled HF in Fig.4.8 and Fig.4.9A,B) and thus should include the effects of two-body photoabsorption. As shown in Fig.4.8 and Fig.4.9A,B the HF  $(\gamma, n)$  calculation is far below the data while in Fig.4.9A,B,  $(\gamma, p)$  in which quasifree knockout is significant, is also below the data but in better agreement than  $(\gamma, n)$ . These calculations predict that two-body photoabsorption is clearly not a dominant effect especially in  $(\gamma, n)$  where quasi-free knockout is small.

Further calculations have been performed using an extension of the Pavia DWIA approach [14] to investigate the role of MEC effects for the  $(\gamma, n_0)$  reaction. The nuclear wave function is essentially derived from the shell model, but contains short-range-correlation terms of the Jastrow type (SRC). The current operator includes a two-body part, derived from the one-pion-exchange potential, where only the seagull term has been retained. An optical potential is used to model the  $n$ - $^{15}\text{O}$  FSI. This calculation which was made with one-body currents only (DWIA-SRC in Fig.4.8) and with two-body currents included (DWIA-SRC-MEC in Fig.4.8) predicts a dominant MEC effect. However the calculated cross section is very sensitive to FSI and needs much more care in the choice of optical potential before the calculation can be believed. The effects of changing the optical potential are at least as big as those of switching on/off the two-body current.

The cross section of the unresolved  $(\frac{5}{2}^+, \frac{1}{2}^+)$  doublet at  $\sim 5.2$  MeV can not be obtained with a coupled-channels HF-RPA calculation as the structure of the  $\frac{5}{2}^+$  and  $\frac{1}{2}^+$  states is not 1h. They are mainly 2h1p in character and can be excited in a direct reaction through photoabsorption on an exchanged charged pion. The

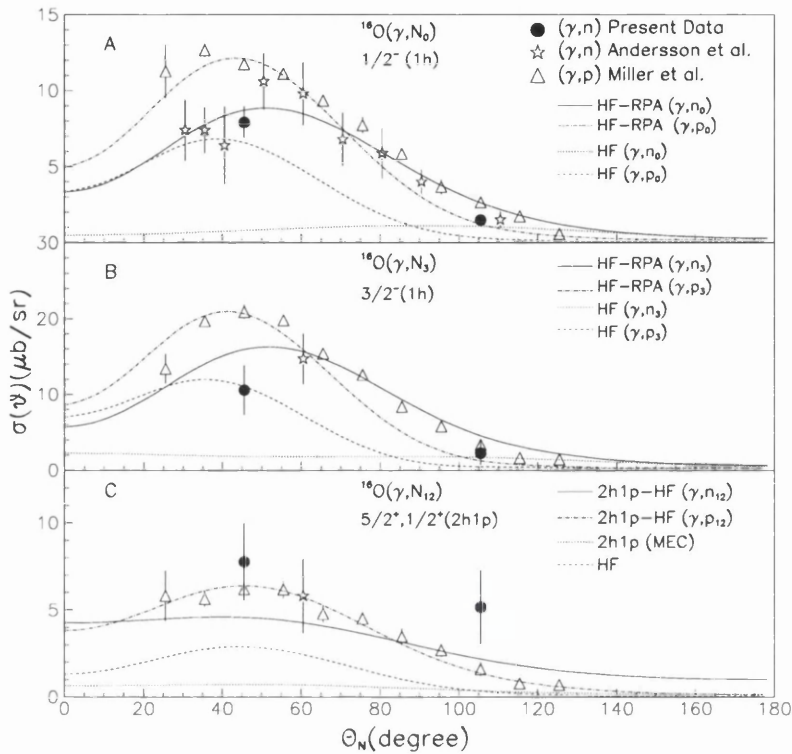


Figure 4.9: Cross-sections for  $^{16}\text{O}(\gamma, N)$  reactions and comparison with theoretical calculations.

cross section for this type of reaction has been calculated [76] using a model where only the dominant 2h1p component in the wave functions for the  $\frac{1}{2}^+$  and  $\frac{5}{2}^+$  states has been retained and one-pion-exchange currents are assumed to be fully responsible for the cross section. No FSI effects are included. The dominant 2h1p components are  $(1p_{1/2})^{-2} (1d_{5/2})$  for the  $\frac{5}{2}^+$  state and  $(1p_{1/2})^{-2} (2s_{1/2})$  for the  $\frac{1}{2}^+$  state. This model predicts  $\sigma_{\frac{1}{2}^+} \ll \sigma_{\frac{5}{2}^+}$  and after these cross sections are added (Fig.4.9C) they fall far below the experimental data. However a 2s1d-shell admixture to the  $^{16}\text{O}$  ground state, offers the possibility to reach these states via QFK of a nucleon or 2N absorption where one of the nucleons returns to its original orbital. The amplitudes and cross-sections for this reaction mechanism

were calculated using the HF formalism described above. Spectroscopic factors, obtained from an analysis of high resolution  $^{16}\text{O}(e,e'p)$  data [84] gave the strength for the  $(1d_{5/2})^{-1}$  and  $(2s_{1/2})^{-1}$  components of the  $\frac{5}{2}^+$ ,  $\frac{1}{2}^+$  states respectively. This calculation is labelled HF in Fig.4.9C where it can be seen that although it is closer than the MEC calculation to the experimental data, it still underestimates it. When the HF and MEC amplitudes are added coherently to produce the cross sections labelled 2h1p-HF in Fig.4.9C a better description of both  $(\gamma, n_{12})$  and  $(\gamma, p_{12})$  data is obtained.

#### 4.4 The $^6\text{Li}(\gamma, n)$ Reaction

$E_x$ (MeV)	$E_m$ (MeV)	$J^\pi$	T	$\Gamma_{cm}$ (MeV)
g.s	5.7	$(\frac{3}{2})^-$	$\frac{1}{2}$	1.5
5-10	10.7-15.7	$(\frac{1}{2})^-$	$\frac{1}{2}$	$5 \pm 2$
16.66	22.36	$(\frac{3}{2})^+$	$\frac{1}{2}$	$0.2 \pm 0.06$
18	23.7	$(\frac{1}{2})^+$	$\frac{1}{2}$	broad
20	25.7	$(\frac{3}{2}, \frac{5}{2})^+$	$\frac{1}{2}$	$\sim 5$
34	39.7			$\sim 4$

Table 4.2: *Excited states of  $^5\text{Li}$ [3]*

The  $^6\text{Li}(\gamma, n)$  measurement was performed using 50-70 MeV tagged photons and  $45^\circ$  and  $105^\circ$  neutron detection angles. The threshold for the  $^6\text{Li}(\gamma, n)$  reaction is 5.7 MeV and the reaction leaves  $^5\text{Li}$  as a residual nucleus, for which the level scheme is listed in table 4.2.

The  $^6\text{Li}(\gamma, n)$  missing energy spectra obtained with photons of average energy  $\sim 58$  MeV at  $45^\circ$  and  $105^\circ$  neutron detection angle are shown in Fig. 4.10. A

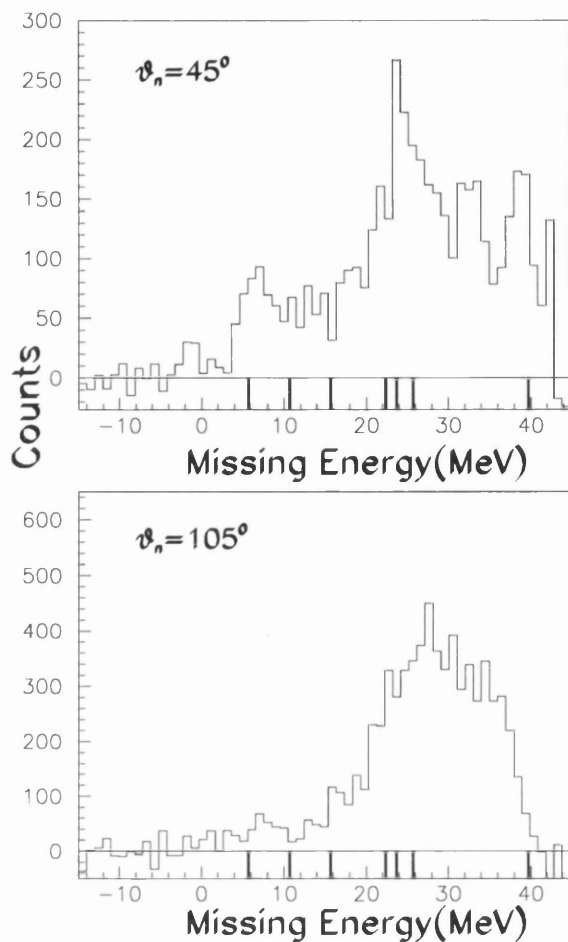


Figure 4.10: Missing energy for  $E_\gamma=50.7-64.2$  MeV of  ${}^6\text{Li}(\gamma, n)$ .

clear peak at 5.7 MeV missing energy, associated with knockout of a 1p-shell neutron to the  ${}^5\text{Li}(\frac{3}{2}^-)$ , ground state can be seen at  $45^\circ$  detection angle but is much less prominent at  $105^\circ$ . The peak is superimposed on a continuum, where other undetected particles are emitted in addition to the neutron, which increases in the 20 MeV missing energy region. This continuum can be partially attributed to  ${}^6\text{Li}(\gamma, n)p + {}^4\text{He}$  (threshold  $\sim 3.7$  MeV) where the photon interacts with the loosely bound outer p-n pair. Above 22 MeV missing energy the  ${}^6\text{Li}(\gamma, n){}^3\text{He} + d$  reaction, where the photon interacts with the  $\alpha$ -core, may also contribute to the

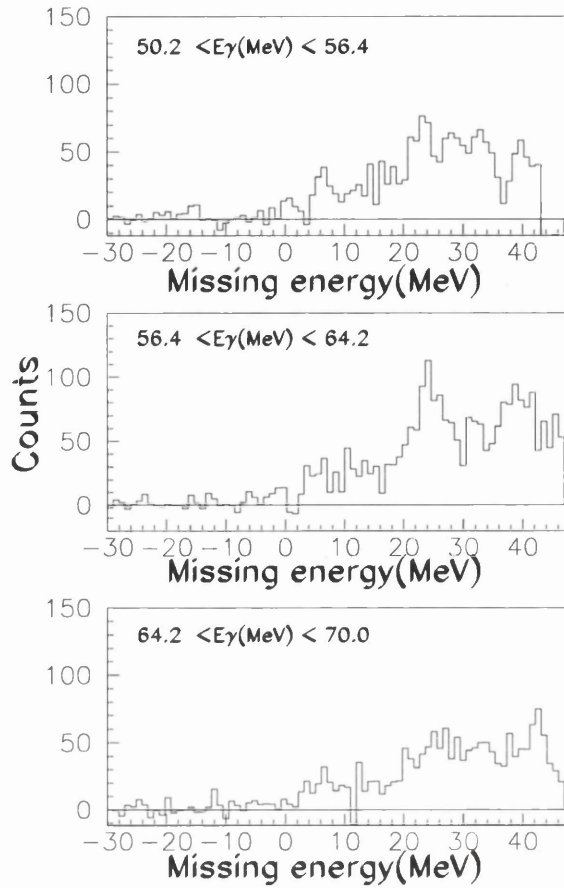


Figure 4.11: Missing energy for the  ${}^6\text{Li}(\gamma, n)$  reaction at  $45^\circ$  neutron detection angle and three different photon energy ranges.

broad continuum peak seen at  $\sim 25$  MeV missing energy. In Fig.4.11 and Fig.4.12 missing energy spectra are shown as a function of photon energy for the  $45^\circ$  and  $105^\circ$  neutron detection angles respectively. It can be seen from those figures that the ground-state peak becomes smaller for higher photon energies at  $45^\circ$ . The states in  ${}^5\text{Li}$  can be populated via other reactions such as  ${}^7\text{Li}({}^3\text{He}, dt){}^5\text{Li}$  and  ${}^6\text{Li}(p, d){}^5\text{Li}$ . The excitation energy spectrum of the  ${}^7\text{Li}({}^3\text{He}, dt){}^5\text{Li}$  reaction[38] shows a ground-state peak, a 4 MeV wide bump at 34 MeV and some weak indication of structure at 22 MeV (Fig.4.13). In the case of the  ${}^6\text{Li}(p, d){}^5\text{Li}$

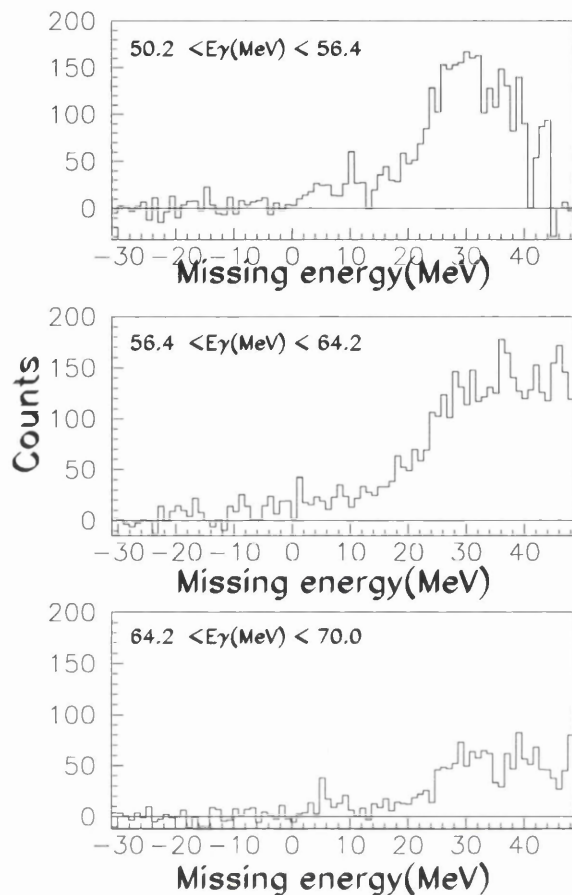


Figure 4.12: *Missing energy for the  ${}^6\text{Li}(\gamma, n)$  reaction at  $105^\circ$  neutron detection angle and three different photon energy ranges.*

reaction[13] the excitation energy spectrum shows similar features to the present  $(\gamma, n)$  missing energy spectrum, a peak at the ground state and a large bump around 20-30 MeV (Fig.4.14).

The equivalent  ${}^6\text{Li}(\gamma, p)$  missing energy spectrum where  ${}^5\text{He}$  is the residual system shows similar structure. Fig.4.15 shows the missing energy spectrum for  ${}^6\text{Li}(\gamma, p)$  [68](upper) and  ${}^6\text{Li}(\gamma, n)$  (lower). The  ${}^6\text{Li}(\gamma, p)$  missing energy spectrum was obtained using tagged photons of average energy 61 MeV and a  $90^\circ$  proton detection angle, while the  ${}^6\text{Li}(\gamma, n)$  measurement was taken at  $45^\circ$  neutron

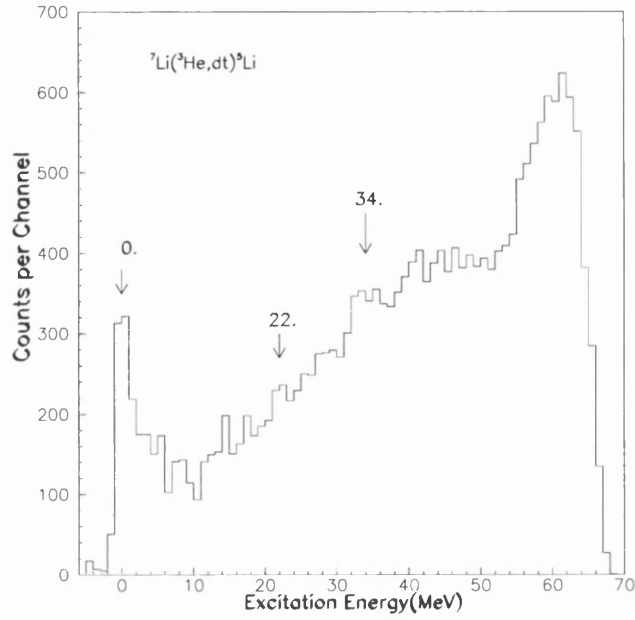


Figure 4.13: *Excitation energy spectrum from the  ${}^7\text{Li}({}^3\text{He}, dt){}^5\text{Li}$  reaction[38].*

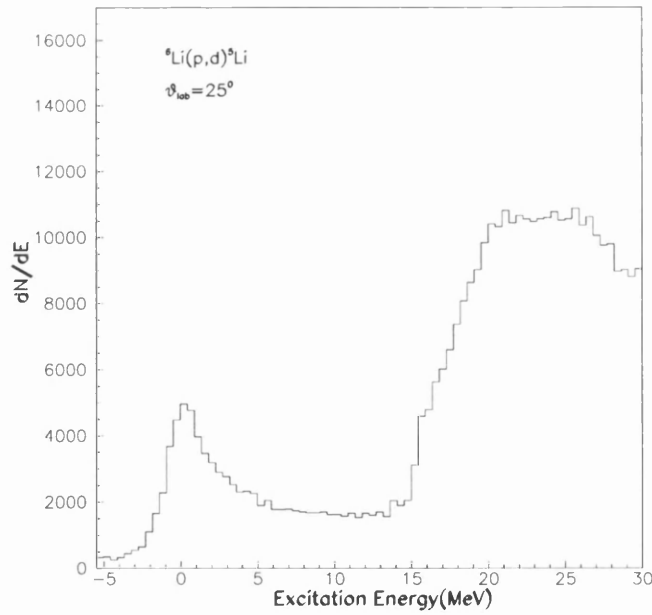


Figure 4.14: *Excitation energy spectrum from the  ${}^6\text{Li}(p, d){}^5\text{Li}$  reaction at  $25^\circ$  (lab) detection angle[13].*

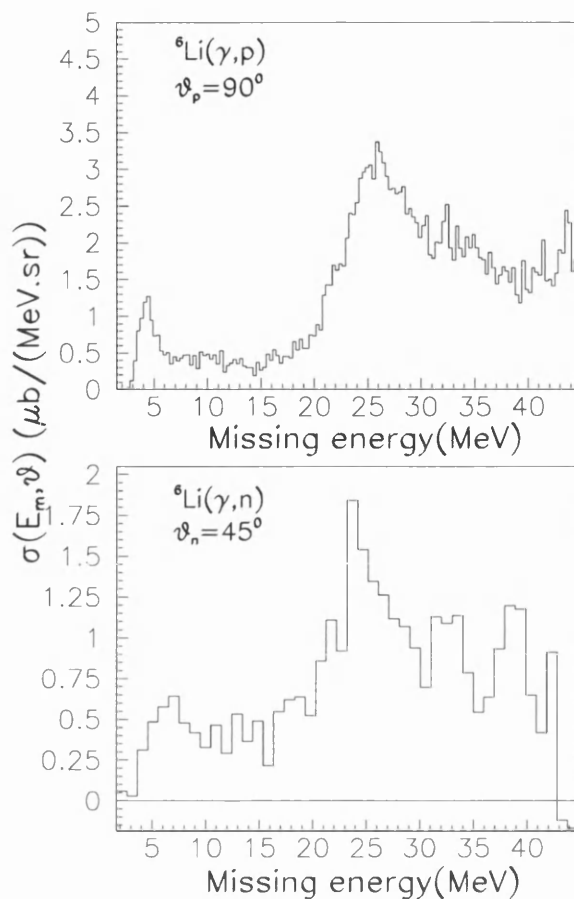


Figure 4.15: *Missing energy spectra for  ${}^6\text{Li}(\gamma, p)$  [68] and  ${}^6\text{Li}(\gamma, n)$  reactions.*

detection angle using tagged photons of average energy  $\sim 58$  MeV. Both spectra show similar structure with a ground state peak (4.6 MeV for  ${}^6\text{Li}(\gamma, p)$  5.7 MeV for  ${}^6\text{Li}(\gamma, n)$ ) and a large bump around 20-30 MeV missing energy. Although there has been no  $(e, e'n)$  measurement, it is interesting to consider the  $(e, e'p)$  reaction. The  $(e, e'p)$  reaction mechanism is predominantly QFK and the  ${}^6\text{Li}(e, e'p)$  spectrum[56] shown in Fig.4.16 shows excitation of the 1h states of  ${}^5\text{He}$  after 1p knockout ( $E_m=4.6$  MeV) and 1s knockout ( $E_m=21.35$  MeV). Both are visible in  $(\gamma, p)$ , the latter appearing as a small shoulder on the continuum distribution. 1s knockout in  $(\gamma, n)$  would produce the broad  $\frac{1}{2}^-$   ${}^5\text{Li}$  state which

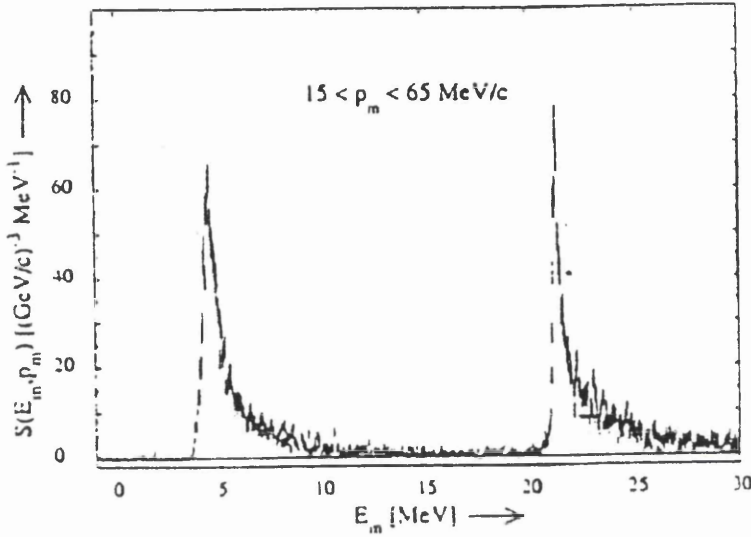


Figure 4.16: Missing energy spectrum for  ${}^6\text{Li}(e, e'p)$  reaction [56].

would appear at  $E_m=10-15$  MeV missing energy in Fig.4.15. This  $E_m$  region also contains continuum  ${}^6\text{Li}(\gamma, pn)$  strength.

#### 4.4.1 Cross sections and Comparison with $(\gamma, p)$ Measurements

Differential cross sections for the  ${}^6\text{Li}(\gamma, n)$  reaction were obtained for a photon energy range of 50.14-64.22 MeV ( $\sim 58$  MeV average) for the missing energy range 3-9 MeV which contains  $(\gamma, n_0)$  and  $(\gamma, n)p, {}^4\text{He}$ : ( $\sigma_{3-9}^n$ ); the missing energy range of 3-15 MeV which contains  $(\gamma, n_{01})$  and  $(\gamma, n)p, {}^4\text{He}$ : ( $\sigma_{3-15}^n$ ); and the region of 20-30 MeV missing energy which contains  $(\gamma, n)p, {}^4\text{He}$  and  $(\gamma, n) {}^3\text{He}, d$ : ( $\sigma_{20-30}^n$ ). These are displayed in Fig.4.17 where they are compared with equiv-

alent ( $\gamma, p$ ) measurements which were obtained with tagged photons of average energy  $\sim 59$  MeV. The equivalent ( $\gamma, p$ ) measurements are labelled  $\sigma_{3-9}^p$ ,  $\sigma_{3-15}^p$  and  $\sigma_{20-30}^p$  respectively.

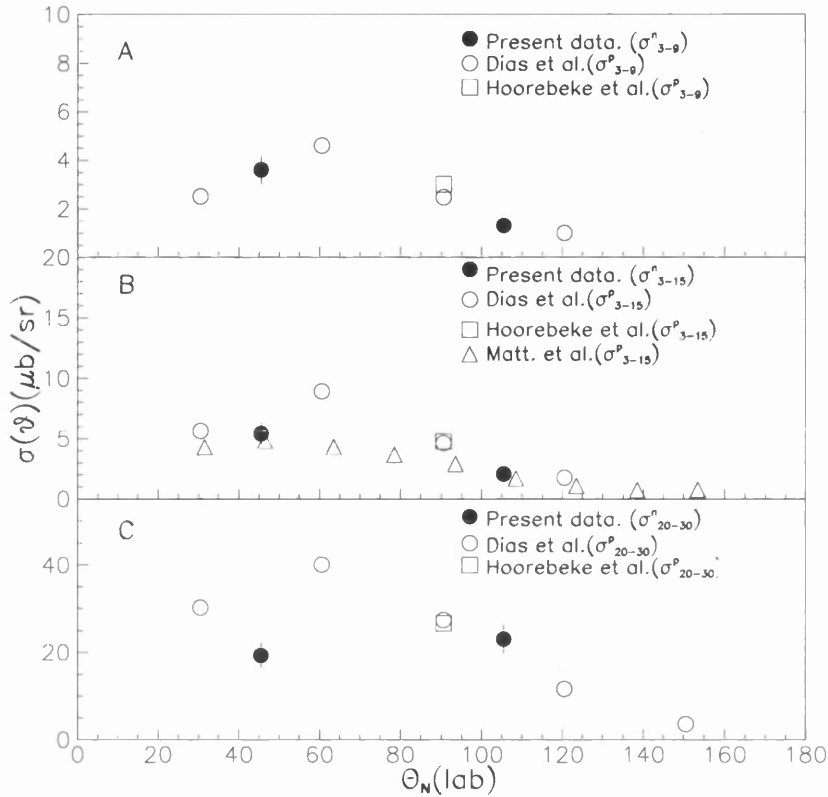


Figure 4.17: Angular distributions of  ${}^6\text{Li}(\gamma, n)$  and comparison with equivalent  ${}^6\text{Li}(\gamma, p)$  data. (open circles from [26], open triangle from [64] and open rectangles from [46]).

From Fig.4.17A  $\sigma_{3-9}^n$  and  $\sigma_{3-9}^p$  [26, 46] appear to be very similar. A bremsstrahlung ( $\gamma, p$ ) measurement which had poor energy resolution [64] has a somewhat lower  $\sigma_{3-15}^p$  than the later tagged photon measurements [26, 46] (Fig.4.17B). From Fig.4.17C  $\sigma_{20-30}^n$  appears to be significantly smaller than  $\sigma_{20-30}^p$  at forward angle.

The  $\sigma_{3-9}^n$ ,  $\sigma_{3-15}^n$  and  $\sigma_{20-30}^n$  cross sections as a function of photon energy are

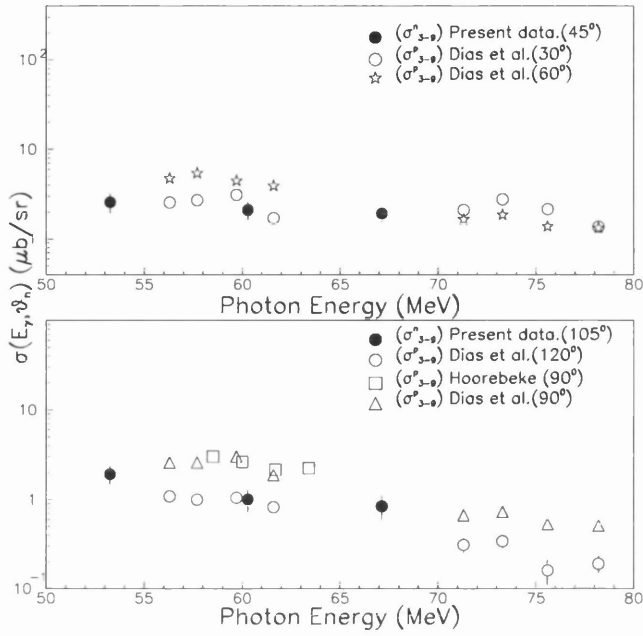


Figure 4.18: Cross-section as a function of photon energy for the  ${}^6\text{Li}(\gamma, N)$  reaction in the 3-9 MeV missing energy range.

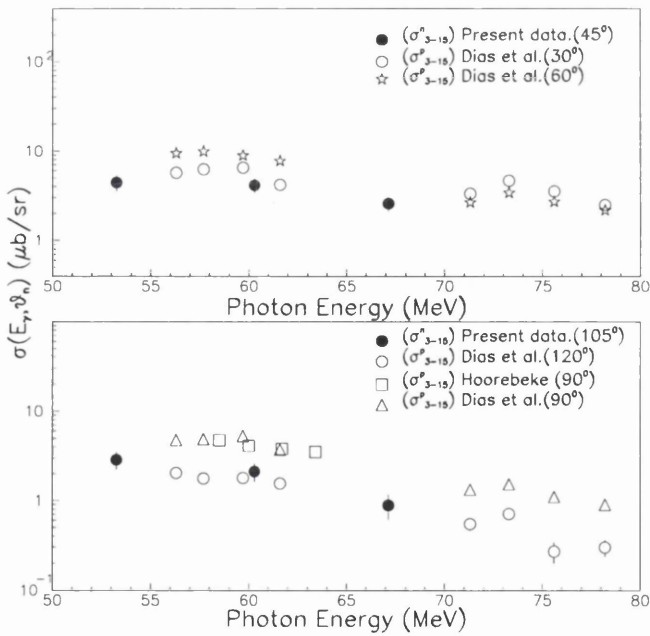


Figure 4.19: Cross-section as a function of photon energy for the  ${}^6\text{Li}(\gamma, N)$  reaction in the 3-15 MeV missing energy range.

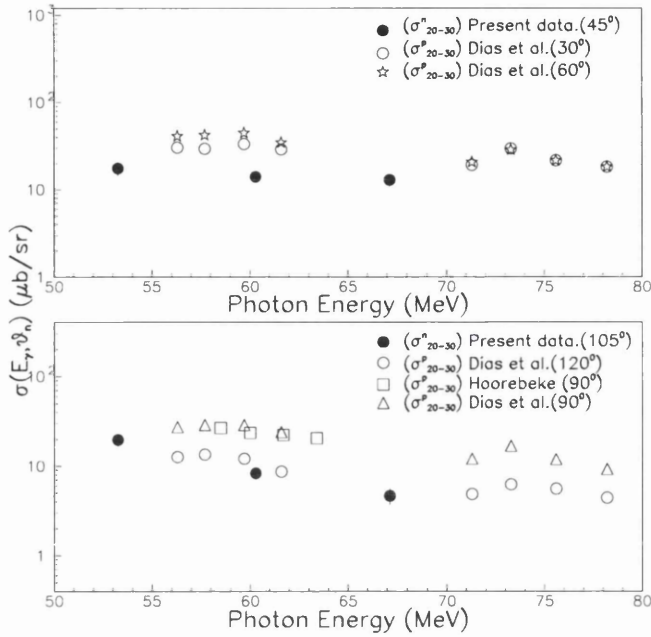


Figure 4.20: Cross-section as a function of photon energy for the  ${}^6\text{Li}(\gamma, N)$  reaction in the 20-30 MeV missing energy range.

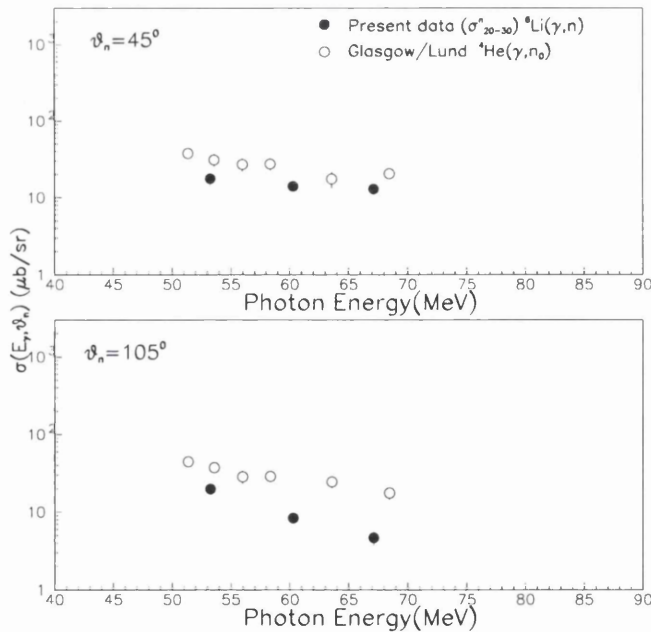


Figure 4.21: Cross-sections for the  ${}^6\text{Li}(\gamma, n)$  reaction in the 20-30 MeV missing energy range, as a function of photon energy, and comparison with  ${}^4\text{He}(\gamma, n)$  measurements[81].

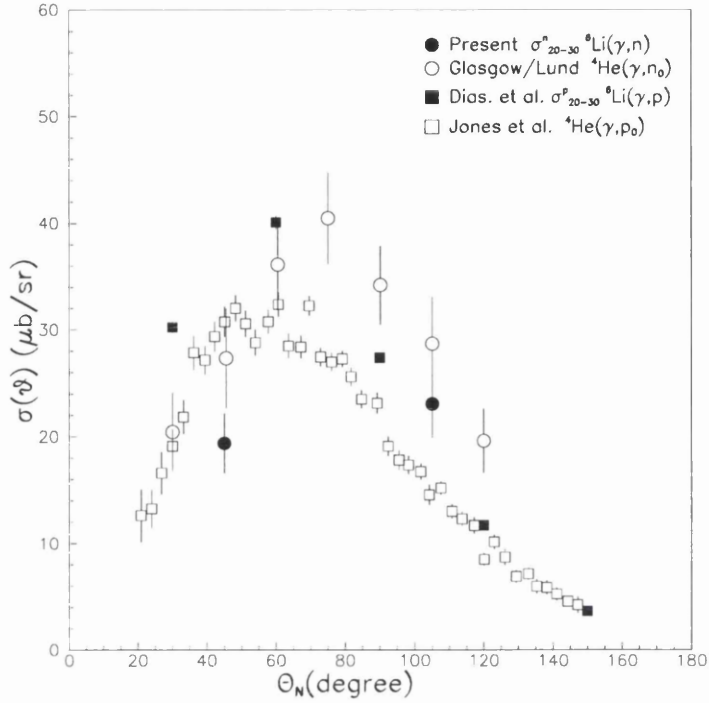


Figure 4.22: Angular distributions of  ${}^6\text{Li}(\gamma, N)$  reactions in the 20-30 MeV missing energy range and  ${}^4\text{He}(\gamma, N)$  reactions. ( $(\gamma, p)$  data from [26, 49] and  ${}^4\text{He}(\gamma, n)$  data from [81]).

shown in Fig.4.18,4.19 and 4.20 respectively where they are compared with equivalent  $(\gamma, p)$  measurements[28, 46]. The photon energy dependence is relatively weak for both  $(\gamma, n)$  and  $(\gamma, p)$ .

It is interesting to compare the cross section of the  ${}^6\text{Li}(\gamma, N)$  reaction in the missing energy region 20-30 MeV ( $\sigma_{20-30}^n, \sigma_{20-30}^p$ ) with the cross section of the  ${}^4\text{He}(\gamma, N)$  reaction [81, 49]. This may give an indication of the importance of absorption of photons by the  $\alpha$ -core in  ${}^6\text{Li}$ . These are shown in Fig4.21 where cross sections as a function of photon energy are presented for  $(\gamma, n)$  and Fig4.22 where angular distributions are presented for  $(\gamma, N)$ . The similarity between these cross sections suggests that a substantial part of the strength observed for

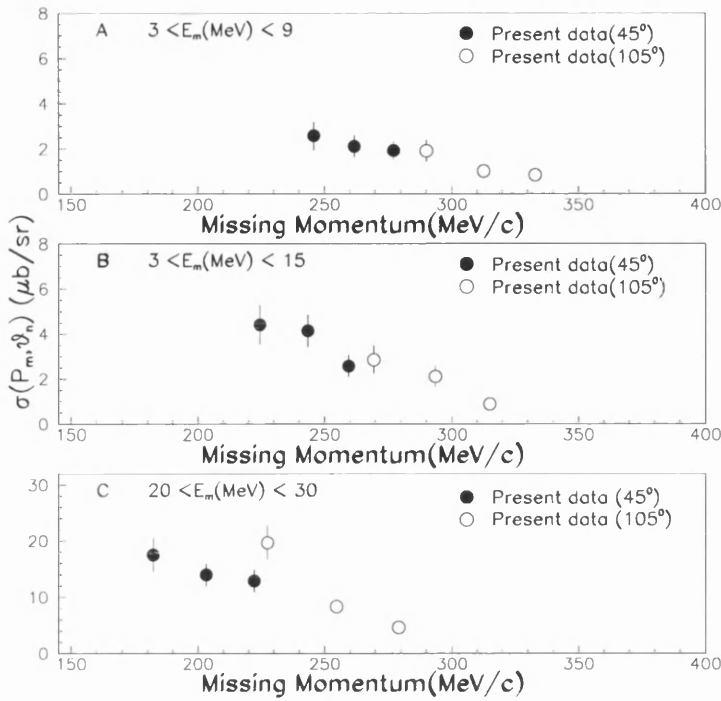


Figure 4.23: Cross section for the  ${}^6\text{Li}(\gamma, n)$  reaction as a function of missing momentum.

the  ${}^6\text{Li}(\gamma, n)$  reaction in the 20-30 MeV missing energy region is due to  $(\gamma, n){}^3\text{He}$  and for the  ${}^6\text{Li}(\gamma, p)$  reaction in the 20-30 MeV missing energy region is due to  $(\gamma, p)t$  on the  $\alpha$ -core, with the valence p-n pair spectating. It should be noted that the  ${}^4\text{He}(\gamma, p)$  measurement was performed with  $\sim 64$  MeV photons while the others used  $\sim 58$  MeV photons.

It may be instructive to plot cross section as a function of missing momentum  $P_m$ , as the  $P_m$  dependence may indicate the reaction mechanism involved. For example the scaling of cross section with missing momentum would be expected in the case of QFK, although scaling behaviour, with different missing-momentum dependence is also observed where 2N mechanisms are expected. For the  $(\gamma, n)$

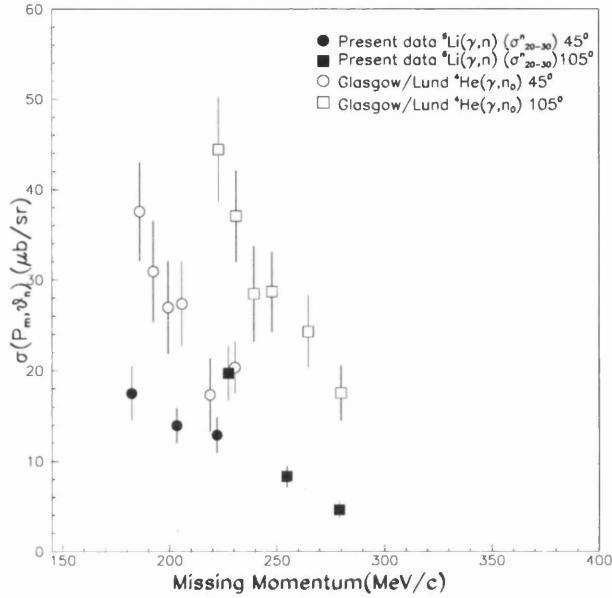


Figure 4.24: Cross sections for the  ${}^6\text{Li}(\gamma, n)$  reaction in 20-30 MeV missing energy region, as a function of missing momentum and comparison with  ${}^4\text{He}(\gamma, n)$  measurement[81].

reaction the missing momentum is defined as

$$\mathbf{P}_m = \mathbf{P}_\gamma - \mathbf{P}_n = -\mathbf{P}_{\text{recoil}} \quad (4.1)$$

where  $\mathbf{P}_{\gamma, n}$  are respectively the measured photon and neutron momentum. Fig.4.23 shows the missing momentum dependence of region  $\sigma_{3-9}^n$  (A),  $\sigma_{3-15}^n$  (B) and  $\sigma_{20-30}^n$  (C). Over the relatively small range of  $P_m$  covered  $\sigma_{3-9}^n$  and  $\sigma_{3-15}^n$  show a fairly smooth  $P_m$  dependence.

Finally the  $P_m$  dependence of the  ${}^4\text{He}(\gamma, n)$  reaction is compared with that of  $\sigma_{20-30}^n$ . This comparison is made in Fig.4.24. Scaling behaviour is not observed in either case.

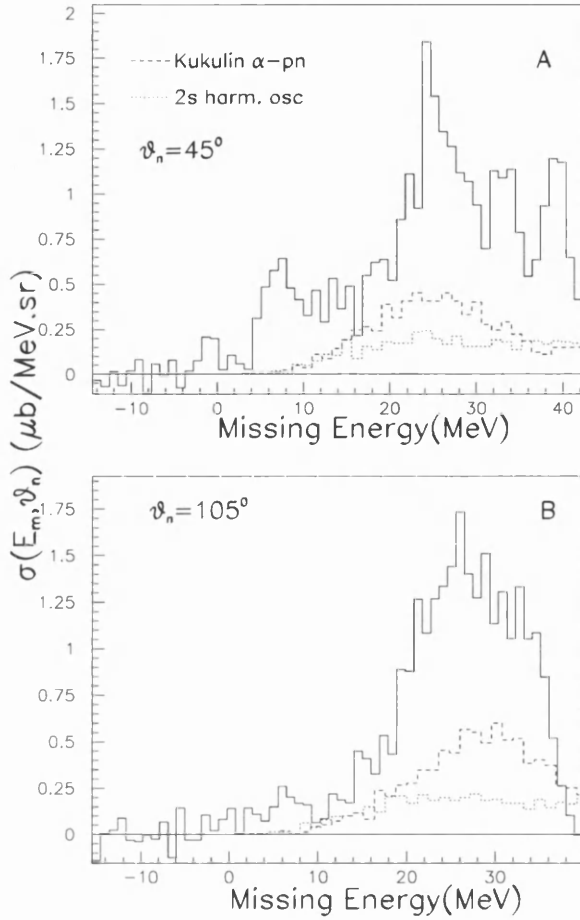


Figure 4.25: *Missing energy spectra for the  ${}^6\text{Li}(\gamma, n)$  reaction and comparison with theoretical calculations obtained from the monte carlo code MORGAINE[51].*

#### 4.4.2 Comparison with Theoretical Calculations

The  $(\gamma, n)$  missing energy spectra were calculated on the basis of the QD model as formulated by Gottfried[41] using the Monte Carlo code MORGAINE[51] (MONte carlo for REAL GAMMA Induced Nucleon Emission). Gottfried showed that the  $(\gamma, pn)$  cross section, subject to some approximations, depends on two quantities

$$\sigma \propto F(P) \times S(\tau) \quad (4.2)$$

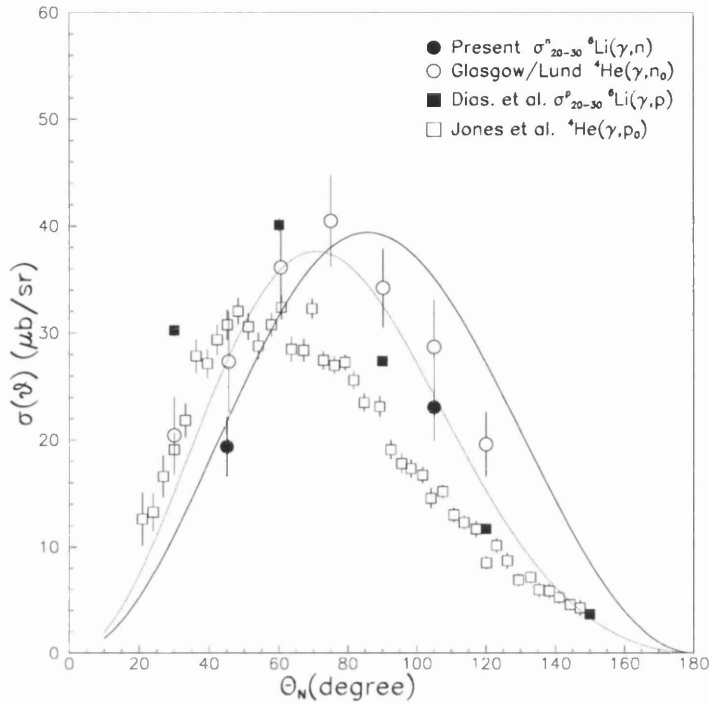


Figure 4.26: Angular distributions of  ${}^6\text{Li}(\gamma, N)$  reactions in the 20-30 MeV missing energy range and  ${}^4\text{He}(\gamma, N)$  reactions compared with theoretical calculations [34] for  ${}^4\text{He}(\gamma, N)$ .

where  $F(P)$  is the probability that a p-n pair has a momentum  $P$ , which in heavier nuclei would be calculated on the basis of the shell model, and  $S(r)$  is a semi-empirical correlation function which depends on the relative p-n coordinates. This model was first developed for the analysis of  $(\gamma, pn)$  measurements [51]. It is assumed that the photon is absorbed by a p-n pair that moves inside the target nucleus with a given momentum distribution.

The p-n pair photoabsorption process is then modeled using the real deuteron 2-body photodisintegration cross section. For the ground state of  ${}^6\text{Li}$  a cluster wave function of Kukulin et al.[54](dashed line in Fig.4.25) and a shell model wavefunction using a harmonic oscillator potential of Wade et al.[87] (dotted

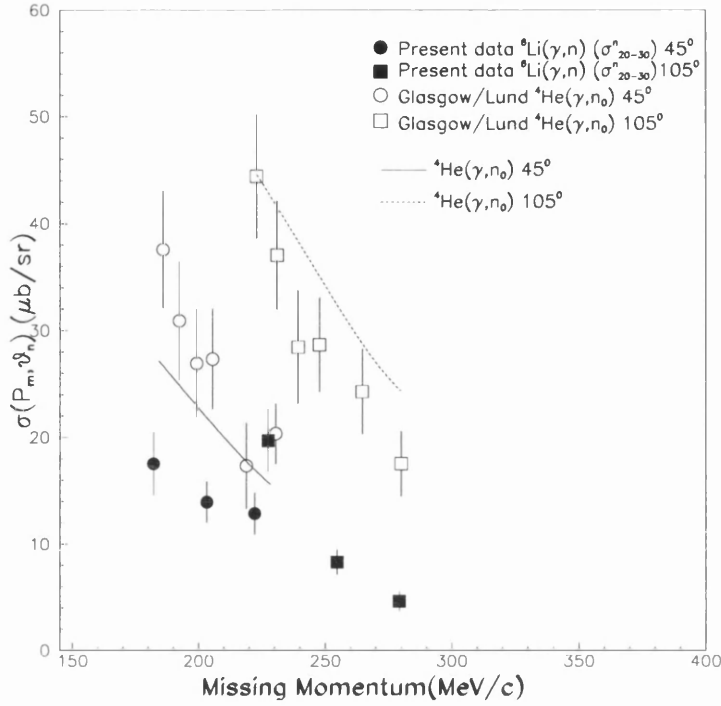


Figure 4.27: Cross sections as a function of missing momentum for the  ${}^6\text{Li}(\gamma, n)$  ( $E_m=20\text{-}30\text{ MeV}$ ) and  ${}^4\text{He}(\gamma, n)$  measurements [81] compared with theoretical calculations [34].

line in Fig.4.25) were used. The kinetic energy distribution of the neutron was obtained and then converted into apparent (for a  $(\gamma, n)$  reaction) missing energy. This calculation includes a simulation of the experimental situation, including the coverage of a finite solid angle by the detectors, the detector thresholds, detector energy resolution and photon energy range. In the missing energy region below 21 MeV where the only contribution apart from 1p or 1s neutron knock out is due to the  $(\gamma, pn)$  reaction, the cluster-model-wavefunction calculation is in better agreement with the data. In the 10-15 MeV missing energy range both calculations fall below the data (Fig.4.25), which may indicate appreciable strength for 1s knockout to the  $\frac{1}{2}^-$  state of  ${}^5\text{Li}$ .

For the higher missing energy range (20-30 MeV), where  ${}^6\text{Li}(\gamma, n){}^3\text{He}+d$  is also possible, both  $(\gamma, pn)$  calculations are markedly lower than the data. To investigate further this missing energy range the measured cross sections of  ${}^6\text{Li}(\gamma, N)$  ( $(\gamma, p)$  data from [26]) and  ${}^4\text{He}(\gamma, N)$  [81, 49] are compared (Fig.4.26) with a calculation made in the Alt-Grassberger-Sandhas (AGS) type integral-equation formalism [4, 42] which attempts to solve the four-nucleon Schrödinger equation [34] using a reasonably realistic model of the N-N potential [61]. Both electric dipole (E1) and electric quadrupole (E2) contributions were taken into account. In Fig.4.26 the solid curve shows the  ${}^4\text{He}(\gamma, n)$  calculation while the dotted curve shows the  ${}^4\text{He}(\gamma, p)$  calculation. The calculation predicts, due to spin-isospin mixing effects, a bigger E2 influence for  $(\gamma, p)$ , producing a more forward biased distribution. This is shown in the  ${}^4\text{He}(\gamma, N)$  data and to a certain extent in  ${}^6\text{Li}(\gamma, n)$  although here the data are too sparse to be conclusive. In Fig.4.27 the calculated cross section as a function of  $P_m$  is compared with the data from  ${}^6\text{Li}(\gamma, n)$  and  ${}^4\text{He}(\gamma, n)$  reactions. Neither data nor calculation show a smooth  $P_m$  dependence.

## 4.5 Summary and Outlook

The data presented in this thesis are the first tagged photon  $(\gamma, n)$  measurements on  ${}^6\text{Li}$  at intermediate photon energy and the first triple coincidence  $(\gamma, n\gamma')$  measurements, where detection of decay photons from the A-1 residual nucleus, in coincidence with knocked-out neutrons, has been used to achieve very good energy resolution, unobtainable from  $(\gamma, n)$ . Both measurements provide important information about the nature of the photon absorption mechanism and on the structure of the target nucleus.

The results from the measurement of the  $(\gamma, n\gamma')$  reaction are very promising. Good decay-photon energy resolution, around 300 keV at 6 MeV which is good enough to resolve 5.2 and 6.2 MeV states in  $^{15}\text{O}$ , was obtained. The best obtainable energy resolution was 1 MeV with  $(\gamma, n)$  where only a single angle was obtained. In the comparison with theoretical calculations, the Gent HF-RPA treatment of  $(\gamma, n_0)$  and  $(\gamma, n_3)$  to the mainly  $1h \frac{1}{2}^-$  (ground) and  $\frac{3}{2}^-$  (6.2 MeV) states works reasonably well. However in the case of  $(\gamma, n_{12})$  to the  $\frac{5}{2}^+, \frac{1}{2}^+$  (5.2 MeV) doublet the Gent MEC model fails. The 5.2 MeV doublet has a small  $1h$  impurity configuration which was calculated by HF-RPA and added coherently to the MEC calculation giving a big enhancement in the cross section. As a result of this very successful pilot measurement, further measurements are now in progress at Max-Lab, using three large NaI(Tl) photon detectors which give a factor 5 increase in counting rate for  $(\gamma, n\gamma')$ . In this measurement a full angular distribution will be obtained. The  $^{12}\text{C}(\gamma, n\gamma')$  reaction will also be measured, this time to investigate the mainly  $2h1p \sim 7$  MeV triplet of states in  $^{11}\text{C}$ , as a further test of MEC calculations.

In the case of the  $^6\text{Li}(\gamma, n)$ , consideration of the cluster structure appears to be very important. The ground state of  $^5\text{Li}$  is seen clearly in the missing energy spectrum, which is very similar to the  $^6\text{Li}(\gamma, p_0)$  reaction. The  $\frac{3}{2}^-$  ground state can be populated by QFK, where a  $1p_{3/2}$  neutron is knocked-out, or by an MQD interaction with the valence p-n pair where the p is left "bound" to  $^4\text{He}$ . This is also some (less conclusive) evidence for population of the broad  $\frac{1}{2}^-$  state in  $^5\text{Li}$ . The ground state peak (and  $\frac{1}{2}^-$ ) is superimposed on a continuum, peaking at  $\sim 25$  MeV missing energy. This structure is again similar to  $^6\text{Li}(\gamma, p)$ . Integrating the peak region of the continuum gives a differential cross section similar to that obtained in  $^4\text{He}(\gamma, n)$ , suggesting the interaction of photons with the  $\alpha$ -core of

${}^6\text{Li}$ . A QD model calculation was attempted using a Kukulín cluster-model wave function to give the p-n pair momentum distribution and was reasonably close to the data in the continuum region below the threshold for  $\gamma + {}^6\text{Li} \rightarrow {}^3\text{He} + n + d$  reaction.

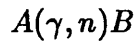
The  $(\gamma, N)$  project at Max-Lab will continue with further  $(\gamma, n\gamma')$  measurements on  ${}^{16}\text{O}$  and  ${}^{12}\text{C}$ . Given the promise shown by the first  $(\gamma, n)$  measurements on  ${}^6\text{Li}$ , it is hoped to measure at more angles and photon energies.  ${}^3\text{He}$  and  ${}^4\text{He}$  total cross sections will also be measured. These data will guide current microscopic theoretical models which seek to build the wavefunction of few-body nuclei.

# Appendix A

## Kinematics for the $A(\gamma, n)B$ Reaction

In this appendix the kinematical aspects of a single nucleon knock-out photoneuclear process are presented

A photon with energy  $E_\gamma$  and momentum  $\mathbf{P}_\gamma$  impinges on a target nucleus A at rest in the lab-system (Fig.A.1). After the reaction a particle(neutron) is emitted with momentum  $\mathbf{P}_n$  and energy  $E_n$  and the nucleus B recoils with momentum  $\mathbf{P}_B$  and energy  $E_B$ (Fig.A.1).

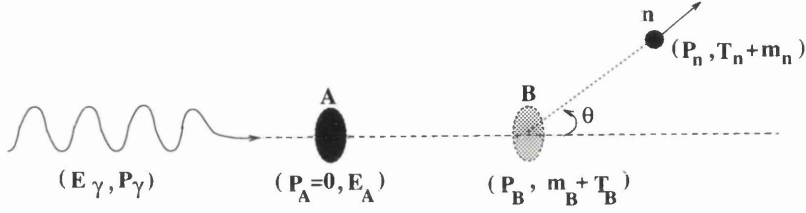


The target mass A is known, the momentum and energy of the incoming photon are measured , and the momentum and energy of the emitted neutron are measured. The momentum and energy of the residual system is determined by using conservation of the momentum and energy .

$$\mathbf{P}_A + \mathbf{P}_\gamma = \mathbf{P}_n + \mathbf{P}_B \quad (\text{A.1})$$

$$E_A + E_\gamma = E_n + E_B \quad (\text{A.2})$$

where E is the total energy given by (c=1)

Figure A.1: Kinematics for the  $A(\gamma, n)B$  Reaction

$$E = T + m \quad (\text{A.3})$$

Since the target nucleus A is at rest

$$P_A = 0$$

$$E_A = m_A$$

and A1 and A2 can be written

$$P_\gamma = P_n + P_B \quad (\text{A.4})$$

$$m_A + E_\gamma = E_n + E_B \quad (\text{A.5})$$

Using equation A3 in A5

$$E_\gamma - T_n - T_B = m_n + m_B^* - m_A \quad (\text{A.6})$$

where  $m_B^*$  denotes that the residual nucleus may be left in an excited state.

the left hand side of equation A6 is defined as the missing energy (equation 3.2)

$$E_m = m_B^* + m_n - m_A \quad (\text{A.7})$$

equation A6 can be rewritten as

$$m_B^* + T_B = E_\gamma - T_n - m_n + m_A \quad (\text{A.8})$$

from equation A4 the law of the cosine is used

$$P_B^2 = P_\gamma^2 + P_n^2 - 2P_n P_\gamma \cos \theta \quad (\text{A.9})$$

since  $m_\gamma=0$

$$P_B^2 = E_\gamma^2 + P_n^2 - 2P_n E_\gamma \cos \theta \quad (\text{A.10})$$

The energy and momentum relationship is

$$P^2 = E^2 - m^2 = T^2 + 2mT \quad (\text{A.11})$$

A8 can be squared on both sides

$$(m_B^* + T_B)^2 = (E_\gamma - T_n - m_n + m_A)^2 \quad (\text{A.12})$$

$$m_B^{*2} + 2T_B m_B^* + T_B^2 = (E_\gamma - T_n - m_n + m_A)^2 \quad (\text{A.13})$$

from A10 and A11

$$T_B^2 + 2m_B T_B = E_\gamma^2 + P_n^2 - 2P_n E_\gamma \cos \theta \quad (\text{A.14})$$

$$m_B^* = [(E_\gamma - T_n - m_n + m_A)^2 - (E_\gamma^2 + P_n^2 - 2P_n E_\gamma \cos(\theta_n))]^{1/2} \quad (\text{A.15})$$

Using equation A15 in equation A7 the missing energy can be written:

$$E_m = \sqrt{(E_\gamma + m_A - T_n - m_n)^2 - (E_\gamma^2 + P_n^2 - 2E_\gamma P_n \cos(\theta_n))} + m_n - m_A \quad (\text{A.16})$$

# Appendix B

## Cross-section Results

Here tabulated numerical values of cross-sections will be presented. All cross-sections are presented in  $\mu\text{b}/\text{sr}$ . The total errors are statistical and systematical errors added in quadrature.

### The ${}^2\text{H}(\gamma, n)$ Reaction

$\theta_n$	$\frac{d\sigma}{d\Omega}$	$\Delta(\frac{d\sigma}{d\Omega})_{stat}[\%]$	$\Delta(\frac{d\sigma}{d\Omega})_{sys}[\%]$	$\Delta(\frac{d\sigma}{d\Omega})_{total}[\%]$
45°	7.6	16.3	12.5	20.6
105°	11.6	15.7	12.4	20.0

Table B.1: *The measured cross-section ( $\mu\text{b}/\text{sr}$ ) for photodisintegration of the deuteron.*

The  $^{16}\text{O}(\gamma, n)$  Reaction

$\theta_n$	$\frac{d\sigma}{d\Omega}$	$\Delta(\frac{d\sigma}{d\Omega})_{stat}[\%]$	$\Delta(\frac{d\sigma}{d\Omega})_{sys}[\%]$	$\Delta(\frac{d\sigma}{d\Omega})_{total}[\%]$
45°	7.9	4.4	12.4	13.2
105°	1.5	16.5	12.3	20.6

Table B.2: *The measured cross-sections ( $\mu\text{b}/\text{sr}$ ) for the ground state ( $n_0$ ) of  $^{15}\text{O}$ .*

$\theta_n$	$\frac{d\sigma}{d\Omega}$	$\Delta(\frac{d\sigma}{d\Omega})_{stat}[\%]$	$\Delta(\frac{d\sigma}{d\Omega})_{sys}[\%]$	$\Delta(\frac{d\sigma}{d\Omega})_{total}[\%]$
45°	18.6	2.1	12.8	13.0
105°	7.5	4.6	12.3	13.1

Table B.3: *The measured cross-sections ( $\mu\text{b}/\text{sr}$ ) for the 5.2-6.2 MeV ( $n_{123}$ ) unresolved states of  $^{15}\text{O}$ .*

The  $^{16}\text{O}(\gamma, n\gamma')$  Reaction

$\theta_n$	$\frac{d\sigma}{d\Omega}$	$\Delta(\frac{d\sigma}{d\Omega})_{stat}[\%]$	$\Delta(\frac{d\sigma}{d\Omega})_{sys}[\%]$	$\Delta(\frac{d\sigma}{d\Omega})_{total}[\%]$
45°	7.7	24.5	14.9	28.7
105°	5.2	37.5	15.0	40.8

Table B.4: *The measured cross-sections ( $\mu\text{b}/\text{sr}$ ) for the 5.2 MeV ( $n_{12}$ ) states of  $^{15}\text{O}$ .*

$\theta_n$	$\frac{d\sigma}{d\Omega}$	$\Delta(\frac{d\sigma}{d\Omega})_{stat}[\%]$	$\Delta(\frac{d\sigma}{d\Omega})_{sys}[\%]$	$\Delta(\frac{d\sigma}{d\Omega})_{total}[\%]$
45°	10.9	15.2	14.9	21.3
105°	2.3	52.5	15.0	55.1

Table B.5: *The measured cross-sections ( $\mu b/sr$ ) for the 6.2 MeV ( $n_3$ ) state of  $^{15}O$ .*

### The ${}^6Li(\gamma, n)$ Reaction

The cross-section for the  ${}^6Li(\gamma, n)$  reaction was measured in three different missing energy ranges. The missing energy range 3-9 MeV ( $\sigma_{3-9}^n$ ), missing energy range 3-15 MeV ( $\sigma_{3-15}^n$ ) and missing energy range 20-30 MeV ( $\sigma_{20-30}^n$ ).

$\theta_n$	$\frac{d\sigma}{d\Omega}$	$\Delta(\frac{d\sigma}{d\Omega})_{stat}[\%]$	$\Delta(\frac{d\sigma}{d\Omega})_{sys}[\%]$	$\Delta(\frac{d\sigma}{d\Omega})_{total}[\%]$
45°	3.6	12.4	12.4	17.5
105°	1.3	3.2	16.0	16.3

Table B.6: *The measured cross-sections ( $\mu b/sr$ ) for the  ${}^6Li(\gamma, n)$  reaction at 3-9 MeV missing energy ( $\sigma_{3-9}^n$ ) using tagged photons of average energy 58 MeV.*

$\theta_n$	$\frac{d\sigma}{d\Omega}$	$\Delta(\frac{d\sigma}{d\Omega})_{stat}[\%]$	$\Delta(\frac{d\sigma}{d\Omega})_{sys}[\%]$	$\Delta(\frac{d\sigma}{d\Omega})_{total}[\%]$
45°	5.4	10.2	12.4	16.0
105°	2.0	22.6	12.4	25.7

Table B.7: *The measured cross-sections ( $\mu b/sr$ ) for the  ${}^6Li(\gamma, n)$  reaction at 3-15 MeV missing energy ( $\sigma_{3-15}^n$ ) using tagged photons of average energy 58 MeV.*

$\theta_n$	$\frac{d\sigma}{d\Omega}$	$\Delta(\frac{d\sigma}{d\Omega})_{stat}[\%]$	$\Delta(\frac{d\sigma}{d\Omega})_{sys}[\%]$	$\Delta(\frac{d\sigma}{d\Omega})_{total}[\%]$
45°	19.4	5.7	13.3	14.5
105°	23.0	4.2	13.2	13.9

Table B.8: *The measured cross-sections ( $\mu b/sr$ ) for the  ${}^6Li(\gamma, n)$  reaction at 20-30 MeV missing energy ( $\sigma_{20-30}^n$ ) using tagged photons of average energy 58 MeV.*

$\theta_n$	$E_\gamma(\text{MeV})$	$\frac{d\sigma}{d\Omega}$	$\Delta(\frac{d\sigma}{d\Omega})_{stat}[\%]$	$\Delta(\frac{d\sigma}{d\Omega})_{sys}[\%]$	$\Delta(\frac{d\sigma}{d\Omega})_{total}[\%]$
45°	50.2-56.4	2.6	19.8	13.5	24.0
	56.4-64.2	2.1	18.5	13.0	22.6
	64.2-70.0	2.0	15.2	12.9	19.9
105°	50.2-56.4	2.0	20.9	13.4	24.9
	56.4-64.2	1.0	25.7	12.5	28.6
	64.2-70.0	0.9	28.3	13.7	31.5

Table B.9: *The measured cross-sections ( $\mu b/sr$ ) for the  ${}^6Li(\gamma, n)$  reaction at 3-9 MeV missing energy ( $\sigma_{3-9}^n$ ) for various photon energy bins.*

$\theta_n$	$E_\gamma(\text{MeV})$	$\frac{d\sigma}{d\Omega}$	$\Delta(\frac{d\sigma}{d\Omega})_{stat}[\%]$	$\Delta(\frac{d\sigma}{d\Omega})_{sys}[\%]$	$\Delta(\frac{d\sigma}{d\Omega})_{total}[\%]$
45°	50.2-56.4	4.4	15.2	12.4	19.6
	56.4-64.2	4.1	12.5	12.4	17.6
	64.2-70.0	2.6	13.5	12.4	18.3
105°	50.2-56.4	2.9	17.6	12.4	21.5
	56.4-64.2	2.1	18.3	12.4	22.1
	64.2-70.0	0.9	28.7	12.5	31.3

Table B.10: *The measured cross-sections ( $\mu\text{b}/\text{sr}$ ) for the  ${}^6\text{Li}(\gamma, n)$  reaction at 3-15 MeV missing energy range ( $\sigma_{3-15}^n$ ) for various photon energy bins.*

$\theta_n$	$E_\gamma(\text{MeV})$	$\frac{d\sigma}{d\Omega}$	$\Delta(\frac{d\sigma}{d\Omega})_{stat}[\%]$	$\Delta(\frac{d\sigma}{d\Omega})_{sys}[\%]$	$\Delta(\frac{d\sigma}{d\Omega})_{total}[\%]$
45°	50.2-56.4	17.5	9.4	14.2	17.0
	56.4-64.2	14.0	7.4	14.6	13.9
	64.2-70.0	12.9	8.0	16.7	15.3
105°	50.2-56.4	19.7	6.2	14.0	15.3
	56.4-64.2	8.3	6.8	12.3	14.1
	64.2-70.0	4.6	12.9	14.9	19.7

Table B.11: *The measured cross-sections ( $\mu\text{b}/\text{sr}$ ) for the  ${}^6\text{Li}(\gamma, n)$  reaction at 20-30 MeV missing energy range ( $\sigma_{20-30}^n$ ) for various photon energy bins.*

# Bibliography

- [1] J.O.ADLER ET AL.:*Nucl. Instr.and Meths.***A388**(1997)17
- [2] J.AHRENS :*Nucl. Phys.* **A446** (1985)229c
- [3] F. AJZENBERG :*Nucl. Phys.* **A490** (1988)1
- [4] E. O. ALT ET AL. :*Phys. Rev.* **C1** (1970)85
- [5] B.E.ANDERSSON: *PhD Thesis Lund* 1994(unpublished)
- [6] B.E.ANDERSSON ET AL. :*Phys. Rev.* **C51** (1995)2553
- [7] J.N. ANDERSSON :*Max-Lab Report Lund* 1995(unpublished)
- [8] J.R.M ANNAND :*Nucl. Instr. and Meths.* **A262** (1987)371
- [9] J.R.M ANNAND ET AL. :*Phys. Rev. Let.* **71** (1993)2703
- [10] J.R.M ANNAND ET AL. :*Nucl. Instr.and Meths.* **A386** (1996)385
- [11] J.R.M ANNAND ET AL. :*Nucl. Instr. and Meths.* **A400** (1997)344
- [12] J.R.M ANNAND :*private communication*
- [13] D. BACHELIER ET AL. :*Nucl. Phys.* **A126** (1969)60
- [14] G. BENENTI ET AL. :*Nucl. Phys.* **A574** (1994)716

- [15] B. L. BERMAN ET AL. :*Phys. Rev. Lett.* **15** (1965)727
- [16] S. BOFFI :*Nucl. Phys.* **A359** (1981)91
- [17] R. BRUN ET AL. :*Geant Cern DD/EE/84* (1987)
- [18] N.A. BURKOVA ET AL. :*Phys. Lett.* **B248** (1990)15
- [19] P.J. CARLOS :*Phys. Lett.* **B203** (1988)333
- [20] M. CAVINATO :*Nucl. Phys.* **A373** (1982)445
- [21] M. CAVINATO :*Nuova cim* **A76** (1983)197
- [22] M. CAVINATO :*Nucl. Phys.* **A442** (1984)237
- [23] R.A. CECIL ET AL. :*Nucl. Instr. and Meths.* **A161** (1979)439
- [24] J. CHADWICK AND M. GOLDHABER: *Nature* **134** (1934)237
- [25] S. COSTA ET AL. :*Phys. Lett.* **B203** (1963)308
- [26] J.F. DIAS ET AL. :*Nucl. Phys.* **A587** (1995)434
- [27] J.F. DIAS ET AL.:*Phys. Rev.***C55**(1997)942
- [28] J.F. DIAS :*PhD Thesis Gent* 1994(unpublished)
- [29] J.K. DICKENS:*Monte Carlo code SCINFUL*,ORNL-64621988
- [30] G. DIETZE ET AL.:*Monte Carlo code NRESP7*,PTB Report ND-221982
- [31] S.S. DIETRICH ET AL.:*Atomic Data and Nuclear Data Tables* **38** (1988)199
- [32] M. DROSG :*Nucl. Instr. and Meths.* **105**(1972)573
- [33] J.A. EDEN ET AL. :*Phys. Rev.* **C44**(1991)753

- [34] G. ELLERKMANN ET AL. :*Phys. Rev.* **C53**(1996)2638
- [35] S. FERRONI ET AL. :*Nucl. Phys.* **76** (1966)58
- [36] D.J.S.FINDLAY AND OWENS:*Nucl. Phys.* **A292** (1977)53
- [37] F.W.K. FIRK :*Nucl. Instr. and Meths.* **162**(1979)539
- [38] R. FRANKE ET AL.:*Nucl. Phys.* **A433**(1985)351
- [39] M. GARI AND H. HEBACH :*Phys. Rep.* **72**(1981)1
- [40] H. GORINGER ET AL. :*Nucl. Phys.* **A292** (1982)414
- [41] K. GOTTFRIED :*Nucl. Phys.* **5** (1958)557
- [42] P. GRASSBERGER ET AL. :*Nucl. Phys.* **B2** (1967)181
- [43] S.J. HALL ET AL.:*Nucl. Instr. and Meths.* **368**(1996)698
- [44] PETER HARTY ET AL. :*Phys. Rev.* **C37** (1988)13
- [45] HENRIK RUIJTER ET AL. :*Phys. Rev.* **C54** (1996)3076
- [46] L. HOOREBEKE :*PhD Thesis Gent* 1991(unpublished)
- [47] LENNART ISAKSSON: *PhD Thesis Lund* 1996(unpublished)
- [48] D.A. JENKINS ET AL.:*Phys. Rev.***C50**(1994)74
- [49] R.T. JONES ET AL.:*Phys. Rev.***C43**(1991)2052
- [50] K.J. KING ET AL.:*Nucl. Instr. and Meths.* **227** (1984)257
- [51] S. KLEIN :*PhD Thesis Tübingen* 1990(unpublished)
- [52] H. H. KNOX ET AL.:*Nucl. Instr. and Meths.***101**(1972)519

- [53] V.I. KUKULIN ET AL. :*Sov. Jour. of Nucl. Phys.* **34** (1981)11
- [54] V.I. KUKULIN ET AL. :*Nucl. Phys.* **A417** (1984)128
- [55] A. KUZIN ET AL. :*Aust. Jour. Phys.* **46**(1996)6
- [56] J.B.J.M. LANEN ET AL. :*Phys. Rev. Lett.* **62**(1989)2925
- [57] J.S.LEVINGER :*Phys. Rev.* **84** (1951)43
- [58] L.J. LONDERGAN :*Phys. Rev.* **C19** (1979)998
- [59] R.G. LOVAS ET AL. :*Nucl. Phys.* **A474** (1987)451
- [60] R.G. LOVAS ET AL. :*Nucl. Phys.* **A516** (1990)325
- [61] R. A. MALFLIER AND J.A. TJON:*Nucl. Phys.* **A127** (1969)161
- [62] J.L.MATTHEWS ET AL. :*Nucl. Instr. and Meths.***91**(1971)37
- [63] J.L.MATTHEWS ET AL. :*Nucl. Instr. and Meths.***111**(1973)157
- [64] J.L.MATTHEWS ET AL.:*Nucl. Phys.* **A267** (1976)51
- [65] G. MAUSER :*PhD Thesis Tübingen* 1993(unpublished)
- [66] J.C. MCGEORGE ET AL.:*Phys. Rev.* **51C** (1995)1967
- [67] G.J. MILLER ET AL. :*Nucl. Phys.* **A586** (1995)125
- [68] D. NILLSON ET AL. :*Phys. Scr.* **49** (1994)397
- [69] G.J. O'KEEFE :*PhD Thesis Melbourne* 1994(unpublished)
- [70] R.O.OWENS :*Nucl. Instr. and Meths.* **A288**(1990)574
- [71] W.C. PARKE ET AL :*Phys. Rev.* **C29** (1984)2319

- [72] CERN PROGRAM LIBRA **Q121** (1993)
- [73] P. ROSSI ET AL. :*Phys. Rev.* **C40** (1989)2412
- [74] D. RYCKBOSCH ET AL. :*Nucl. Phys.* **A568** (1994)52
- [75] J. RYCKEBUSCH ET AL. :*Nucl. Phys.* **A476**(1988)237
- [76] J. RYCKEBUSCH ET AL. :*Phys. Rev.* **C46** (1992)R829
- [77] B.SCHOCH :*Phys. Rev. Lett.* **41** (1978)80
- [78] B.SCHOCH :*Phys. Lett.* **109B** (1982)11
- [79] E.W. SCHMID ET AL. :*Phys. Lett.* **7** (1963)263
- [80] M.R.SENE' :*Nucl. Phys.* **A442** (1985)215
- [81] D.A. SIMS ET AL. <sup>4</sup>He( $\gamma, n$ ) data to be published in *Physc lett B*
- [82] D.A. SIMS ET AL. :*Phys. Rev.* **C55** (1997)1288
- [83] D.A. SIMS :*priviate communication*
- [84] V. VAN DER SLUYS ET AL. :*Phys. Rev.* **C49** (1994)2695
- [85] S.A. SOFIANOS ET AL. :*Phys. Rev.* **C48** (1993)2285
- [86] S.V SPRINGHAM:*Nucl. Phys.* **A517** (1990)93
- [87] M.W. WADE ET AL.:*Phys. Rev. Lett.***53**(1984)2540
- [88] J.W. WEIL ET AL. :*Phys. Rev.* **78** (1950)738
- [89] K. VARGA ET AL. :*Phys. Rev.* **C43** (1991)1201
- [90] V.V. VERBINSKI :*Nucl. Instr. and Meths.* **65**(1968)8